

Isotopes in Speleothems: Methods and Application

Isotopes in Speleothems: Methods and Application

By:

Mohammed Ibrahim Abdo EL-Shenawy

B. Sc., M. Sc.

A Thesis Submitted to the School of Graduate Studies in Partial Fulfillment of the
Requirements for the Degree Doctor of Philosophy

McMaster University

© Copyright by Mohammed EL-Shenawy, October 2016

Ph.D. Thesis – M. EL-Shenawy; McMaster University – School of Geography and Earth
Sciences

DOCTOR OF PHILOSOPHY (2016)
(Earth and Environmental Sciences)

McMaster University
Hamilton, Ontario

TITLE: Isotopes in Speleothems: Methods and Application

AUTHOR: Mohammed EL-Shenawy

B.Sc., M.Sc. (Beni Suef University, Free University of Brussels)

SUPERVISORS: Dr. Sang-Tae Kim

NUMBER OF PAGES: xiv, 169

Abstract

Speleothems (cave carbonate deposits) have been recognized as a multi-proxy paleoclimate archive. Variations in carbon and oxygen isotopes in speleothems can record past climate changes (e.g., temperature, rainfall and vegetation) under isotopic equilibrium conditions. However, non-climatic noises caused by in-cave processes may affect these stable isotope records under non-equilibrium isotopic conditions. The identification of equilibrium and non-equilibrium isotopic conditions in speleothems is still disputed in the speleothem research community; however, this is a prerequisite for the interpretation of carbon and oxygen isotope records in speleothems as paleoclimate proxies.

In this Ph.D. thesis, a series of laboratory experiments under cave-analogue conditions were performed to simulate the formation of speleothems in natural caves. The results of these experiments demonstrate that stable isotope equilibrium in speleothems is achieved under slow carbonate precipitation in pool-like settings (pool carbonates). On the basis of these pool carbonates, equilibrium carbon and oxygen isotope fractionation factors between calcite and water (or DIC for carbon) were determined. Our experiments show larger carbon and oxygen isotope non-equilibrium fractionations between calcite and water (or DIC for carbon) in stalagmite-like settings (fast carbonate precipitate) than those determined in pool-like settings. The flow rate of drip water above the surface of stalagmite appears to control the magnitude of these non-equilibrium isotope effects which increase with decreasing the flow rate.

Furthermore, a natural speleothem sample was examined as a paleoclimate archive in this thesis. The growth of a double stalagmite (WS-5d) in Wadi Sannur Cave from the Northeastern Sahara was used to infer the greening of the Sahara (intensive rainfall and vegetation). The U/Th dating in the WS-5d stalagmite suggests that greening conditions extended widely in the Sahara during the interglacial Marine Isotope Stages MIS 5.5, MIS 7.3, and the early MIS 9. Based upon oxygen isotope compositions from the WS-5d, we attributed the source of these greening periods to long-traveling rains from the

Atlantic Ocean that were delivered via the West African monsoon system. Our study suggests that the two youngest greening periods were concurrent with the arrival of *Homo sapiens* in the Levant and an earlier possible change in human population at 244 ka, indicating a key role of the Sahara route in early human dispersal out of Africa.

Finally, clumped isotope measurements (Δ_{47}) on carbonate-derived CO₂ have been shown to reflect the formation temperature of the carbonate minerals. The absolute Δ_{47} values of these isotopic measurements seem to be sensitive to the standardization methods (heated CO₂ gases and water-equilibrated CO₂ gases) that are used to normalize the raw Δ_{47} measurements. Neither the hypothetical base for the heated CO₂ gas standardization method nor the theoretical base for the water-equilibrated CO₂ gas standardization method has been experimentally tested. A series of CO₂ gases were heated in pre-dehumidified quartz tubes to obtain equilibrium Δ_{47} values of these CO₂ gases at temperature range of 50 – 1100 °C. Consequently, the first experimentally derived Δ_{47} – T calibration in a CO₂ gas phase was proposed. This experimental calibration provides a validated base for the standardization of the raw Δ_{47} data. Moreover, heating CO₂ in a pre-humidified quartz tube enables us to easily prepare a CO₂ standard gas of a similar Δ_{47} value to the CO₂ sample (i.e., similar Δ_{47} correction matrix). This will lead to an improvement in the correction scheme of the carbonate clumped isotope thermometry and reliably adjust the absolute Δ_{47} scale.

I dedicate this thesis to the soul of my Dad

Acknowledgements

I am grateful to Almighty Allah for guiding me to conceptualize, develop and complete this dissertation. Without his sufficient grace and mercy, nothing is accomplished.

I would like to express my sincere gratitude and trustful respect to my supervisor, Dr. Sang-Tae Kim, for accepting me as his first PhD student and also for providing me with the tools and funding to succeed. Special thanks to Prof. Henry Schwarcz for his expertise and generous offering of time to discuss my ideas and lab work either by emails or personal meetings which often extended to affect the rest of his daily schedule. I would like to thank Martin Knyf for his endless technical support and also for lending an ear when needed. Martin, I wish you all the best in your coming years of retirement. I am thankful to my committee members, Dr. Eduard Reinhardt and Prof. Derek Ford for their time and insights into my research.

Thank you to my labmates, Chris Spencer, Jillian Wyman, Nick Randazzo and Kesia Ie for their kindest friendship and good times we spent together. Special thanks go to my closest friend Ahmed Ashour who has served as a panacea to my homesickness. Thanks also go out to the staff in the main office, particularly Ann Wallace, Kath Philp and Salomé Santos-Blaguski who have always taken great care of the graduate students.

I am thankful for research funding support provided by Natural Science and Engineering Research Council (NSERC) Discovery Grant, Ontario Ministry of Research and Innovation – Ontario Research Fund (MRI-ORF), Canada Foundation for Innovation – Leaders Opportunity Fund (CFI-LOF), and also McMaster University, through Dr. Sang-Tae Kim.

I am deeply indebted to my dad for his care, hard work and everlasting love. Although he passed away long time ago, his soul is still guiding me. Thanks mom for your advices and prayers which smoothen my life. Finally, I would like to thank my beloved wife, Nahla,

who was so patient and supportive. Nahla, I really appreciate your being there for me throughout the last four years and sorry for the huge stress I accidentally inserted to our life.

-Mohammed

Table of Contents

Abstract	iii
Acknowledgements	vi
Table of Contents	viii
List of Figures	xii
List of Tables	xiv
List of Equations	xv
Contribution of Authors	xvi
Chapter 1 - Introduction	1
Chapter 2 - Carbon and oxygen isotope systematics in cave environments: Lessons from an artificial cave	18
2.1 Abstract.....	19
2.2 Introduction.....	21
2.3 Experimental and analytical Methods.....	26
2.3.1 <i>Experimental Setup</i>	26
2.3.2 <i>Preparation of solutions</i>	29
2.3.3 <i>Stable isotope and other analyses</i>	30
2.4 Results.....	32
2.4.1 <i>Mineralogy and weight of CaCO₃ precipitates</i>	32
2.4.2 <i>DIC concentration, pH and isotopic compositions of drip water and cave CO₂</i>	33
2.4.3 <i>Carbon and oxygen isotope compositions in the precipitated calcite</i>	35
2.4.3.1 <i>Carbon and oxygen isotope compositions of calcite precipitated on the upper watch glasses (stalagmite-like settings)</i>	35
2.4.3.2 <i>Carbon and oxygen isotope compositions of calcite precipitated on the lower watch glasses (pool-like settings)</i>	36
2.5 Discussion.....	37
2.5.1 <i>Temperature and flow rate effects on stalagmite growth rate</i>	39

2.5.2 <i>Chemical and isotopic evolution of drip water</i>	39
2.5.2.1 <i>Chemical evolution in drip water</i>	39
2.5.2.2 <i>Carbon isotope evolution in drip water</i>	40
2.5.2.3 <i>Oxygen isotope evolution in drip water</i>	42
2.5.3 <i>Equilibrium carbon and oxygen isotope fractionations during slow calcite precipitation in pool – like settings</i>	44
2.5.3.1 <i>Equilibrium carbon isotope fractionation between calcite and DIC in lower watch glasses</i>	44
2.5.3.2 <i>Equilibrium oxygen isotope fractionation between calcite and H₂O in lower watch glasses</i>	46
2.5.4 <i>Non-equilibrium carbon and oxygen isotope fractionations during fast calcite precipitation in stalagmite – like settings</i>	49
2.5.4.1 <i>Flow rate and temperature effects on carbon isotope compositions of the calcite precipitated on the upper watch glasses</i>	50
2.5.4.2 <i>Flow rate and temperature effects on oxygen isotope compositions of the calcite precipitated on the upper watch glasses</i>	55
2.5.5 <i>Insights into the debate of equilibrium oxygen isotope fractionation between calcite and water in cave environments</i>	58
2.6 Conclusions.....	61
2.7 Acknowledgements.....	63
2.8 References.....	64
2.9 Tables.....	70
2.10 Figures.....	73
2.11 Supplementary Materials.....	88
Chapter 3 - Speleothem evidence for the greening of the Sahara and its implications for the early human dispersal out of Africa	90
3.1 Abstract.....	91
3.2 Introduction.....	92

3.3 Analytical Methods.....	93
3.4 Timing of speleothem growth in the Wadi Sannur cave.....	94
3.5 Source of paleorainfall and its driving mechanism.....	97
3.6 The green Sahara and the early human dispersal out of Africa.....	102
3.7 Conclusion.....	104
3.8 Acknowledgements.....	104
3.9 References.....	105
3.10 Tables.....	110
3.11 Figures.....	111
3.12 Supplementary Materials.....	116
Chapter 4 - Disordering of ^{13}C-^{18}O bond in CO_2 gas over a heated quartz surface at 50 – 1100 °C: Insights into the abundance of mass 47 (Δ_{47}) in CO_2 gas at thermodynamic equilibrium.....	120
4.1 Abstract.....	121
4.2 Introduction.....	123
4.3 Experimental	126
4.4 Results and Discussion.....	130
4.4.1 <i>Time series experiments</i>	130
4.4.1.1 <i>Carbon and oxygen isotope compositions of the baked CO_2 gases</i>	131
4.4.1.2 <i>Time evolution of Δ_{47} in baked CO_2 gases</i>	132
4.4.2 <i>Effect of the CO_2 cleaning procedures on the raw Δ_{47}</i>	134
4.4.3 <i>Temperature dependence of equilibrium Δ_{47} of CO_2 gas at MRSI</i>	137
4.4.4 <i>Correction and standardization of the raw Δ_{47} – temperature relationship</i>	139
4.4.5 <i>Comparison with the theoretical Δ_{47} – temperature relationship</i>	140
4.4.6 <i>Implications for the correction scheme of the carbonate clumped isotope thermometry</i>	142
4.5 Conclusions.....	144
4.6 Acknowledgments.....	146

4.7 References.....	147
4.8 Tables.....	150
4.9 Figures.....	153
Chapter 5 - Conclusions and outlook.....	163
5.1 Conclusions.....	163
5.2 Outlook.....	167
5.3 References.....	169

List of Figures

Fig. 1.1	9
Fig. 1.2	10
Fig. 2.1	73
Fig. 2.2	74
Fig. 2.3	75
Fig. 2.4	76
Fig. 2.5	77
Fig. 2.6	78
Fig. 2.7	80
Fig. 2.8	81
Fig. 2.9	82
Fig. 2.10	83
Fig. 2.11	84
Fig. 2.12	85
Fig. 2.13	86
Fig. 2.14	87
Fig. 3.1	111
Fig. 3.2	112
Fig. 3.3	113
Fig. 3.4	115
Fig. 4.1	153
Fig. 4.2	154
Fig. 4.3	155
Fig. 4.4	156
Fig. 4.5	157
Fig. 4.6	158
Fig. 4.7	159
Fig. 4.8	161

Fig. 4.9.....162

List of Tables

Table 2.1	70
Table 2.2	71
Table 2.3	72
Table 3.1	110
Table 4.1	150
Table 4.2	151
Table 4.3	152

List of Equations

Eq. 2.1.....	48
Eq. 2.2.....	51
Eq. 2.3.....	52
Eq. 2.4.....	59
Eq. 4.1.....	129
Eq. 4.2.....	130
Eq. 4.3.....	130
Eq. 4.4.....	130
Eq. 4.5.....	130
Eq. 4.6.....	130
Eq. 4.7.....	130
Eq. 4.8.....	132
Eq. 4.9.....	138
Eq. 4.10.....	138
Eq. 4.11.....	138
Eq. 4.12.....	140

Contribution of Authors

Chapter 2 - Carbon and oxygen isotope systematics in cave environments: Lessons from an artificial cave. M.I. EL-Shenawy, S.-T. Kim and H.P. Schwarcz. To be submitted to *Geochimica et Cosmochimica Acta*. M.I. EL-S. designed the experiment, performed chemical and isotopic analyses, interpreted the data. M.I. EL-S. wrote the manuscript with feedback from S.-T.K. and H.P.S.. S.-T. K. conceived the project.

Chapter 3 - Speleothem evidence for the greening of the Sahara and its implications for the early human dispersal out of Africa. M. I. EL-Shenawy, S-T. Kim, H. P. Schwarcz, Y. Asmerom and V. Polyak. Submitted to *Quaternary Science Reviews*. M.I. EL-S. conceived the project, conducted the field work, collected the speleothem samples, carried out oxygen isotope analyses. Y. A. and V. P. performed the U/Th analyses. M.I. EL-S. wrote the manuscript with input from S.-T.K., H.P.S., Y.A. and V. P.

Chapter 4 - Disordering of ^{13}C - ^{18}O bond in CO_2 gas over a heated quartz surface at 50 – 1100 °C: Insights into the abundance of mass 47 (Δ_{47}) in CO_2 gas at thermodynamic equilibrium. M. I. EL-Shenawy and S-T. Kim. To be submitted to *Rapid Communications in Mass Spectrometry*. M.I. EL-S. designed the experiment, conduct the clumped isotope analyses, interpreted the data, and wrote the manuscript with input from S.-T.K.

Chapter 1- Introduction

Speleothem is a family name for secondary cave carbonates (such as stalagmites, stalactites and flowstones) and their formation is a function of water and vegetation availability above the surface of a cave site. The percolation of surface water or rainfall downward through subsurface fractures, cracks and conduits in limestone results in leaching of CaCO_3 in the presence of excess CO_2 (high $p\text{CO}_2$), which is typically made available by the respiration of the plants into the soil. Subsequent degassing of CO_2 from CaCO_3 -saturated seepage water, when this water is exposed to the cave atmosphere (low $p\text{CO}_2$), leads to deposition of speleothems due to the $p\text{CO}_2$ gradient between the seepage water and the cave atmosphere (Schwarcz 1986; Ford and Williams 1989). The availability and variability of water and vegetation are mainly controlled by climate dynamics over cave areas. These climate dynamics (signals) might be recorded in the chemical and isotopic composition of speleothems, which reflect those compositions in parent seepage water. However, deciphering the climate records in speleothems requires proper understanding of the physicochemical processes that controlled the formation, isotopic and chemical composition of speleothems (Hendy, 1971; Fairchild et al., 2009; Dreybrodt and Scholz, 2011).

In the past five decades, speleothems have been recognized as a powerful continental paleoclimate archive because of their robust chronology (U-series dating; Edwards et al., 1987, Li et al., 1989; Cheng et al., 2016), wide geographic distribution (i.e., spans low and high latitudes) and high resolution chemical and isotopic microstratigraphy (e.g., Johnson et al., 2006; Ridley et al., 2015). Historically, the

emphasis of early research on speleothems was on the estimation of paleotemperature based upon oxygen isotope fractionation between carbonate and water (e.g., Harmon et al., 1979; Gasconyne et al., 1980). This quantitative approach requires the knowledge of three aspects: (1) oxygen isotope composition ($\delta^{18}\text{O}$) in fossil drip water trapped as fluid inclusions in speleothems (Schwarcz et al., 1976; Dennis et al., 2001; Vonhof et al., 2006), (2) whether the carbonate formed in isotopic equilibrium (enabling paleotemperature estimation) or in non-equilibrium (discarded for paleothermometry) with their drip water, and (3) the appropriate equation to estimate the formation temperature from the oxygen isotope fractionation determined from speleothems and fossil drip water (e.g., O'Neil et al., 1969; Friedman and O'Neil, 1977; Kim and O'Neil, 1997; Coplen, 2007; Tremaine et al., 2011). The latter two aspects are ambiguous and controversial, thus hampering the estimation of paleotemperatures in speleothem-based records. For instance, the "Hendy test" has been utilized as a routine test to check isotopic non-/equilibrium in ancient speleothems. However, performing Hendy test on few growth layers in an individual stalagmite does not guarantee the deposition of the whole stalagmite in isotopic equilibrium. Moreover, the main criteria for Hendy test (i.e., no correlation between $\delta^{18}\text{O}$ and $\delta^{13}\text{C}$ in carbonates along a single growth layer) might falsely indicate isotopic equilibrium in a small radius stalagmite or a short selected transect within stalagmite apex (few centimeters). On the other hand, the use of different oxygen isotope fractionation equations available in the literature (i.e., Kim and O'Neil, 1997; Coplen, 2007) to estimate paleotemperature in a same carbonate sample can result

in a discrepancy of 8 °C, which is equivalent to the temperature difference between glacial/interglacial cycles.

Due to the aforementioned complexities in the estimation of paleotemperature in speleothems, recent research on speleothems focuses on qualitative interpretations (e.g., wet/dry) of their well-dated stable isotope records. These qualitative interpretations were mainly used for transferring the speleothems chronology to the marine isotope records to constrain the timing of the terminations of the ice ages (e.g., Cheng et al., 2009; Grant et al., 2012; Chang et al., 2016), identifying the climate forcing factors by allowing direct comparison with natural and anthropogenic phenomenon without implementing orbital tuning (Wang et al., 2008; Cheng et al., 2012; Ridely et al., 2015) and detecting the teleconnections in the global climate system (Wang et al., 2001; Yuan et al., 2004; Asmerom et al., 2010; Cheng et al., 2016). However, stable isotope signals ($\delta^{18}\text{O}$ and $\delta^{13}\text{C}$) in speleothems might be influenced by large kinetic isotope effects (Mickler et al., 2006). These kinetic isotope effects can either amplify or mask the climate signals in speleothems (e.g., McDermott, 2004; Van Rangelbergh et al., 2015). For example a small dry event relative to normal conditions in a specific area might be interpreted as a megadrought event, or a few degrees increase in temperature above a cave site might be masked (cancelled) in a kinetically influenced stable isotope ($\delta^{18}\text{O}$ and $\delta^{13}\text{C}$) records from a stalagmite. Moreover, these kinetic isotope effects imbue the speleothem-based paleoclimate records with uncertainties that reduce the significance of any exclusive conclusions from these records.

To enable the robust quantitative and qualitative interpretation of carbon and oxygen isotope records in speleothems, the speleothem community needs to fill the gap of knowledge regarding the following topics:

- (1) How to identify isotope equilibrium in ancient or modern speleothems and what are the conditions at which speleothems grow in isotopic equilibrium?
- (2) What are the true equilibrium carbon and oxygen isotope fractionation factors between carbonate and drip water in cave environments?
- (3) What are the source(s), magnitude and direction(s) of potential kinetic carbon and oxygen isotope effects in speleothems?
- (4) What are the possible ways to quantify kinetic carbon and oxygen isotope effects in speleothem-based records and extract purely climate-driven information?

In chapter 2 of this Ph.D. thesis, a series of laboratory experiments were conducted under cave-analogue conditions in an artificial cave to simulate the formation of speleothems and to study carbon and oxygen isotope systematics in cave environments. These laboratory experiments were performed under tightly controlled conditions (i.e., cave temperature, flow rate, relative humidity and $p\text{CO}_2$ of cave atmosphere). The mineralogy of the synthetic speleothems in this study (i.e., equivalent to stalagmites and pool carbonates) was mostly calcite, which was precipitated by CO_2 degassing due to the $p\text{CO}_2$ gradient between the carbonate-saturated drip water and the cave atmosphere. Two speleothem-like deposits, pool-like calcite and stalagmite-like calcite, were simulated in this study. The pool-like calcite was slowly precipitated, allowing the calcite formation at isotopic equilibrium. As a result, carbon and oxygen isotope equilibrium fractionation

factors between calcite and drip water were measured. These experimentally determined isotope fractionation factors can be used not only to identify isotopic equilibrium in modern farmed calcite in cave settings, but also to estimate paleotemperature in ancient speleothems formed at their oxygen isotope equilibrium.

In contrast, stalagmite-like calcite, precipitated rapidly, was out of isotopic equilibrium. Larger carbon and oxygen isotope fractionation factors were observed in the stalagmites than those determined from pool-like calcite. The flow rate of the drip water over a stalagmite apex appears to be the major controlling factor for these large kinetic isotope effects. The magnitude of the kinetic isotope effects increases with decreasing the flow rate and vice versa. The flow rate-induced kinetic oxygen isotope effects explain the current discrepancy among the the published equilibrium $1000\ln^{18}\alpha_{\text{C-C-H}_2\text{O}}$ values (e.g., Coplen, 2007; Tremaine et al., 2011) and the observed $1000\ln^{18}\alpha_{\text{C-C-H}_2\text{O}}$ variability in modern farmed calcite from natural cave settings. Finally, the results of this study open a new window to quantify kinetic oxygen isotope effects recorded in ancient speleothems and thus to reconstruct paleotemperature.

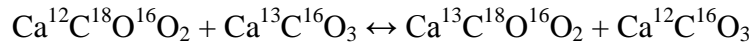
The greening periods (i.e., extensive rainfall and vegetation) in the Sahara had been inferred from surface continental (i.e., lacustrine and travertine deposits) and marine archives (Gaven et al., 1981; Crombie et al., 1997; Schwarcz and Morawska, 1993; Smith, 2012; Osborne et al., 2008; Castañeda et al., 2009; de Menocal, 2013). These greening periods were essential to permit early human migration out of Africa via the Sahara. However, the timing, spatial extension and moisture source of the green Sahara

periods are still in dispute due to the extensive weathering in the Sahara region that affects the lacustrine deposits as well as the lack of age constraints on the marine archives (i.e., Milankovitch tuning). Speleothems are terrestrial carbonate deposits formed in caves and they are isolated from various surface weathering processes and can be independently dated by U/Th technique back to 500 Ka. Therefore, speleothem growth in the Sahara can be a powerful geological proxy for the greening of the Sahara.

In chapter 3 a double stalagmite (WS-5d) was collected from the Wadi Sannur cave (central Egypt) in the northeastern Sahara desert. The growth of WS-5d stalagmite indicates the availability of water and vegetation in the Sahara and thereby, the U/Th dates in this stalagmite identify the timing of the greening conditions in the Sahara. In addition, the oxygen isotope compositions collected from the WS-5d stalagmite were used to track the moisture source above the Wadi Sannur cave (28 ° N). The distance between the moisture source and the location of the Wadi Sannur cave was used to investigate the spatial extension of the greening in the Sahara. Furthermore, the correlation between the chronology of the WS-5d stalagmite and the paleodata of summer insolation and CO₂ concentrations enabled us to identify the climate forcing factors for the greening of the Sahara. Collectively, the results of this study have significant implications for the understanding of climate changes on the human dispersal out of Africa.

In the 2000's, the Caltech group developed a new isotope-based (i.e., Δ_{47}) paleothermometer, carbonate clumped isotope thermometry, that relates the abundance of

mass 47 in carbonate-derived CO₂ to the formation temperature of formation of the carbonate minerals (Ghosh et al., 2006; Schabule et al., 2006). Unlike the conventional carbonate-water oxygen isotope thermometry, the Δ_{47} – temperature relationship does not require any knowledge of the oxygen isotope composition of water (liquid phase) because it relies on a following homogeneous isotope exchange reaction:



Under isotopic equilibrium, this reaction at low temperatures proceeds to the right direction, resulting high Δ_{47} values in the CO₂ liberated by the acid digestion of carbonates, whereas the reaction favors the left direction approaching the stochastic distribution ($\Delta_{47} = 0$ ‰) at high temperatures (Schauble et al., 2006; Guo et al., 2009). Although carbonate clumped isotope thermometry (Δ_{47}) holds great promise for reconstructing paleotemperature using speleothems, challenges, such as uncertainties in the standardization of Δ_{47} measurements (Huntington et al., 2009; Dennis et al., 2011), calibration of Δ_{47} – T relationship (e.g., Ghosh et al., 2006; Dennis and Schrag, 2010) and the systematics of Δ_{47} in speleothems (Affek et al., 2008; Daëron et al., 2011; Affek and Zaarur, 2014; Affek et al., 2014), remain unresolved.

The standardization of Δ_{47} measurements was originally carried out by comparing the measured Δ_{47} values in carbonate-derived CO₂ gases with heated CO₂ gases at 1000 °C that are assumed to be at their stochastic distribution (i.e., $\Delta_{47} = 0$ ‰; Ghosh et al., 2006; Huntington et al., 2009). Using the heated gas standardization or one point standardization approach, as can be seen in Fig. 1.1, Dennis and Schrag (2010) showed an excellent agreement between their experimental calibration of the carbonate clumped

isotope thermometry and the theoretical models by Schauble et al. (2006) and Guo et al. (2009). However, the Δ_{47} value of the heated gases is out of the range of those measured in the carbonate-derived CO_2 samples (i.e., different Δ_{47} correction matrix). This can cause a systematic error in the corrected Δ_{47} value of a measured CO_2 sample if any Δ_{47} -dependent artifacts caused by the mass spectrometric analysis and/or the preparation procedures exist.

Dennis et al. (2011) suggested that the fragmentation and recombination of the CO_2^+ ions in the ion source of the isotope ratio mass spectrometer artificially affect the measured Δ_{47} value of CO_2 gas based upon the deviation of the measured CO_2 gas from the stochastic distribution (scrambling effect). This so called ‘scrambling effect’ has been thought to shift the measured Δ_{47} value toward the stochastic distribution and its magnitude increases with increasing the Δ_{47} value of the CO_2 gas (Dennis et al., 2011). However, it is unclear whether the scrambling effect arises in the ion source and/or during the purification procedures of the CO_2 . Regardless the source of the scrambling effect, Dennis et al. (2011) proposed a new “multiple-point standardization” approach that normalizes the measured Δ_{47} values of carbonate-derived CO_2 samples on the basis of an empirical transfer function (ETF). This ETF is created by plotting the measured Δ_{47} values of CO_2 gases heated at 1000 °C as well as CO_2 gases equilibrated with H_2O against their corresponding Δ_{47} values predicted by the theoretical work of Wang et al. (2004). Although this new approach enables a direct comparison of the reported Δ_{47} values from different laboratories (Dennis et al., 2011, Tang et al., 2014), the theoretical predictions (i.e., Wang et al., 2004) used in this approach have not yet been experimentally tested.

Recent studies show that different theoretical models yielded 0.01 to 0.1 ‰ discrepancy in the predicted Δ_{47} values (Hill et al., 2013; Webb and Miller, 2014). Furthermore, when the experimental calibration of the carbonate clumped isotope thermometry by Dennis and Schrag (2010) is projected based on the new multiple-point standardization approach, a large offset between the experimental and theoretical calibrations of the carbonate clumped isotope thermometry is observed (Dennis et al., 2011; Fig. 1.1).

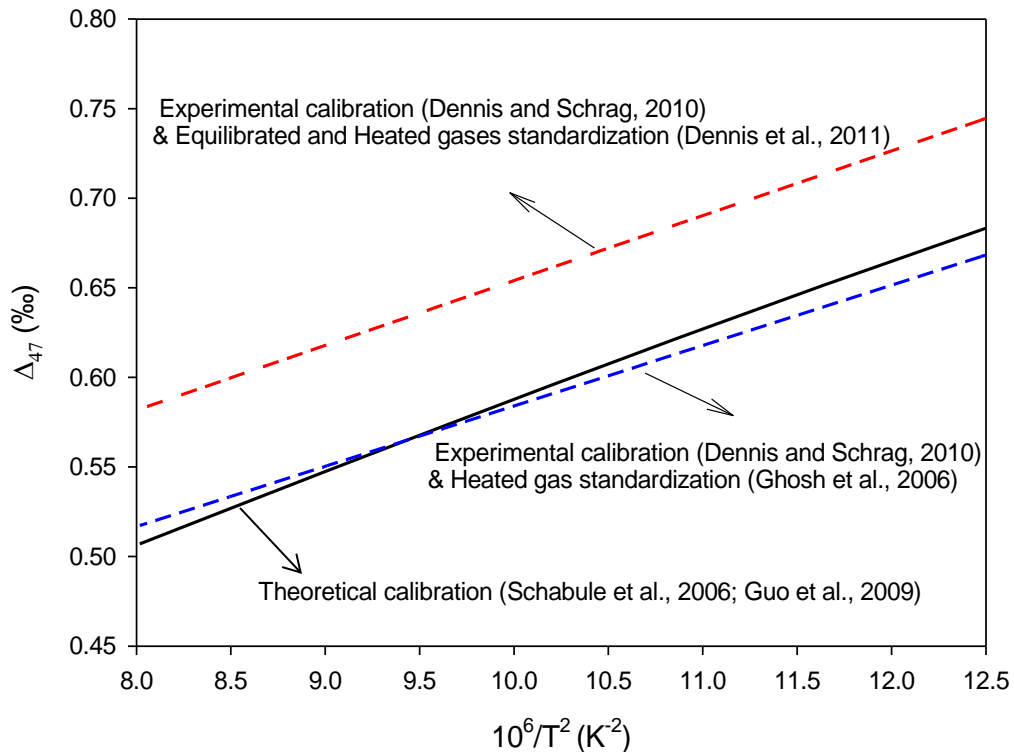


Fig. 1.1: The sensitivity of the carbonate clumped isotope thermometry calibration to the standardization method.

In addition to the aforementioned standardization issues, the Δ_{47} - T calibration of the carbonate clumped isotope thermometry is still a matter of debate. It is not clear

whether the slope of this calibration is steep (e.g., Ghosh et al., 2006; Zaarur et al., 2013) or shallow (e.g., Dennis and Schrag, 2010) (Fig. 1.2).

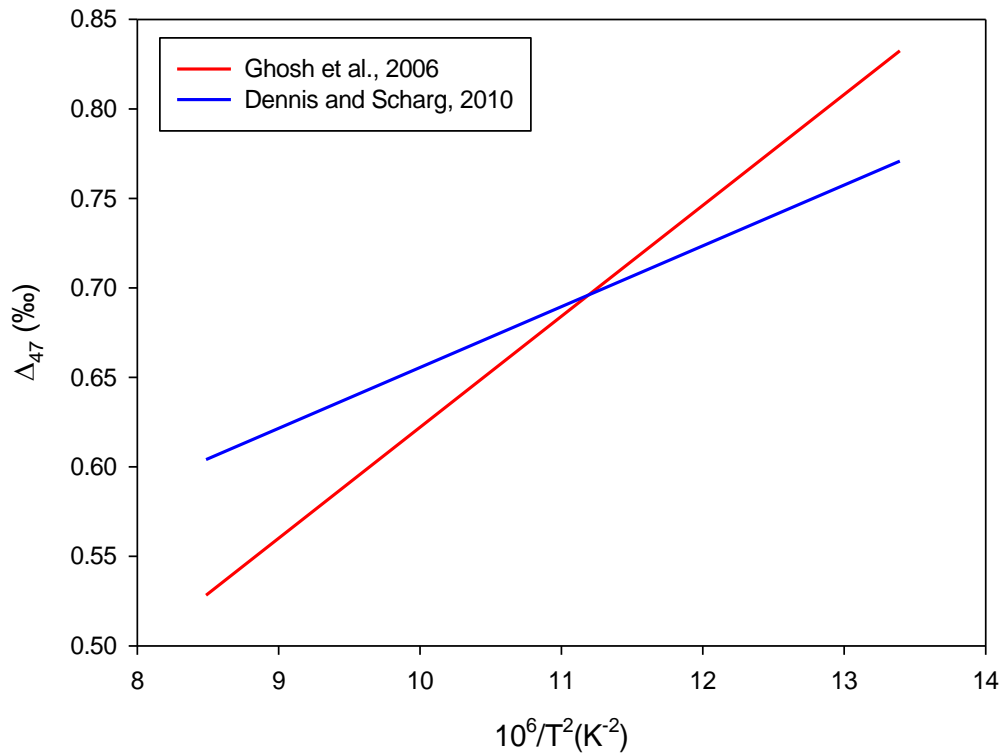


Fig. 1.2: The discrepancy in Carbonate clumped isotope thermometry calibration. Δ_{47} values are corrected following Dennis et al. (2011).

As a result, one could not be certain whether the carbonate precipitated at its clumped isotope equilibrium or not. For instance, if the steep slope calibration (Ghosh et al., 2006; Zaarur et al., 2013) was used to evaluate Δ_{47} systematics of speleothems, the measured Δ_{47} values in modern speleothems would be out of clumped isotope equilibrium (i.e., lower than the equilibrium Δ_{47} at a given temperature). In contrast, using the shallow

slope calibration (e.g., Dennis and Schrag, 2010) appears to indicate clumped isotope equilibrium in (some) reported Δ_{47} data from modern speleothems (Affek et al., 2008; Daëron et al., 2011; Kluge and Affek, 2012; Affek et al., 2014). It should be noted that the discussion of the published clumped isotope data from speleothem samples in the light of the shallow slope calibration was overlooked in the literature (e.g., Affek and Zaarur, 2014; Affek et al., 2014). In summary, the standardization of Δ_{47} measurements and the calibration of $\Delta_{47} - T$ relationship should be investigated further before the utilization of the clumped isotope techniques in speleothem science to accurately reconstruct paleotemperatures or the oxygen isotope composition of paleorainfall.

Chapter 4 of this Ph.D. thesis deals with the following two topics on the standardization of Δ_{47} measurements:

- (1) The validity of the theoretically predicted Δ_{47} values by Wang et al. (2004) used in the ETF.
- (2) The source and magnitude of the scrambling effect in the clumped isotope facility of McMaster Research Group for Stable Isotopologues (MRSI).

To tackle the first topic, a series of two-step experiments were carried out where pre-cleaned CO_2 gases were heated in pre-dehumidified quartz tubes for chosen periods of time to measure their Δ_{47} values. In the first step of the experiment, the kinetics of Δ_{47} in heated CO_2 was studied at 50, 100, 491 and 1000 °C to define the time required for the heated CO_2 gases to reach their respective thermodynamic equilibrium (i.e., equilibration time for Δ_{47}). Second, the equilibration times were used to construct the $\Delta_{47} - \text{temperature}$

relationship for three CO₂ gases of different isotopic compositions between 50 and 1100 °C. The results of the two-step experiments present the first experimental calibration of the Δ_{47} – temperature relationship in a CO₂ gas phase. In addition, another experiment was conducted to detect the source and magnitude of the scrambling effect in the clumped isotope facility at MRSI. CO₂ gases without prior cleaning procedures were heated to attain thermodynamic equilibrium at 100, 200 and 1000 °C. Subsequently they were cleaned and measured for their Δ_{47} values. A comparison with the two-step experiments demonstrates that the cleaning procedures are the most likely cause for the scrambling effect. The results of Chapter 4 are expected to improve the multiple-point standardization approach initially proposed by Dennis et al. (2011).

Chapter 5 provides a summary of my Ph.D. research and an outlook for future research from Chapters 2, 3 and 4.

References

- Affek H. P., Bar-Matthews M., Ayalon A., Matthews A. and Eiler J. M. (2008) Glacial/interglacial temperature variations in Soreq cave speleothems as recorded by “clumped isotope” thermometry. *Geochim. Cosmochim. Acta* **72**, 5351–5360.
- Affek H. P. and Zaarur S. (2014) Kinetic isotope effect in CO₂ degassing: insight from clumped and oxygen isotopes in laboratory precipitation experiments. *Geochim. Cosmochim. Acta* **143**, 319–330.
- Affek H.P. Ayalon A., Bar-Matthews M., Bursteyn Y., Matthews A. and Zaarur S. (2014) Accounting for kinetic isotope effects in Soreq Cave (Israel) speleothems. *Geochim. Cosmochim. Acta* **143**, 303–318.
- Asmerom Y., Polyak V. J. and Burns S. J. (2010) Variable winter moisture in the southwestern United States linked to rapid glacial climate shifts. *Nat. Geosci.* **3**, 114–117.
- Castañeda I. S., Mulitza S., Schefuss E., Lopes dos Santos R. A, Sinninghe Damsté J. S. and Schouten S. (2009) Wet phases in the Sahara/Sahel region and human migration patterns in North Africa. *Proc. Natl. Acad. Sci. U. S. A.* **106**, 20159–20163.
- Cheng H., Edwards R. L., Broecker W. S., Denton G. H., Kong X., Wang Y., Zhang R. and Wang X. (2009) Ice Age Terminations. *Science* **326**, 248–252.
- Cheng H., Edwards R. L., Sinha A., Spötl C., Yi L., Chen S., Kelly M., Kathayat G., Wang X., Li X., Kong X., Wang Y., Ning Y. and Zhang H. (2016) The Asian monsoon over the past 640,000 years and ice age terminations. *Nature* **534**, 640–646.
- Cheng H., Sinha A., Wang X., Cruz F. W. and Edwards R. L. (2012) The Global Paleomonsoon as seen through speleothem records from Asia and the Americas. *Clim. Dyn.* **39**, 1045–1062.
- Coplen T. B. (2007) Calibration of the calcite-water oxygen-isotope geothermometer at Devils Hole, Nevada, a natural laboratory. *Geochim. Cosmochim. Acta* **71**, 3948–3957.
- Crombie M. K., Arvidson R. E., Struchio N. C., El Alfy Z. and Abu Zied K. (1997) Age and isotopic constraints on Pleistocene episodes in the Western Desert, Egypt. *Palaeogeogr. Palaeoclimatol. Palaeoecol.* **130**, 337–355.

- Daëron M., Guo W., Eiler J., Genty D., Blamart D., Boch R., Drysdale R., Maire R., Wainer K. and Zanchetta G. (2011) $^{13}\text{C}^{18}\text{O}$ clumping in speleothems: Observations from natural caves and precipitation experiments. *Geochim. Cosmochim. Acta* **75**, 3303–3317.
- Dennis K. J., Affek H. P., Passey B. H., Schrag D. P. and Eiler J. M. (2011) Defining an absolute reference frame for “clumped” isotope studies of CO_2 . *Geochim. Cosmochim. Acta* **75**, 7117–7131.
- Dennis K. J. and Schrag D. P. (2010) Clumped isotope thermometry of carbonatites as an indicator of diagenetic alteration. *Geochim. Cosmochim. Acta* **74**, 4110–4122.
- Dennis P. F., Rowe P. J. and Atkinson T. C. (2001) The recovery and isotopic measurement of water from fluid inclusions in speleothems. *Geochim. Cosmochim. Acta* **65**, 871–884.
- Derricourt R. (2005) Getting “Out of Africa”: Sea crossings, land crossings and culture in the Hominin migrations. *J. World Prehistory* **19**, 119–132.
- Dreybrodt W. and Scholz D. (2011) Climatic dependence of stable carbon and oxygen isotope signals recorded in speleothems: From soil water to speleothem calcite. *Geochim. Cosmochim. Acta* **75**, 734–752.
- Fairchild I. J. and Treble P. C. (2009) Trace elements in speleothems as recorders of environmental change. *Quat. Sci. Rev.* **28**, 449–468.
- Ford D. and Williams P. D. (2007) Karst hydrogeology and geomorphology. Wiley, Chichester.
- Friedman I. and O’Neil J. R. (1977) Compilation of stable isotope fractionation factors of geochemical interest. *Geolog. Surv. Prof. Paper 440-KK*, pp. 117.
- Gascoyne M., Schwarcz H. P. and Ford D. C. (1980) A paleotemperature record for the mid-Wisconsin in Vancouver Island. *Nature* **285**, 474–476.
- Gaven C., Hillaire-Marcel C., Petit-Maire N. (1981) A Pleistocene lacustrine episode in southeastern Libya. *Nature* **290**:131–133.
- Ghosh P., Adkins J., Affek H., Balta B., Guo W., Schauble E. A., Schrag D. and Eiler J. M. (2006) $^{13}\text{C}^{18}\text{O}$ bonds in carbonate minerals: A new kind of paleothermometer. *Geochim. Cosmochim. Acta* **70**, 1439–1456.

- Grant K. M., Rohling E. J., Bar-Matthews M., Ayalon A., Medina-Elizalde M., Ramsey C. B., Satow C. and Roberts A. P. (2012) Rapid coupling between ice volume and polar temperature over the past 150,000 years. *Nature* **491**, 744–747.
- Guo W., Mosenfelder J. L., Goddard W. A. and Eiler J. M. (2009) Isotopic fractionations associated with phosphoric acid digestion of carbonate minerals: Insights from first-principles theoretical modeling and clumped isotope measurements. *Geochim. Cosmochim. Acta* **73**, 7203–7225.
- Hendy C. (1971) The isotopic geochemistry of speleothems - I. The calculation of the effects of different modes of formation on the isotopic composition of speleothems and their applicability as paleoclimatic indicators. *Geochim. Cosmochim. Acta* **35**, 801–824.
- Hill P. S., Tripathi A. K. and Schauble E. A. (2014) Theoretical constraints on the effects of pH, salinity, and temperature on clumped isotope signatures of dissolved inorganic carbon species and precipitating carbonate minerals. *Geochim. Cosmochim. Acta* **125**, 610–652.
- Huntington K. W., Eiler J. M., Affek H. P., Guo W., Bonifacie M., Yeung L. Y., Thiagarajan N., Passey B., Tripathi a, Daëron M. and Came R. (2009) Methods and limitations of “clumped” CO₂ isotope (Delta47) analysis by gas-source isotope ratio mass spectrometry. *J. Mass Spectrom.* **44**, 1318–29.
- Johnson K. R., Hu C., Belshaw N. S. and Henderson G. M. (2006) Seasonal trace-element and stable-isotope variations in a Chinese speleothem: The potential for high-resolution paleomonsoon reconstruction. *Earth Planet. Sci. Lett.* **244**, 394–407.
- Kim S.-T. and O’Neil J. (1997) Equilibrium and nonequilibrium oxygen isotope effects in synthetic carbonates. *Geochim. Cosmochim. Acta* **61**, 3461–3475.
- Kluge T., John C. M., Jourdan A. L., Davis S. and Crawshaw J. (2015) Laboratory calibration of the calcium carbonate clumped isotope thermometer in the 25-250°C temperature range. *Geochim. Cosmochim. Acta* **157**, 213–227.
- Lawrence Edwards R., Chen J. H. and Wasserburg G. J. (1987) ²³⁸U-²³⁴U-²³⁰Th-²³²Th systematics and the precise measurement of time over the past 500,000 years. *Earth Planet. Sci. Lett.* **81**, 175–192.
- Li W.-X., Lundberg J., Dickin a. P., Ford D. C., Schwarcz H. P., McNutt R. and Williams D. (1989) High-precision mass spectrometric uranium-series dating of cave deposits and implications for paleoclimate studies. *Nature* **339**, 534–536.

- McDermott F. (2004) Palaeo-climate reconstruction from stable isotope variations in speleothems: A review. *Quat. Sci. Rev.* **23**, 901–918.
- De Menocal P. B. (2013) Marine Sediment Records of African Climate Change: Progress and Puzzles. *Treatise Geochemistry Second Ed.* **14**, 99–108.
- Mickler P. J., Stern L. A. and Banner J. L. (2006) Large kinetic isotope effects in modern speleothems. *Bull. Geol. Soc. Am.* **118**, 65–81.
- Osborne A., Vance D., Rohling E., Barton N., Rogerson M., Fello N. (2008) A humid corridor across the Sahara for the migration of early modern humans out of Africa 120,000 years ago. *Proc. Natl. Acad. Sci. U. S. A.* **105**, 16444–16447.
- O’Neil J., Clayton R. and Mayeda T. (1969) Oxygen Isotope Fractionation in Divalent Metal Carbonates. *J. Chem. Phys.* **51**, 5547–5558.
- Van Rampelbergh M., Fleitmann D., Verheyden S., Cheng H., Edwards L., De Geest P., De Vleeschouwer D., Burns S. J., Matter A., Claeys P. and Keppens E. (2013) Mid-to late Holocene Indian Ocean Monsoon variability recorded in four speleothems from Socotra Island, Yemen. *Quat. Sci. Rev.* **65**, 129–142.
- Ridley H. E., Asmerom Y., Baldini J. U. L., Breitenbach S. F. M., Aquino V. V., Pruffer K. M., Culleton B. J., Polyak V., Lechleitner F. A., Kennett D. J., Zhang M., Marwan N., Macpherson C. G., Baldini L. M., Xiao T., Peterkin J. L., Awe J. and Haug G. H. (2015) Aerosol forcing of the position of the intertropical convergence zone since ad 1550. *Nat. Geosci.* **8**, 195–200.
- Schauble E. A., Ghosh P. and Eiler J. M. (2006) Preferential formation of ^{13}C - ^{18}O bonds in carbonate minerals, estimated using first-principles lattice dynamics. *Geochim. Cosmochim. Acta* **70**, 2510–2529.
- Schwarcz H. P., Harmon R. S., Thompson P. and Ford D. C. (1976) Stable isotope studies of fluid inclusions in speleothems and their paleoclimatic significance. *Geochim. Cosmochim. Acta* **40**, 657–665.
- Schwarcz H. P. (1986) Geochronology and isotopic geochemistry of speleothems. *Handbook Environ. Isotope Geochem.* **2**, 271–303.
- Schwarcz H. and Morawska L. (1993) Uranium-series dating of carbonates from Bir Tarfawi and Bir Sahara East. In *Egypt During the Last Interglacial: The Middle Paleolithic of Bir Tarfawi and Bir Sahara East* (eds. F. Wendorf, R. Schild, R. and A.E. Close). New York, Plenum Press, , pp. 205–217.

- Smith J. R. (2012) Spatial and temporal variations in the nature of Pleistocene pluvial phase environments across North Africa. In *Modern Origins: A North African Perspective* (eds. J. J. Hublin and S. P. McPherron). Springer. 35–47.
- Tang J., Dietzel M., Fernandez A., Tripathi A. K. and Rosenheim B. E. (2014) Evaluation of kinetic effect on clumped isotope fractionation (Δ_{47}) during inorganic calcite precipitation. *Geochim. Cosmochim. Acta* **134**, 120–136.
- Tremaine D. M., Froelich P. N. and Wang Y. (2011) Speleothem calcite farmed in situ: Modern calibration of $\delta^{18}\text{O}$ and $\delta^{13}\text{C}$ paleoclimate proxies in a continuously-monitored natural cave system. *Geochim. Cosmochim. Acta* **75**, 4929–4950.
- Vonhof H. B., Breukelen M. R. Van, Postma O., Rowe P. J., Atkinson T. C. and Kroon D. (2006) A continuous-flow crushing device for on-line d 2 H analysis of fluid inclusion water in speleothems. *Rapid Commun. Mass Spectrom.*, 2553–2558.
- Wang Y., Cheng H., Edwards R. L., Kong X., Shao X., Chen S., Wu J., Jiang X., Wang X. and An Z. (2008) Millennial- and orbital-scale changes in the East Asian monsoon over the past 224,000 years. *Nature* **451**, 1090–3.
- Wang Y. J. (2001) A High-Resolution Absolute-Dated Late Pleistocene Monsoon Record from Hulu Cave, China. *Science* **294**, 2345–2348.
- Wang Z., Schauble E. and Eiler J. M. (2004) Equilibrium thermodynamics of multiply substituted isotopologues of molecular gases. *Geochim. Cosmochim. Acta* **68**, 4779–4797.
- Webb M. A. and Miller T. F. (2014) Position-specific and clumped stable isotope studies: Comparison of the urey and path-integral approaches for carbon dioxide, nitrous oxide, methane, and propane. *J. Phys. Chem. A* **118**, 467–474.
- Yuan D., Cheng H., Edwards R. L., Dykoski C. a, Kelly M. J., Zhang M., Qing J., Lin Y., Wang Y., Wu J., Dorale J. a, An Z. and Cai Y. (2004) Timing, duration, and transitions of the last interglacial Asian monsoon. *Science* **304**, 575–578.
- Zaarur S., Affek H. P. and Brandon M. T. (2013) A revised calibration of the clumped isotope thermometer. *Earth Planet. Sci. Lett.* **382**, 47–57.

Chapter 2 - Carbon and oxygen isotope systematics in cave environments: Lessons from an artificial cave

Mohammed I. EL-Shenawy^{1,2}, Sang-Tae Kim¹, and Henry P. Schwarcz¹

¹School of Geography and Earth Sciences, McMaster University, 1280 Main Street West, Hamilton, ON, L8S 4K1, Canada

²Department of Geology, Beni-Suef University, Beni- Suef, 62511, Egypt

To be submitted to *Geochimica et Cosmochimica Acta*

2.1 Abstract

Understanding carbon and oxygen isotope systematics in cave environments is a prerequisite to the interpretation of these stable isotopes in speleothem-based paleoclimate records. Here we present a new series of reproducible experiments under tightly controlled laboratory conditions (i.e., temperature, relative humidity, solution chemistry, flow rate and cave $p\text{CO}_2$), simulating the growth of speleothems in natural cave settings. In these experiments, solutions of low calcium carbonate concentration ($\text{Ca}^{2+} = 2 \text{ mmol/L}$) flowed along a three-step glass path, similar to a stalactite-stalagmite-pool route in natural caves, forming a thin water film that allowed CO_2 degassing and CaCO_3 precipitation as a result of the $p\text{CO}_2$ gradient between the solution and ambient cave atmosphere. The experiments were conducted at three temperatures (15, 25 and 32 °C) and three different flow rates (700, 270 and 125 mL/d) of a fixed drop volume of 0.16 mL.

Our results show that the growth rate of calcite on the stalagmite-like settings increases linearly with increasing flow rate and/or temperature. However, the contribution of each factor (i.e., flow rate or temperature) to the growth rate depends proportionally on the strength of the other factor. The $\delta^{13}\text{C}$ and $\delta^{18}\text{O}$ of calcite formed on the stalagmite-like settings substantially increases with decreasing flow rate (corresponding to increasing flow time) at a given temperature, indicating non-equilibrium isotopic fractionation between calcite and water. Nevertheless, these non-equilibrium isotopic fractionations still demonstrate apparent temperature dependency under a constant flow rate. This suggests that non-equilibrium isotope effects in natural stalagmites might be used to

provide useful qualitative paleoclimate information (such as differentiating wet/dry and warm/cold climate conditions). The non-equilibrium carbon and oxygen isotope effects in the stalagmite-like settings were most likely caused by rapid CO₂ degassing and CaCO₃ precipitation that rapidly consume the DIC reservoir in the thin water film. Furthermore, coherent CO₂ exchange between the carbonate species and cave atmosphere amplified the observed non-equilibrium carbon isotope effects.

In contrast, the calcite in the pool-like settings slowly precipitated at, or close to, isotopic equilibrium with water regardless of the flow rate. It was determined that the slow precipitation rate maintained average temperature-independent carbon isotope fractionation factor between calcite and bicarbonate ($1.7 \pm 0.7 \text{ ‰}$). Conversely, this slow precipitation of calcite allowed oxygen isotope exchange between carbonate species and water resulting in the following temperature-dependent fractionation factor between calcite and water:

$$1000\ln^{18}\alpha_{\text{Cc-H}_2\text{O}} = 18.33 (10^3/T) - 33.14 \quad R^2 = 0.97; P < 0.0001$$

This expression supports the modified $1000\ln^{18}\alpha_{\text{Cc-H}_2\text{O}}$ from Kim and O'Neil (1997) using the acid fractionation factor in Sharma and Clayton (1965). Along with the maximum non-equilibrium deviation at the stalagmite-like settings, equilibrium $1000\ln^{18}\alpha_{\text{Cc-H}_2\text{O}}$ achieved in the pool-like settings can account for the discrepancy in the published expressions for $1000\ln^{18}\alpha_{\text{Cc-H}_2\text{O}}$ (e.g., Coplen, 2007; Tremaine et al., 2011) and the observed variability of $1000\ln^{18}\alpha_{\text{Cc-H}_2\text{O}}$ in modern farmed calcite from natural cave settings.

2.2 Introduction

Stable isotope signals in cave carbonates (speleothems) have widely been used to decipher climate changes in the past. Carbon isotopes ($\delta^{13}\text{C}_{\text{Cc}}$) in speleothems are used to infer changes in vegetation types (i.e., C3 and C4; Dorale et al., 1998), vegetation density (Baldini et al., 2005) and alternating arid/wet conditions (Ridley et al., 2015) above cave sites. Moreover, oxygen isotope compositions of speleothems ($\delta^{18}\text{O}_{\text{Cc}}$) are interpreted as a paleorainfall amount/source proxy (Wang, 2005; Asmerom et al., 2010) and paleotemperature proxy (Gascoyne et al., 1980; van Breukelen et al., 2008). The climatic changes above the cave can be decoded from the $\delta^{13}\text{C}_{\text{Cc}}$ and $\delta^{18}\text{O}_{\text{Cc}}$ signals in speleothems either when speleothems form in isotopic equilibrium with cave drip water (Hendy, 1971) or when none-equilibrium isotope effects associated with various in-cave processes are properly understood (Mühlinghaus et al., 2007; Mühlinghaus et al., 2009; Dreybrodt and Scholz, 2011; Deininger et al., 2012).

Heretofore, there have been two general approaches to evaluate equilibrium/non-equilibrium isotope effects in speleothems. The first approach is used for modern speleothems where a direct comparison can be made between the isotopic fractionation determined from actively growing modern speleothems and that from empirical (Deines et al., 1974; Coplen, 2007; Tremaine et al., 2011) or experimental studies (e.g., O'Neil et al., 1969; Romanek et al., 1992; Kim and O'Neil, 1997; Mook, 2000). Although, in theory, the equilibrium isotope fractionation factor between calcite and water or DIC at certain CaCO_3 growth conditions must be a single value, there are still significant discrepancies in this quantity among theoretical (e.g., Horita and Clayton, 2007; Chacko

and Deines, 2008), empirical, and experimental studies. Consequently, identifying equilibrium/non-equilibrium isotopic effects in modern speleothems, based upon this approach, appears to be dependent on the preference of an individual researcher (e.g., Bar-Matthews et al., 1996; Mickler et al., 2004; Riechelmann et al., 2013; Feng et al., 2014).

The second approach is conducting the following two tests on fossil speleothems: (1) Hendy test (Hendy, 1971) and (2) Replication test (Dorale and Liu, 2009). In Hendy test, isotopic equilibrium is inferred from the absence of significant correlations between $\delta^{13}\text{C}_{\text{Cc}}$ and $\delta^{18}\text{O}_{\text{Cc}}$ along an individual growth layer and/or a growth axis in a stalagmite. However, a positive correlation between $\delta^{13}\text{C}_{\text{Cc}}$ and $\delta^{18}\text{O}_{\text{Cc}}$ along a growth layer could be observed even under isotopic equilibrium conditions because a slower oxygen isotope exchange effect between DIC species and water (Beck et al., 2005) allows carbon and oxygen isotope signals behave similarly (i.e., concurrent enrichments in ^{13}C and ^{18}O). Therefore, isotopic equilibrium might occur at a stalagmite's apex but not at its flanks. Moreover, climatic-driven variability in vegetation, temperature and rainfall amount might result in a coherent correlation between $\delta^{13}\text{C}_{\text{Cc}}$ and $\delta^{18}\text{O}_{\text{Cc}}$ along the growth axis of a stalagmite (Dorale et al., 1998; Hellstrom et al., 1998). As a result, the Hendy test may not be adequate to verify the suitability of ancient stalagmites for paleoclimate studies (Mickler et al., 2006; Dorale and Liu, 2009). Alternatively, Dorale et al. (1998) introduced the replication test to evaluate isotopic equilibrium in ancient speleothems. This test relies on the replication of a stable isotope record from two or more stalagmites within the same cave. However, the replication test does not rule out the kinetic isotope

effects of a similar magnitude during stalagmite formation (Dorale and Liu, 2009). For example, identical kinetic carbon and oxygen isotope effects have been observed in farmed calcite from cave monitoring programmes in Bunker cave (Germany) and Hollow Ridge cave (Florida, USA) (Tremaine et al., 2011; Riechelmann et al., 2013). Interestingly, kinetic effects of an identical magnitude were measured in cave sites of different fluid path, drip rate, and calcite saturation index, at different times. This raises interesting questions about the usage of the replication test to identify isotopic equilibrium in ancient speleothems and whether an identical magnitude of the kinetic isotope effects is climate-driven or a cave-specific effect.

Due to the complex nature of cave systems and the difficulty of isolating different physicochemical factors contributing to the formation of speleothems, theoretical modelling (Mühlinghaus et al., 2007; Dreybrodt, 2008; Mühlinghaus et al., 2009; Scholz et al., 2009; Dreybrodt and Scholz, 2011; Deininger et al., 2012; Dreybrodt and Deininger, 2014) and experimental simulation (Wiedner et al., 2008; Polag et al., 2010; Day and Henderson, 2011; Hansen et al., 2013; Dreybrodt et al., 2016) have long been carried out in order to better understand equilibrium and kinetic isotope effects in cave environments. In theoretical models, two general approaches have been employed to explain the evolution of $\delta^{13}\text{C}$ and $\delta^{18}\text{O}$ in drip water and consequently in growing carbonates (for review see Dreybrodt and Scholz, 2011): (1) the classic Rayleigh distillation approach (e.g., Scholz et al., 2009) and (2) the kinetic fractionation approach where different rate constants of calcite precipitation are used for the light and heavy isotopes by introducing an unknown parameter (i.e., γ ; Dreybrodt, 2008). Both

approaches conclude the time-dependence of $\delta^{13}\text{C}_{\text{Cc}}$ and $\delta^{18}\text{O}_{\text{Cc}}$ values under a constant temperature, showing an enrichment trend in ^{13}C and ^{18}O with the elapsed time of carbonate precipitation. Scholz et al. (2009) compared the two approaches using a hypothetical γ value of 1. They showed that the predicted trends of the two approaches are in excellent agreement with each other when up to 75% of the total DIC available in drip water for carbonate precipitation is consumed. However, a significant divergence between the two approaches is estimated during the remaining stage of carbonate precipitation. This implies that the two approaches might be valid when the drip rate of cave drip water is fast (i.e., fast rates correspond to $\leq 75\%$ of the time required for potential carbonate precipitation; Hansen et al., 2013), but at least one of the approaches is either overestimated or underestimated at very slow drip rates. Therefore, experiment studies are needed to validate the two aforementioned theoretical approaches.

Several experimental studies have been performed to simulate the formation of speleothems in a controlled laboratory setting by mostly using the following two types of experimental designs: (1) the channel design (Fantidis and Ehhalt, 1970; Wiedner et al., 2008; Polag et al., 2010; Hansen et al., 2013) and (2) the direct drip design (Day and Henderson, 2011). In the channel design, a CaCO_3 saturated solution was allowed to flow upon a fiber glass or marble channel, precipitating calcite either by mixing CaCl_2 and NaHCO_3 solutions (Fantidis and Ehhalt, 1970; Wiedner et al., 2008; Polag et al., 2010) or CO_2 degassing (Hansen et al., 2013). The solution mixing experiments were the first to report non-equilibrium carbon and oxygen isotope effects in synthetic calcite formed under cave analogues conditions (Wiedner et al., 2008; Polag et al., 2010). However,

these mixing experiments did not account for the potential effects of two in-cave processes on the $\delta^{13}\text{C}$ and $\delta^{18}\text{O}$ values of drip water and, consequently, on those for growing carbonate minerals. The main in-cave processes are the initial CO_2 degassing and CO_2 exchange, which are caused by the $p\text{CO}_2$ gradient between drip water and the ambient cave atmosphere (Polag et al., 2010). Hansen et al. (2013) used the channel design to experimentally determine the time constants for CO_2 degassing, $p\text{CO}_2$ equilibration to cave atmosphere and carbonate precipitation in a thin water film. Their results provide time constraints on the interpretation of stable isotope signals in speleothems.

Meanwhile, Day and Henderson (2011) performed a set of laboratory experiments that closely simulated the formation of natural stalagmites using the direct drip design. In their experiments, carbonate precipitation was induced by CO_2 degassing from a thin water film, which was maintained by direct dripping of a CaCO_3 saturated solution from a height of 30 cm. They reported the temperature-dependence of the stalagmite growth rate with a complicated contribution from the drip rate effect. However, this observation might be influenced by the significant washing effect induced by their reported fast drip rates, which were not slow enough to allow time for CaCO_3 precipitation under certain conditions (Dreybrodt, 2012). Second, the authors measured an ^{18}O enrichment in the synthetic stalagmites at high temperature when the drip rate was slow. Although the general trend of the latter observation is significant, it is unclear whether the magnitude of this isotopic enrichment is caused by the drip rate effect and/or evaporation (i.e., the loss of control on the relative humidity in their experimental setup). Finally, they did not

report carbon isotope compositions in their study due to a failure in maintaining consistent carbon isotopic composition in the initial solutions.

In this paper, we simulated the growth of speleothems under tightly controlled conditions (e.g., temperature, relative humidity, solution chemistry, and drip rate) in an artificial cave to investigate the controlling factors on the growth rate of speleothems, and characterize the systematics of carbon and oxygen isotopes in cave environments. Our results elucidate equilibrium and non-equilibrium isotope effects in cave carbonates and their formation mechanisms.

2.3 Experimental and analytical Methods

2.3.1 Experimental Setup

In an attempt to efficiently mimic the growth of speleothems in natural caves, our experiments were conducted in a plant growth chamber (Model: Conviron CMP4030). The growth chamber has a central control system which controls and monitors several environmental parameters, such as temperature ($\pm 0.1^{\circ}\text{C}$), relative humidity ($\pm 1\%$) and $p\text{CO}_2$ (± 10 ppmv). The control system is equipped with a data logger that records the environmental parameters every half second. In this study, the experimental temperature was maintained at 15, 25 and 32 $^{\circ}\text{C}$. The relative humidity of the growth chamber was maintained at 95 % by its humidifier that is connected to our in-house reverse osmosis system. The $p\text{CO}_2$ in the growth chamber was passively equilibrated to the $p\text{CO}_2$ level in the laboratory atmosphere (550 ppmv) through a small opening in the growth chamber body. This is to avoid sudden drops in the $p\text{CO}_2$ level in the growth chamber because the

replacement of the $\text{CaCO}_3\text{-CO}_2\text{-H}_2\text{O}$ solution requires the opening of the chamber to the laboratory atmosphere during the experiments. The dimensions of this chamber are 1.34 m \times 1.34 m \times 1.48 m, providing sufficient space to mimic the drip height in natural caves. Moreover, the chamber has room to accommodate three experimental setups (namely, FFR, IFR and SFR) shown in Figure 2.1. The name of each setup is the abbreviation of the speed of its flow rate. Each individual experimental setup is comprised of five components listed below to simulate drip water flow and carbonate precipitation in natural cave settings.

1) **1000 mL Pyrex[®] glass bottle** served as a closed system reservoir for the starting solution. The smaller volume of the bottle minimizes the boundary layer between the $\text{CaCO}_3\text{-CO}_2\text{-H}_2\text{O}$ solution and the head space. This approach reduces CO_2 degassing, facilitating the maintenance of initial $p\text{CO}_2$ and carbon isotope composition of DIC in the solution during the experiments. Moreover, the level of the solution in the bottle was maintained above 4 cm from the bottom to avoid significant CO_2 degassing and CaCO_3 precipitation within the bottle.

2) **A peristaltic pump** supplied the $\text{CaCO}_3\text{-CO}_2\text{-H}_2\text{O}$ solution through Tygon[®] tubing from the 1000 mL glass bottle to the point at which the solution is exposed to the atmosphere of the growth chamber. The pumps in the FFR, IFR and SFR setups were calibrated to Fast, Intermediate and Slow Flow Rates which are 700, 270 and 125 mL/d, respectively.

3) **A Pyrex glass channel tube of a 35 cm length and 2.5 cm diameter (OD):** the inside of the glass tube is etched (HF acid) to form a longitudinal path of 0.9 cm width.

This path disturbed the surface tension of the glass and induced a flow of an average thin water film (0.011 ± 0.002 cm) between the end of the Tygon® tubing which is connected to a plastic tip, and the drip point (Fig. 2.1). This tube is used to simulate the drip water flow on a stalactite surface, facilitating CO₂ degassing, *p*CO₂ equilibration to the cave atmosphere and prior carbonate precipitation (PCP; which occurs in some cases) before the drop impinges the stalagmite surface in natural caves. The combination between the pumping rate and the angle of the glass tube resulted in a constant drop volume (0.16 mL) and three different drip intervals of 20, 50, 110 seconds for FFR, IFR and SFR pumps, respectively. The drip interval is defined by the time between two sequential drops from the end of the channel tube or the residence time of a drop on the apex of a stalagmite (equivalent to component # 4 in this setup). In addition to the drip interval time, extra time is required when each drop of the CaCO₃-CO₂-H₂O solution flows through the channel tube. This extra time was estimated by injecting a dye (equal to the drop volume) at the beginning of the channel tube and by measuring the time required for the dye to leave the channel tube. This “residence time of a drop” in the channel tube in the FFR, IFR, and SFR setups are 50 ± 2 , 100 ± 5 , and 220 ± 10 seconds, respectively.

4) A upper (convex) watch glass of a 10 cm diameter was placed 85 cm underneath the dripping end of the channel tube. The convex surface of the watch glasses was smoothly scratched in two directions to break the tension force of the glass and therefore to mimic the morphology of natural stalagmite surface. When the drop impinges the watch glass, it forms a circular area of 5 cm diameter, creating a water thin film of ~ 0.008 cm (as estimated from the drop volume of 0.16 mL / area of 19.63 cm^2). Each drop

stays on the formed circular area until it is replaced by a new drop (equivalent to drip interval time). Therefore, the exposure time of any drop to the cave atmosphere upon the drop leaves the circular area is the sum of the residence time of the drop in the channel tube and the drip interval time. As a result, the exposure time in the FFR, IFR and SFR setups are 70 ± 2 , 150 ± 5 , and 330 ± 10 seconds.

5) A *lower (concave) watch glass of a 20 cm diameter* is located below the upper watch glass to receive the surplus drip water. This concave watch glass has a volume of 370 mL which requires 12.9, 34.8 and 78.6 hours to be filled (i.e., residence time = flow rate / volume; taking evaporation into account) under fast, intermediate and slow flow rate conditions, respectively. The solution thickness at the center of the watch glass is 1.5 cm when it is full. These lower watch glasses can be used to simulate the carbonate precipitation in a pool setting in natural caves.

2.3.2 Preparation of solutions

Our starting $\text{CaCO}_3\text{-CO}_2\text{-H}_2\text{O}$ solutions were prepared by completely dissolving 2 mmol of CaCO_3 (Fisher chemicals; ACS-grade.) into 1 L of 18 M Ω deionized water stored in a Pyrex glass bottle. The deionized water is taken from an isotopically homogeneous water reservoir of a 27 L volume to maintain an identical starting $\delta^{18}\text{O}$ value over the course of each experiment. The complete dissolution of CaCO_3 was achieved by magnetically stirring, and bubbling CO_2 into, the starting solution at the room temperature until the solution became clear and no CaCO_3 salts were observed at the bottom of the glass bottle. Subsequently, the pH of the starting $\text{CaCO}_3\text{-CO}_2\text{-H}_2\text{O}$

solution was adjusted to ~ 7 by slowly seeping N_2 gas through the $CaCO_3$ - CO_2 - H_2O solutions for a few minutes. Visual $CaCO_3$ precipitation was not observed during the pH adjustment. The pH-adjusted starting solutions were then tightly sealed and stored at either 15, 25 or 32 °C, depending on the target experimental temperature, from 1 to 3 days until the thermal and isotopic equilibria were established (Beck et al., 2005; Kim et al., 2006).

Prior to uploading the starting solution for the speleothem synthesis experiment, each solution was sampled into a 5 mL vial to determine initial pH, $\delta^{18}O_{H_2O}$, $\delta^{13}C_{DIC}$ and DIC concentration. These glass vials were stored at 4 °C immediately for the aforementioned chemical and isotopic analyses. The remainder of each starting solution in the glass bottle (i.e., starting solution depth ≥ 4 cm) was used for its pH, isotopic compositions, and DIC concentration to estimate the average of the initial $\delta^{18}O$, $\delta^{13}C$ and DIC values. In addition, the same analyses were conducted for the final solution from the lower watch glasses.

2.3.3 Stable isotope and other analyses

Stable isotope compositions, as well as DIC concentrations, were measured using the Gas Bench II system coupled with a Thermo Finnigan Delta plus XP continuous flow isotope ratio mass spectrometer (CF-IRMS) at McMaster University. Oxygen isotope composition of water ($\delta^{18}O_{water}$) was determined using a modified CO_2 - H_2O equilibration technique (Gebbinck et al., 2014). Briefly, the Exetainer® vials were flushed and filled with a 0.2 % CO_2 and 99.8 % He mixture. Subsequently, a 0.2 mL aliquot of the water

sample was injected using a 1 mL syringe and then was equilibrated with CO₂ for a minimum of 27 h at 25 ± 0.1 °C. Finally, the oxygen isotope composition of the water-equilibrated CO₂ was determined using the Gas Bench II-CF-IRMS. Reported δ¹⁸O values were normalized to two internal laboratory water standards (MRSI-1 and MRSI-2) previously calibrated against V-SMOW and SLAP. Long-term internal precision of these water standards is better than 0.08 ‰. The oxygen isotope compositions were reported on the V-SMOW scale. For carbon isotope compositions of DIC and its concentrations in solution samples, the Exetainer® vials were preloaded with 0.2 mL 100% H₃PO₄, capped with a new septum and then flushed with 99.999% He. The flushed vial was then injected with 0.2 mL of the solution samples using a 1 mL syringe. The H₃PO₄ reacted with DIC in the solution samples to produce CO₂ for a minimum of 24 h at 25 ± 0.1 °C, followed by the isotopic analysis by the Gas Bench II-CF-IRMS. The solution samples were measured against three isotopic reference materials (i.e., LSVEC, NBS 18, and NBS 19) and two in-house DIC standards (i.e., 2 mmol/L NaHCO₃ and 5 mmol/L NaHCO₃) for the normalization of the carbon isotope composition and the DIC concentration, respectively. Measured δ¹³C_{VPDB} values of the reference materials are reproducible within ± 0.1 ‰ (1σ). The range of DIC concentrations in the sodium bicarbonate standard solutions allowed calibration of mass 44 peak area as a measure of DIC concentration with a precision (1σ) of ≤ 2.5 %. The pH of the starting and final solutions was measured with an Oakton® combination pH electrode calibrated against three NIST-traceable buffers (i.e., 4, 7, and 10 at 25 °C).

Multiple aliquots of cave air were collected in 100 mL flasks (dual-inlet flask). CO₂ was extracted from these aliquots and purified using a customized vacuum line. Purified CO₂ was collected in evacuated septum-capped Exetainer®. Subsequently, CO₂ was transferred via gas syringe to a separate He-flushed, septum-capped Exetainer®, followed by the isotopic analysis by the Gas Bench II-CF-IRMS. CO₂ gases were measured against two isotopic reference materials (LSVEC, NBS 18) and their carbon isotope compositions reported in standard δ notation on the VPDB scale with analytical uncertainty of ± 0.1 ‰.

The synthetic speleothem carbonates were analyzed at 90 °C for their $\delta^{13}\text{C}$ and $\delta^{18}\text{O}$ values using an OPTIMA gas source stable isotope ratio mass spectrometer interfaced with an automated carbonate device. Reported $\delta^{13}\text{C}$ and $\delta^{18}\text{O}$ values were normalized to the recommended values for three isotopic reference materials LSVEC, NBS 18 and NBS 19 (Kim et al., 2015). Long-term internal precision of these reference materials is better than 0.08 ‰ for both $\delta^{13}\text{C}$ and $\delta^{18}\text{O}$. Carbon and oxygen isotope compositions of the synthetic speleothems are reported in standard δ notation on the VPDB and VSMOW scale, respectively.

The weight of the carbonate precipitate on the upper watch glass was quantified by weighting the watch glass before and after the synthesis experiment. Upon the completion of the synthesis experiment, the upper watch glass was rinsed with deionized water and then left to dry in a fume hood overnight. Subsequently, the final weight of the upper watch glass was determined. The mineralogy and crystallography of the carbonate precipitates from both the upper and the lower watch glasses was examined using the X-ray diffraction (XRD) and binocular microscope.

2.4 Results

2.4.1 Mineralogy and weight of CaCO_3 precipitates

Microscopic investigation of the carbonate precipitates on the upper and lower watch glasses clearly showed calcite rhombs. Samples from each experimental condition were randomly selected for the XRD analysis. The XRD results confirmed that the majority of the carbonate precipitates ($\geq 93.6\%$) formed on our upper and lower watch glasses are calcite with a minor amount of vaterite and aragonite ($\leq 6.4\%$; Supplementary Table S1).

CaCO_3 yields on the upper watch glasses show a linear relationship between the rate of growth (mg/d) and both temperature and DIC flow rate (Fig. 2.2, Table 2.1). The DIC flow rate (mmol/d) is expressed as multiplication of the flow rate (mL/d) by the DIC concentration (mmol/mL) in the starting $\text{CaCO}_3\text{-CO}_2\text{-H}_2\text{O}$ solution. The DIC flow rate (mmol/d) dependences of the CaCO_3 growth rate (mg/d) were 1.05 mg/mmol, 6.24 mg/mmol and 11.41 mg/mmol at 15, 25 and 32 °C, respectively (Fig. 2.2a). Moreover, we observed a significant effect of temperature on the CaCO_3 growth rate (i.e., 0.06 mg.d⁻¹/°C, 0.36 mg.d⁻¹/°C and 1.43 mg.d⁻¹/°C) at constant DIC flow rates of 0.5 mmol/d, 1.08 mmol/d and 2.8 mmol/L, respectively (Fig. 2.2b).

2.4.2 DIC concentration, pH and isotopic compositions of drip water and cave CO_2

The DIC concentration, pH, oxygen and carbon isotope compositions of our experimental solutions are listed in Table 2.2. Final DIC concentration, pH and isotopic compositions in the lower watch glasses are plotted against residence time in the figures

2.3, 2.4, 2.5, 2.7, 2.8, and 2.10. Longer residence time obviously corresponds to slower flow rate.

The mean DIC concentration of our starting solutions was 4.06 ± 0.13 (1σ) mmol/L. However, final DIC concentrations in the lower watch glass drop exponentially with decreasing the flow rate while the depletion rate of the relative DIC concentration increases with increasing temperature (Fig. 2.3a). The final pH of drip water in the lower watch glasses is statistically indistinguishable within each experimental temperature (Fig. 2.3b). However, a measurable difference in pH was observed between the similar final pH at high temperatures (25 °C and 32 °C) and those at low temperature (15 °C).

The carbon isotope compositions of the starting DIC ($\delta^{13}\text{C}_{\text{DICin}}$) in our experiments were within a narrow range between -32.4 ± 0.5 ‰ and -35.2 ± 0.5 ‰. In contrast, there are large positive shifts ($\delta^{13}\text{C}_{\text{DICfn}} - \delta^{13}\text{C}_{\text{DICin}}$) in the carbon isotope composition of the final drip water ($\delta^{13}\text{C}_{\text{DICfn}}$) in the lower watch glass from the $\delta^{13}\text{C}_{\text{DICin}}$ values (Fig. 2.4). These positive shifts vary in magnitude based upon the residence time (or the flow rate) and temperature with a minimum magnitude of 5.4 ± 0.4 ‰ ($n = 3$) under the fast flow rate at 15 °C and a maximum magnitude of 25.6 ± 0.7 ‰ ($n = 3$) under the slow flow rate at 32 °C. The average of $\delta^{13}\text{C}$ in cave CO_2 was -13 ± 0.5 ‰ ($n = 10$).

Under all conditions tested in this study, the oxygen isotope composition of the starting solution ($\delta^{18}\text{O}_{\text{H}_2\text{Oin}}$) has a mean of -7.68 ± 0.08 ‰. However, subtle increases in the oxygen isotope composition of the final drip water ($\delta^{18}\text{O}_{\text{H}_2\text{Ofn}}$) were measured in the lower watch glasses, relative to those observed in $\delta^{13}\text{C}_{\text{DICfn}}$ (Fig. 2.5). These subtle increases ($\delta^{18}\text{O}_{\text{H}_2\text{Ofn}} - \delta^{18}\text{O}_{\text{H}_2\text{Oin}}$) show sensitivity to both flow rate and the temperature in

our experimental setup. A minimum $\delta^{18}\text{O}_{\text{H}_2\text{Ofn}} - \delta^{18}\text{O}_{\text{H}_2\text{Oin}}$ of $0.48 \pm 0.16 \text{ ‰}$ ($n = 3$) was observed under fast flow rate at 15 °C whereas the maximum of $1.54 \pm 0.05 \text{ ‰}$ ($n = 3$) in $\delta^{18}\text{O}_{\text{H}_2\text{Ofn}} - \delta^{18}\text{O}_{\text{H}_2\text{Oin}}$ was determined under slow flow rate at 32 °C (Fig. 2.5).

2.4.3 Carbon and oxygen isotope compositions in the precipitated calcite

Carbon and oxygen isotope compositions of precipitated calcite were measured at the apex of the upper watch glasses (i.e., 0 to 2 cm from its centre) and in the bottom of the Lower watch glasses (0 to 5 cm from its centre) and are listed in Table 2.3.

2.4.3.1 Carbon and oxygen isotope compositions of calcite precipitated on the upper watch glasses (stalagmite-like settings)

In our experiments, the upper watch glasses simulate the surface morphology of stalagmites in natural caves. Therefore, the thin film of the calcite precipitated on the upper watch glasses is an analogue to the thin carbonate layer at the apex of stalagmites (e.g., Riechelmann et al., 2013). Consequently, our tightly controlled laboratory experiments allowed us to investigate carbon and oxygen isotope fractionations between calcite and drip water in natural caves by eliminating temperature fluctuation, drip rate instability that are typically occurred in cave environments.

In general, there is a strong increase in the carbon isotope fractionation between the calcite and the DIC in the initial solution ($\delta^{13}\text{C}_{\text{Cc}} - \delta^{13}\text{C}_{\text{DICin}}$) as the temperature and the drip water exposure time to the cave atmosphere increase (Fig. 2.6a). The minimum $\delta^{13}\text{C}_{\text{Cc}} - \delta^{13}\text{C}_{\text{DICin}}$ has a mean of $3.1 \pm 0.2 \text{ ‰}$ ($n = 3$) which is measured at the fast flow rate and 15 °C . Conversely, a maximum $\delta^{13}\text{C}_{\text{Cc}} - \delta^{13}\text{C}_{\text{DICin}}$ value of $13.8 \pm 0.3 \text{ ‰}$ ($n = 3$)

was observed at the slow flow rate and 32 °C. In contrast, the oxygen isotope fractionation between calcite and water ($1000\ln^{18}\alpha_{\text{Cc-H}_2\text{O}}$) decreases as the temperature increases in agreement with the theory of Urey (1948) and other experimental and empirical studies (e.g., Kim and O’Neil, 1997; Coplen, 2007; Day and Henderson, 2011; Tremaine et al., 2011; Fig. 2.6b). Moreover, $1000\ln^{18}\alpha_{\text{Cc-H}_2\text{O}}$ also gradually decreases with increasing flow rate at a given temperature (Fig. 2.6b).

2.4.3.2 Carbon and oxygen isotope compositions of calcite precipitated on the lower watch glasses (pool-like settings)

The lower watch glasses in our experiments mimic a pool setting in natural caves. The carbonate formed in the lower watch glass represents a later stage of CaCO_3 precipitation after the initial CaCO_3 deposition on the upper watch glass. In other words, the carbonate on the lower watch glass grew from a more chemically depleted DIC reservoir than the one in the upper glass. The $\delta^{13}\text{C}_{\text{Cc}}$ value of the calcite formed on the lower watch glass is higher than that from the upper watch glass, resulting in a larger $\delta^{13}\text{C}_{\text{Cc}} - \delta^{13}\text{C}_{\text{DICin}}$ value (Fig. 2.7). In the lower watch glass, the lowest $\delta^{13}\text{C}_{\text{Cc}} - \delta^{13}\text{C}_{\text{DICin}}$ value of 9.3 ± 1.2 ‰ (mean $\pm 1\sigma$; n=3) was observed under the fast flow rate at 15 °C. The calcite formed under the slow flow rate at 32 °C showed the highest $\delta^{13}\text{C}_{\text{Cc}} - \delta^{13}\text{C}_{\text{DICin}}$ value (27.5 ± 0.4 ‰; n = 3). These large $\delta^{13}\text{C}_{\text{Cc}} - \delta^{13}\text{C}_{\text{DICin}}$ values are in parallel with the large positive shifts measured between the initial and final DIC ($\delta^{13}\text{C}_{\text{DICfn}} - \delta^{13}\text{C}_{\text{DICin}}$; Fig. 2.7).

In contrast to the carbon isotope patterns observed between the upper and the lower watch glasses, $\delta^{18}\text{O}_{\text{Cc}}$ values of the calcite precipitates from the lower watch glass are

lower than those of the calcites formed on the upper watch glass with exception to the calcite formed at 15 °C (Fig. 2.8). The difference between $\delta^{18}\text{O}_{\text{Cc}}$ of the lower and the upper watch glasses ($\delta^{18}\text{O}_{\text{Cc.L}} - \delta^{18}\text{O}_{\text{Cc.U}}$) mainly decreases with residence time (slow flow rate) while $\delta^{18}\text{O}_{\text{H}_2\text{O}_{\text{fm}}}$ in the lower watch glasses increases (Fig. 2.8).

2.5 Discussion

2.5.1 Temperature and flow rate effects on stalagmite growth rate

In our setup, the convex nature of the upper watch glass mimics the morphology of stalagmite's surface in natural caves. In all experiments, these upper watch glasses have identical curvature and size (i.e., similar area), enabling direct comparison of the measured growth rate (mg/d) representative of stalagmite growth rate (mg/cm²/d) among all experiments. Our results show positive linear correlations between the daily growth rate and DIC flow rate as well as temperature (Fig. 2.2a,b). The slope of the linear correlation between daily growth rate and DIC flow rate varies as a function of temperature, with an eleven-fold increase between 15 °C and 32 °C. Similarly, the linear slope between daily growth mass and temperature at high DIC flow rate (2.8 mmol/d) is approximately 24 times steeper than that at low DIC flow rate (0.5 mmol/d). In summary, the influence of the DIC flow rate on the growth mass becomes more significant at high temperatures whereas the effect of temperature on the growth mass is strong at high DIC flow rates (Fig. 2.9).

The observed linear trends among the growth rate, DIC flow rate and temperature are in agreement with theoretical, experimental and empirical studies (Franke, 1965;

Buhmann and Dreybrodt, 1985; Genty and Quinif, 1996; Baker et al., 1998). The temperature control on the growth rate is explained by the temperature dependence of the $\text{H}^+ + \text{HCO}_3^- \rightarrow \text{CO}_2 + \text{H}_2\text{O}$ reaction kinetics. The weaker temperature dependence of the growth rate at low DIC flow rate in our data might be a result of progressive prior carbonate precipitation (PCP) in the Pyrex channel (at higher temperatures) before the drip water arrived the upper watch glass (Fig. 2.2a). The PCP decreased the saturation state of drip water, and the precipitation rate. In addition, the flow rate also substantially affects the growth rate by controlling the amount of DIC available on the growth surface (Genty and Quinif, 1996; Banner et al., 2007). Nevertheless, the DIC flow rate effect at high temperatures can be masked under a very fast drip rate (washing effect) which allows neither the complete CO_2 degassing of the drip water nor the initiation of CaCO_3 precipitation (see Figs. 5, 6 in Day and Henderson, 2011).

Given that the pCO_2 of cave atmosphere (550 ppm) and DIC (4 mmol/L) concentration of drip water in this study are common in natural cave settings (e.g., Bar-Matthews et al., 1996; Baker et al., 1998; Banner et al., 2007; Casteel and Banner, 2015), the observed growth mass patterns (Fig. 2.9) enable understanding of stalagmite growth rate in natural caves. Figure 2.9 shows that stalagmites grown in high temperature caves should display a wider range in growth rates than those formed in cold caves. This wide range is caused by the high sensitivity of the growth rates to DIC flow rate (rainfall amount) at high temperatures. In contrast, the narrow range of slow growth rates in stalagmites formed in cold temperature caves can be attributed to the weak sensitivity of growth rate to DIC flow rate at low temperatures. Stalagmite growth rates in temperate

caves have the potential to respond to variations in temperature and/or DIC flow rate. However, other non-climate factors, including the hydrological path, depth of cave under surface and cave ventilation, might complicate regional and within-cave comparison of the stalagmites' growth rate.

2.5.2 *Chemical and isotopic evolution of drip water*

In order to study chemical and isotopic evolution in drip water in our experiments, we compared final pH, DIC concentration, $\delta^{18}\text{O}_{\text{H}_2\text{O}}$ and $\delta^{13}\text{C}_{\text{DIC}}$ (i.e., end members) in the lower watch glasses to those measured at the starting of the experiments under different temperature and flow rate conditions.

2.5.2.1 *Chemical evolution in drip water*

In all experiments, DIC concentration exponentially decreased toward the equilibrium DIC concentration with respect to cave $p\text{CO}_2$ (Fig. 2.3a). The rate of this depletion decreases with increasing flow rate, but increases with temperature. When drip water is exposed to the cave atmosphere, the $p\text{CO}_2$ gradient between the cave atmosphere (550 ppmv) and the drip water (14000 to 18000 ppmv) drives initial degassing of CO_2 from the drip water and thereby lowers the DIC concentration by a small portion, approximately equivalent to 95% of CO_2 (aq) in the drip water (Dreybrodt and Scholz, 2011; Hansen et al., 2013). Initial CO_2 degassing does not lead to calcite precipitation. Eventually the pH rises to a stable value of 8 ± 0.1 that is time- and temperature-independent, indicating the dominance of the bicarbonate ion in the drip water (Fig. 2.3b). The slightly higher pH values at high temperature experiments may be due to the high

solubility of CO_2 (g) at low temperature. As the pH rises, the calcite saturation state of the drip water is driven from undersaturation (< 0 in this study) to saturation, allowing CaCO_3 precipitation to start. Progressive CaCO_3 precipitation and its synchronous CO_2 degassing gradually deplete the DIC reservoir and calcium concentration as time elapsed. Moreover, temperature exhibits proportional control on the DIC depletion because the CaCO_3 precipitation and outgassing increases with temperatures and vice versa. Other factors (e.g., solution thickness in the lower watch glass) can place additional constraints on the DIC depletion (Buhmann and Dreybrodt, 1985; Hansen et al., 2013); however, this was avoided in our experiments by using lower watch glasses of identical dimensions in all experimental trials.

Figure 2.3a demonstrates that chemical equilibrium between the DIC of the residence water in lower watch glasses and cave atmosphere has not been attained under our experimental conditions except for intermediate and slow flow rates at 32 °C; despite the apparent stability of drip water pH.

2.5.2.2 Carbon isotope evolution in drip water

The carbon isotope composition of the final drip water ($\delta^{13}\text{C}_{\text{DICfn}}$) increases from the starting drip water ($\delta^{13}\text{C}_{\text{DICin}}$) with increasing residence time and temperature in the lower watch glasses (Fig. 2.4). This increase likely results from one or a combination of the following two processes: 1) Degassing of isotopically light CO_2 caused by the $p\text{CO}_2$ gradient between drip water and cave atmosphere, and progressive CaCO_3 precipitation (Frisia et al., 2011); and 2) CO_2 exchange between the DIC in drip water and cave

atmosphere (Dreybrodt et al., 2016). The effect of the first process on $\delta^{13}\text{C}_{\text{DIC}}$ in drip water can be estimated either by the classical Rayleigh distillation model (e.g., Mickler et al., 2004; Mickler et al., 2006; Mühlinghaus et al., 2009) or the kinetic fractionation model (Dreybrodt, 2008) based upon the initial and final DIC concentrations measured in this study. However, the Rayleigh model is preferred because its relevant parameters (i.e. equilibrium fractionation factors between the DIC and both CO_2 (g) and CaCO_3) are experimentally defined whereas the kinetic fractionation model includes an unknown parameter (i.e., γ) which has not yet been defined experimentally.

Therefore, we calculated the results based upon the Rayleigh distillation model using $\text{CO}_2\text{--HCO}_3^-$ and $\text{CaCO}_3\text{--HCO}_3^-$ fractionation factors from Mook, 2000 and Romanek et al., 1992, respectively (Fig. 2.4). If the first process has solely affected the $\delta^{13}\text{C}_{\text{DIC}}$ in drip water, then the measured $\delta^{13}\text{C}_{\text{DICfn}} - \delta^{13}\text{C}_{\text{DICin}}$ should be in agreement with the Rayleigh distillation model. However, the measured $\delta^{13}\text{C}_{\text{DICfn}} - \delta^{13}\text{C}_{\text{DICin}}$ values are larger than those predicted by Rayleigh distillation model as can be seen in Figure 2.4. The large differences between the measured and calculated $\delta^{13}\text{C}_{\text{DICfn}} - \delta^{13}\text{C}_{\text{DICin}}$ cannot be explained by the discrepancy among the used and other published carbon isotope fractionation factors (Deines et al., 1974; Mook, 2000) employed in the Rayleigh distillation model. Notably, using Dreybrodt (2008)'s kinetic model with high hypothetical values of γ (≥ 1.01) cannot account for the difference between the measured $\delta^{13}\text{C}_{\text{DICfn}} - \delta^{13}\text{C}_{\text{DICin}}$ and those predicted from Rayleigh distillation model. These significant differences increase with increasing the residence time (slow flow rate) and temperature in the lower watch glasses, suggesting substantial influence of continuous

CO₂ exchange between the DIC in drip water and cave atmosphere on the $\delta^{13}\text{C}_{\text{DICfn}}$ (Dreybrodt and Scholz, 2011; Dreybrodt et al., 2016). Indeed, the major carbon reservoir in our experimental setup is the atmospheric CO₂ in the growth chamber (> 93 % of the total carbon in the system). Thus, the $\delta^{13}\text{C}_{\text{DICfn}}$ should increase to a value that would be in equilibrium with the -13 ‰ carbon isotope composition of cave atmospheric CO₂ resulting in average $\delta^{13}\text{C}_{\text{DICfn}} - \delta^{13}\text{C}_{\text{DICin}}$ value of 28.9 ± 0.5 ‰ at all temperatures (Mook, 2000). However, Figure 2.4 shows that the $\delta^{13}\text{C}_{\text{DICfn}}$ did not reach the carbon isotope equilibrium with respect to the atmospheric CO₂. This is most likely due to the continuous flow of the drip water – containing DIC of lower $\delta^{13}\text{C}$, close to the $\delta^{13}\text{C}_{\text{DICin}}$, over the lower watch glasses.

We evaluated the CO₂ exchange effect by subtracting the measured $\delta^{13}\text{C}_{\text{DICfn}}$ from the predicted $\delta^{13}\text{C}_{\text{DICfn}}$. As a result, the CO₂ exchange appears to increase the $\delta^{13}\text{C}_{\text{DICfn}}$ by 3.9 ‰ and 22 ‰ between fast flow rate at 15°C and slow flow rate at 32°C, respectively. Carbon isotope exchange between DIC (NaHCO₃) and surrounding atmospheric CO₂ has been experimentally reported by Dreybrodt et al. (2016); however calcite precipitation was excluded in their experiments. Our study is the first to report the evolution in $\delta^{13}\text{C}_{\text{DIC}}$ under coherent CO₂ exchange and calcite precipitation, which is critical to understanding the effect of CO₂ exchange on the $\delta^{13}\text{C}_{\text{Cc}}$ in speleothems. Nevertheless, the large isotopic effects of CO₂ exchange on the $\delta^{13}\text{C}_{\text{DICfn}}$ of drip water in our experiment present an exaggerated picture of those might occur in pool settings in well-ventilated caves (e.g., Matthey et al., 2010) because of the low $\delta^{13}\text{C}_{\text{DICin}}$ used in our experiments (ranges from -32.4 ± 0.5 to -35.2 ± 0.5 ‰). These $\delta^{13}\text{C}_{\text{DICin}}$ values are lower than those in natural caves

but they are preferred experimentally to distinguish between the simultaneous effects of the CO₂ exchange and the CO₂ degassing on the $\delta^{13}\text{C}_{\text{Cc}}$.

2.5.2.3 Oxygen isotope evolution in drip water

The oxygen isotope composition of the final drip water ($\delta^{18}\text{O}_{\text{H}_2\text{Ofn}}$) shows a similar behaviour to that observed in carbon isotopes (Fig. 2.5). Drip water contains two oxygen reservoirs: water and the much smaller reservoir of DIC. These two reservoirs are in continuous isotopic exchange with each other (Beck et al., 2005). As a result, any process that alters $\delta^{18}\text{O}$ of one reservoir will affect the other. However, even a large shift in $\delta^{18}\text{O}_{\text{DIC}}$ will result in a minimal change in the $\delta^{18}\text{O}_{\text{H}_2\text{O}}$ value of water reservoir. For instance, decrease in DIC concentration due to fast CO₂ degassing and subsequent CaCO₃ precipitation enriches ¹⁸O in the DIC pool but will hardly affect $\delta^{18}\text{O}_{\text{H}_2\text{O}}$. In contrast, water evaporation can increase $\delta^{18}\text{O}_{\text{H}_2\text{O}}$ and thus $\delta^{18}\text{O}_{\text{DIC}}$.

In our experiments, the relative humidity was maintained at 95 % to minimize evaporation of drip water. The resultant deficiency in the air moisture content (5 %) can cause minimal evaporation of the residence water in the lower watch glasses, thereby increasing the $\delta^{18}\text{O}_{\text{H}_2\text{Ofn}}$. Nevertheless, the $\delta^{18}\text{O}_{\text{H}_2\text{Ofn}}$ value should rise to a steady state as the lower watch glass is under surplus discharge conditions (flow rate \gg evaporation rate) or 10 % of the water is evaporated at relative humidity of 95% (Gat and Gofiantini, 1981). Therefore, the steady state of the $\delta^{18}\text{O}_{\text{H}_2\text{Ofn}}$ is achieved after 1.5 day (maximum) in our setup. Figure 2.5 shows an increase in $\delta^{18}\text{O}_{\text{H}_2\text{Ofn}} - \delta^{18}\text{O}_{\text{H}_2\text{Oin}}$ with either a decrease in flow rate at a constant temperature, or an increasing in temperature under a constant flow

rate. The fast flow rate minimizes the effect of evaporation on $\delta^{18}\text{O}_{\text{H}_2\text{Ofn}}$ by accelerating the establishment of the steady state in the lower watch glass and eliminating the drip water evaporation. Conversely, the increase in air temperature increases the capacity of cave air to hold water, allows more drip water to evaporate, which consequently increases the $\delta^{18}\text{O}_{\text{H}_2\text{Ofn}}$. Given that the residence time of water and the maximum increase in $\delta^{18}\text{O}_{\text{H}_2\text{Ofn}}$ are determined to be ≥ 12 hours and ≤ 1.6 ‰ in the lower watch glasses under the experimental conditions tested in this study, oxygen isotope exchange between water and DIC should be complete or near completion (Beck et al., 2005). As a result, oxygen isotope signatures of DIC species would reflect the increase in $\delta^{18}\text{O}_{\text{H}_2\text{Ofn}}$ due to evaporation.

2.5.3 Equilibrium carbon and oxygen isotope fractionations during slow calcite precipitation in pool – like settings

2.5.3.1 Equilibrium carbon isotope fractionation between calcite and DIC in lower watch glasses

Equilibrium carbon isotope fractionation between calcite and DIC species occurs under certain conditions, which are: 1) infinite or continuously replenished DIC reservoir to guarantee a constant $\delta^{13}\text{C}$ value in DIC and thus in the calcite precipitation, and 2) slow calcite precipitation (Turner, 1982). Precipitation rate of carbonates in natural caves decreases with increasing the thickness of water layer (Buhmann and Dreybrodt, 1985; Baker et al., 1998; Hansen et al., 2013). At steady state (i.e., lower watch glass is full), the water layer at the centre of the watch glasses (1.5 cm thick) is 150 orders of magnitude

thicker than the thin water film on stalagmite's surface in natural caves promoting slow calcite precipitation. In addition, the continuous replenishment of DIC by the surplus flow from the upper watch glasses to the lower watch glasses may facilitate this slow calcite precipitation at carbon isotope equilibrium. However, if a large fraction of the calcite formed before the steady state was established in the lower watch glass, the calcite would be out of carbon isotope equilibrium with the DIC species (i.e., bicarbonate) at steady state. In this case, the $\delta^{13}\text{C}_{\text{DIC}}$ would be gradually increasing and consequently the $\delta^{13}\text{C}_{\text{Cc}}$ would capture this gradual increase resulting in negative carbon isotope fractionation values between calcite and final DIC ($\delta^{13}\text{C}_{\text{DICfn}}$) that is contrary to what we actually observed in this study (Fig. 2.7).

At the temperature range of 10 – 35 °C, equilibrium carbon isotope fractionation between calcite and HCO_3^- ($1000\ln^{13}\alpha_{\text{Cc-HCO}_3^-}$) has been reported to vary between 0 and 2 ‰ (Deines et al., 1974; Turner, 1982; Romanek et al., 1992; Mook, 2000). Romanek et al. (1992) suggested a temperature-independent $1000\ln^{13}\alpha_{\text{Cc-HCO}_3^-}$ value of 1.0 ± 0.2 ‰, whereas Mook, (2002) proposed a temperature dependence of the carbon isotope fractionation (i.e., $1000\ln^{13}\alpha_{\text{Cc-HCO}_3^-} = -4232/T + 15.1$). Our measured $1000\ln^{13}\alpha_{\text{Cc-DICfn}}$ values of calcite in lower watch glasses are 1.8 ± 0.6 ‰ (n = 9), 1.4 ± 0.7 ‰ (n = 11) and 1.8 ± 0.8 ‰ (n = 9) at 15 °C, 25 °C and 32 °C, respectively (Table 2.3). Therefore, the average (1.7 ± 0.7 ‰; $\pm 1\sigma$) of our experimentally determined carbon isotope fractionation factors from three temperatures supports Romanek et al. (1992)'s temperature independency of the fractionation factor, and also suggests that calcite in

lower watch glass is at or close to the isotopic equilibrium ($\text{pH} \approx 8$; Deines et al., 1974; Turner, 1982; Romanek et al., 1992).

Finally, although the calcite in the lower watch glass formed close to carbon isotope equilibrium with respect to DIC, the $\delta^{13}\text{C}_{\text{Cc}}$ values were imprinted with in-cave processes, including PCP (DIC depletion) and CO_2 exchange between the DIC and cave atmosphere, which altered the original $\delta^{13}\text{C}_{\text{DICin}}$ values (Fig. 2.7). Therefore, these in-cave processes can obscure the vegetation signal (C3 and C4 plants) in the $\delta^{13}\text{C}_{\text{Cc}}$ of speleothems (e.g., flowstones and pool carbonates) formed from long residence water in well-ventilated cave (see section 2.5.4.1 for details).

2.5.3.2 Equilibrium oxygen isotope fractionation between calcite and H_2O in lower watch glasses

Equilibrium oxygen isotope fractionation between calcite and H_2O ($1000\ln^{18}\alpha_{\text{Cc-H}_2\text{O}}$) requires that calcite precipitation must be slower than complete oxygen isotope exchange between the DIC and water reservoirs (Dreybrodt and Scholz, 2011). The latter eliminates the enrichment in the ^{18}O content of the DIC due to the degassing of isotopically light CO_2 that leads to higher $\delta^{18}\text{O}$ in calcite than that expected at oxygen isotope equilibrium with water (Kluge et al., 2014). The estimated time required for calcite precipitation from the thick water layer in the lower watch glasses is at least two times slower than that for oxygen isotope exchange between the DIC and water (Beck et al., 2005; Hansen et al., 2013). As a result, complete oxygen isotope exchange between the DIC and water is expected in the lower watch glass. However, evaporation of water in

the lower watch glasses resulted in increase in the $\delta^{18}\text{O}_{\text{H}_2\text{O}_{\text{fn}}}$ value from the $\delta^{18}\text{O}_{\text{H}_2\text{O}_{\text{in}}}$ (Fig. 2.8). This evaporation increase ($\delta^{18}\text{O}_{\text{H}_2\text{O}_{\text{fn}}} - \delta^{18}\text{O}_{\text{H}_2\text{O}_{\text{in}}}$) would transfer to the $\delta^{18}\text{O}$ of DIC species (bicarbonate) and thus imprint the $\delta^{18}\text{O}_{\text{Cc}}$ of calcite in the lower watch glasses. Carbon isotope fractionation between calcite and DIC in the lower watch glasses indicates that the majority of calcite precipitation occurred after the steady state (i.e., lower watch glass is full) (Fig. 2.7). The $\delta^{18}\text{O}_{\text{H}_2\text{O}_{\text{fn}}}$ should reach a constant value in our set up either before or at the steady state in the lower watch glasses (see section 2.5.2.3). Therefore, if both calcites on the upper and lower watch glasses were formed in oxygen isotope equilibrium with water, the $\delta^{18}\text{O}_{\text{Cc,L}}$ values of calcite formed on lower watch glasses would be higher than their corresponding $\delta^{18}\text{O}_{\text{Cc,U}}$ values on the upper watch glasses. Hence, the difference in oxygen isotope composition of calcite between the lower and upper watch glasses ($\delta^{18}\text{O}_{\text{Cc,L}} - \delta^{18}\text{O}_{\text{Cc,U}}$) should be equal to the evaporation increase in water ($\delta^{18}\text{O}_{\text{H}_2\text{O}_{\text{fn}}} - \delta^{18}\text{O}_{\text{H}_2\text{O}_{\text{in}}}$).

Figure 2.8 demonstrates that the $\delta^{18}\text{O}_{\text{Cc,L}}$ values are lower than the values of $\delta^{18}\text{O}_{\text{Cc,U}}$ at 25 and 32 °C. This implies that the calcite on the upper watch glasses was formed out of oxygen isotope equilibrium with water at these temperatures (i.e., $\delta^{18}\text{O}_{\text{Cc,U}}$ values positively deviated from those at isotope equilibrium by a magnitude higher than the ($\delta^{18}\text{O}_{\text{H}_2\text{O}_{\text{fn}}} - \delta^{18}\text{O}_{\text{H}_2\text{O}_{\text{in}}}$)) because oxygen isotope exchange between DIC and water during slow calcite precipitation in the lower watch glasses drove the calcite precipitation toward oxygen isotope equilibrium with water. In contrast, the ($\delta^{18}\text{O}_{\text{Cc,L}} - \delta^{18}\text{O}_{\text{Cc,U}}$) under the fast flow rate at 15 °C is equal to ($\delta^{18}\text{O}_{\text{H}_2\text{O}_{\text{fn}}} - \delta^{18}\text{O}_{\text{H}_2\text{O}_{\text{in}}}$) suggesting both calcites on the upper and lower watch glasses were formed close to oxygen isotope equilibrium with

water. However, the $\delta^{18}\text{O}_{\text{Cc.L}}$ values under the intermediate and slow flow rates at 15 °C are higher than their corresponding $\delta^{18}\text{O}_{\text{Cc.U}}$ values on the upper watch glasses but the $(\delta^{18}\text{O}_{\text{Cc.L}} - \delta^{18}\text{O}_{\text{Cc.U}})$ and $(\delta^{18}\text{O}_{\text{H}_2\text{O}_{\text{fn}}} - \delta^{18}\text{O}_{\text{H}_2\text{O}_{\text{in}}})$ are not equal. Given that the residence times of water in the lower watch glasses under the latter flow rates are longer than the fast flow rate, the inequality between the $(\delta^{18}\text{O}_{\text{Cc.L}} - \delta^{18}\text{O}_{\text{Cc.U}})$ and $(\delta^{18}\text{O}_{\text{H}_2\text{O}_{\text{fn}}} - \delta^{18}\text{O}_{\text{H}_2\text{O}_{\text{in}}})$ at 15 °C is most likely explained by the following two-step scenario: 1) The calcite on the upper watch glasses formed out of oxygen isotope equilibrium with water; however, the deviation of the $\delta^{18}\text{O}_{\text{Cc.U}}$ from isotope equilibrium was smaller than the $(\delta^{18}\text{O}_{\text{H}_2\text{O}_{\text{fn}}} - \delta^{18}\text{O}_{\text{H}_2\text{O}_{\text{in}}})$, and 2) subsequently the calcite in the lower watch glasses formed close to oxygen isotope equilibrium with water resulting in $\delta^{18}\text{O}_{\text{Cc.L}}$ values higher than those of $\delta^{18}\text{O}_{\text{Cc.U}}$ and $(\delta^{18}\text{O}_{\text{Cc.L}} - \delta^{18}\text{O}_{\text{Cc.U}})$ lower than $(\delta^{18}\text{O}_{\text{H}_2\text{O}_{\text{fn}}} - \delta^{18}\text{O}_{\text{H}_2\text{O}_{\text{in}}})$.

Although the $\delta^{18}\text{O}_{\text{Cc}}$ and $\delta^{18}\text{O}_{\text{H}_2\text{O}_{\text{fn}}}$ values in the lower watch glasses at different flow rates are significantly different, the $1000\ln^{18}\alpha_{\text{Cc-H}_2\text{O}_{\text{fn}}}$ values at each temperature are nearly identical indicating the formation of calcite close or at oxygen isotope equilibrium (Fig. 2.10). Consequently, a linear fit was ascribed to the measured $1000\ln^{18}\alpha_{\text{Cc-H}_2\text{O}}$ from all experiments from the lower watch glass ($n = 31$) to define the temperature dependence of the equilibrium oxygen isotope fractionation between calcite and water in a cave environment (Fig. 2.11). A least-squares fit to these measurements yields the following equation:

$$1000\ln^{18}\alpha_{\text{Cc-H}_2\text{O}} = 18.33 \pm 0.55 (10^3/T) - 33.14 \pm 1.86 \quad (2.1)$$

$$R^2 = 0.97; P < 0.0001$$

We believe that this equation represents the equilibrium $1000\ln^{18}\alpha_{\text{Cc-H}_2\text{O}}$ value in a cave environment for the following reasons: 1) the slow calcite precipitation in the lower watch glasses; 2) the observed oxygen isotope exchange effect between DIC and water at 25 °C and 32 °C; and 3) the low calcium and DIC concentrations of the drip water in our experiments, which is commonly reported in natural caves (e.g., Baker et al., 1998; Banner et al., 2007; Tremaine et al., 2011; Casteel and Banner, 2015). Furthermore, this equation supports the commonly used temperature dependence of the oxygen isotope fractionation factor between calcite and water reported by Kim and O'Neil (1997), especially when the same acid fractionation factor is used (i.e., Sharma and Clayton, 1965). In addition, Figure 2.11 shows that there is an excellent agreement among our calibration, modern pool carbonates from Soreq cave in Israel (Bar-Matthews et al., 1996), and previous slow CO₂ degassing experiments (Wiedner et al., 2008).

2.5.4 Non-equilibrium carbon and oxygen isotope fractionations during fast calcite precipitation in stalagmite – like settings

Carbonate precipitation on the apex of stalagmites occurs in thin layers that consist of either calcite or aragonite (Baker et al., 1998; Wassenburg et al., 2013). The thin layer-forming calcite (or aragonite) precipitates from a thin CaCO₃ saturated water film (≈ 0.01 cm thickness) in a time scale of seconds (Buhmann and Dreybrodt, 1985; Dreybrodt and Scholz, 2011; Hansen et al., 2013). This fast precipitation of CaCO₃ might allow the kinetically controlled incorporation of carbon and oxygen isotopes into stalagmites. Evidence of such kinetic isotope effects has been reported in a large compilation study of

natural speleothems by Mickler et al. (2006). These authors stressed the significance of in-cave processes on controlling these kinetic isotope effects. In the following sections, the effects of different in-cave processes on carbon and oxygen isotopes in stalagmites are discussed.

2.5.4.1 Flow rate and temperature effects on carbon isotope compositions of the calcite precipitated on the upper watch glasses

The flow rate controls the exposure time that is spent by the drip water in contact with cave atmosphere, including: 1) the flow time of drip water on cave ceiling and/or stalactite surface; and 2) the drip time interval between two subsequent drops on the apex of stalagmite. In most natural caves and our experimental design, the use of drip time interval to model the effect of the flow rate would be misleading and underestimating its effect on the isotopic composition of calcite precipitated. Therefore, in this study, we estimated the flow rate effect based upon the exposure time (i.e., flow time along the Pyrex tube channel plus the residence time on the apex of the upper watch glass).

The $\delta^{13}\text{C}_{\text{Cc}}$ value of the calcite formed on the upper watch glass increases substantially with exposure time and temperature (Fig. 2.6a). Three potential processes can control the $\delta^{13}\text{C}_{\text{Cc}}$ value. The first process is the equilibrium carbon isotope fractionation between calcite and HCO_3^- ($1000\ln^{13}\alpha_{\text{Cc-DIC}}$), which is independent of the exposure time and temperature (Romanek et al., 1992). An average $1000\ln^{13}\alpha_{\text{Cc-DIC}}$ value of 1.7 ‰ at quasi isotope equilibrium conditions in the lower watch glass was measured

in this study. However, the $\delta^{13}\text{C}_{\text{Cc}}$ values of the calcite formed on the upper watch glass are significantly higher than that value expected at carbon isotope equilibrium with initial DIC.

The second process is the DIC depletion caused by calcite precipitation and its associated fast CO_2 degassing (Mickler et al., 2006; Mühlinghaus et al., 2009; Dreybrodt and Scholz, 2011). This is a time- and temperature-dependant process, enriching the DIC reservoir of the drip water in ^{13}C and thus increasing the $\delta^{13}\text{C}_{\text{Cc}}$ value of precipitating calcite relative to that formed in earlier stages of calcite precipitation. Unlike the situation in the lower watch glass, the DIC concentration on the upper watch glass cannot reliably be measured because of the small drop volume and the short residence time of the drop on the upper watch glass. Therefore, we quantified the depletion of DIC concentration in the drip water by using the following theoretical equation proposed by Dreybrodt, (1988):

$$[\text{DIC}] (t) = \{([\text{DIC}] (t_0) - [\text{DIC}]_{\text{eq}}) \exp (t / t_{pr})\} + [\text{DIC}]_{\text{eq}} \quad (2.2)$$

$[\text{DIC}] (t)$ is the remaining fraction of the DIC at any exposure time, whereas $[\text{DIC}] (t_0)$ and $[\text{DIC}]_{\text{eq}}$ are the initial DIC (measured) and DIC at equilibrium with cave pCO_2 (calculated using “ 2 x equation 11” in Kaufmann, 2003). t is the exposure time and t_{pr} is the time constant of precipitation, which is the ratio of liquid film thickness (a) to rate precipitation constant (α_{pr} ; temperature dependant) (Dreybrodt, 1988; Baker et al., 1998). For simplification, we used the thin film thickness of 0.008 cm on the upper watch glasses (see section 2.3.1) as an approximation to the film thickness along the stalactite–stalagmite path in this study. The estimated $[\text{DIC}] (t)$ for each flow rate at the three experimental temperatures are listed in Table S2 in the supplementary materials.

Subsequently, the Rayleigh distillation approach (e.g., Mickler et al., 2004; Mickler et al., 2006) was used to estimate the effect of DIC depletion on the $\delta^{13}\text{C}_{\text{Cc}}$ value of calcite the on upper watch glass. In our Rayleigh distillation calculations, the temperature independent $^{13}\alpha_{\text{Cc-HCO}_3^-}$ value of our own (1.0017) and the temperature-dependent $^{13}\alpha_{\text{CO}_2\text{-HCO}_3^-}$ values from Mook (2000) were used. Figure 2.6a shows a significant positive offset between the measured and calculated $\delta^{13}\text{C}_{\text{Cc}}$ values based upon the first and second processes. This offset ($\Delta^{13}\text{C}_{\text{measured-calculated}}$) largely increases with time and temperature, discounting uncertainties in carbon isotope fractionation and time constant for CaCO_3 precipitation for the causes of these increases. This leads us to attribute a part or all of $\Delta^{13}\text{C}_{\text{measured-calculated}}$ offsets to the third process: CO_2 exchange between the DIC species in drip water and the cave atmosphere (Hendy, 1971; Scholz et al., 2009; Dreybrodt and Scholz, 2011; Deininger et al., 2012; Dreybrodt et al., 2016).

The third process is carbon isotope exchange between DIC species in the drip water and CO_2 in the cave atmosphere, which is also time- and temperature-dependent (Hendy, 1971; Dreybrodt and Scholz, 2011; Dreybrodt et al., 2016). This process is facilitated by the diffusion of cave CO_2 into the drip water and the subsequent conversion of $\text{CO}_{2(\text{aq})}$ to HCO_3^- (Dreybrodt and Scholz, 2011; Dreybrodt et al., 2016). The effect of this exchange on carbon isotopes in DIC has been theoretically and experimentally investigated by Dreybrodt et al. (2016) and can be calculated as follows:

$$\Delta^{13}\text{C exchange} = [\delta^{13}\text{C}_{\text{DICin}} - \delta^{13}\text{C}_{\text{DICeq}}] * [1 - \exp(-t / t_{\text{ex}})] \quad (2.3)$$

Where $\Delta^{13}\text{C exchange}$ is the effect of CO_2 exchange on $\delta^{13}\text{C}_{\text{DIC}}$. t and t_{ex} are the exposure time and the exchange time, respectively. One can calculate t_{ex} using Dreybrodt et al.

(2016)'s updated equation of $t_{\text{ex}} = t_{\text{red}} [\text{HCO}_3^-]/[\text{K}_\text{H} \cdot \text{pCO}_2]$ where t_{red} and $[\text{K}_\text{H} \cdot \text{pCO}_2]$ are dependant of temperature (Dreybrodt et al., 2016). Values of $\delta^{13}\text{C}_{\text{DICin}}$ and $\delta^{13}\text{C}_{\text{DICeq}}$ are the initial $\delta^{13}\text{C}$ of the DIC and $\delta^{13}\text{C}$ of DIC at equilibrium with CO_2 in cave atmosphere.

For all experiments, the calculated $\Delta^{13}\text{C}$ exchange based upon different flow times and temperatures is significantly smaller than the difference between the measured $\delta^{13}\text{C}_{\text{Cc}}$ and the calculated $\delta^{13}\text{C}_{\text{Cc}}$ values based upon the first and second processes. For instance, at 15 °C, the $\Delta^{13}\text{C}$ exchange is 0.15 ‰, 0.34 ‰ and 0.89 ‰ whereas the $\Delta^{13}\text{C}_{\text{measured-calculated}}$ is 1.14 ‰, 1.66 ‰ and 3.13 ‰ under fast, intermediate and slow flow rates, respectively. Similarly, the $\Delta^{13}\text{C}$ exchange is 0.32 ‰, 0.81 ‰ and 2.41 ‰ at 25 °C while the $\Delta^{13}\text{C}_{\text{measured-calculated}}$ is 2.23 ‰, 4.96 ‰ and 8.21 ‰ under fast, intermediate and slow flow rates, respectively. These differences might be a result of underestimating the degree of CO_2 exchange between the DIC species in drip water and the cave atmosphere in the theoretical and experimental study by Dreybrodt et al. (2016). The theoretical calculations in the latter study were validated with several experiments of carbon isotope exchange between pure NaHCO_3 solution and ambient CO_2 . These NaHCO_3 experiments excluded potential effects of carbonate precipitation on the CO_2 exchange. The carbonate precipitation might enhance carbon isotope exchange between DIC in drip water and atmospheric CO_2 by two processes: 1) accelerating the diffusion of CO_2 in the drip water, or/and 2) allowing an additional pathway for CO_2 exchange (i.e., carbon isotope exchange between CO_2 in cave atmosphere and CO_2 released into the drip water by CaCO_3 precipitation; Deininger et al., 2012). Alternatively, the kinetic fractionation model of Dreybrodt (2008) can account for this difference observed between the measured $\delta^{13}\text{C}_{\text{Cc}}$

values in this study and the calculated effect of the three processes, if a high hypothetical value of γ is used (e.g., ≥ 1.01).

The implications of our experimental observations for carbon isotope compositions of natural stalagmites are:

- 1) In general, flow rate and temperature can kinetically affect the $\delta^{13}\text{C}_{\text{Cc}}$ in stalagmites (Fig. 2.6a). In natural caves of quasi stable temperature, variability of $\delta^{13}\text{C}_{\text{Cc}}$ in an individual stalagmite should be interpreted as a wet/dry indicator, reflecting the intensity of water discharge (flow rate) in the karst area either on glacial/interglacial (e.g., Frumkin et al., 2000) or seasonal scale (e.g., Ridley et al., 2015). In contrast, significant drifts in $\delta^{13}\text{C}_{\text{Cc}}$ of a stalagmite from a cave site, characterized by a constant drip rate, would reflect changes in temperature, most likely warm/cold climates.
- 2) Carbon isotope exchange between DIC in drip water and cave CO_2 can obscure the vegetation signals recorded in $\delta^{13}\text{C}_{\text{DIC}}$ of drip water and thereby the $\delta^{13}\text{C}_{\text{Cc}}$ of stalagmites. The carbon isotope exchange effect on $\delta^{13}\text{C}_{\text{Cc}}$ in stalagmites depends on how far the $\delta^{13}\text{C}_{\text{DIC}}$ in drip water is from isotope equilibrium with $\delta^{13}\text{C}$ of cave CO_2 . In well-ventilated caves, $\delta^{13}\text{C}$ of cave CO_2 is similar to that of the atmospheric CO_2 (-8 ‰), which is not in isotope equilibrium with the $\delta^{13}\text{C}_{\text{DIC}}$ in drip water (-14 to -12 ‰). As a result, complete carbon isotope exchange between DIC in drip water and cave CO_2 can result in a 15 ‰ shift in the $\delta^{13}\text{C}_{\text{DIC}}$ and therefore obscure the vegetation type (C3 and C4) signals in the $\delta^{13}\text{C}_{\text{Cc}}$ of a stalagmite. In contrast, carbon isotope exchange in closed caves is negligible

because the source of cave CO₂ is either soil CO₂ or CO₂ degassing from drip water or soil, which are in carbon isotope equilibrium with the drip water.

In summary, in-cave kinetic effects on the $\delta^{13}\text{C}_{\text{Cc}}$ of stalagmites might be climatically controlled by the rainfall amount and/or surface temperature. However, changes in the flow route of the drip water might result in isotopic noises in the $\delta^{13}\text{C}_{\text{Cc}}$ record of any stalagmites (Baldini et al., 2006).

2.5.4.2 Flow rate and temperature effects on oxygen isotope compositions of the calcite precipitated on the upper watch glasses

At isotopic equilibrium, the $\delta^{18}\text{O}_{\text{Cc}}$ value in a carbonate–CO₂–water system of a known $\delta^{18}\text{O}_{\text{H}_2\text{O}}$ value is solely governed by temperature, maintaining a unique fractionation factor between calcite and water at a given temperature (Urey, 1948; Epstein et al., 1953; Kim and O’Neil, 1997; Coplen, 2007). Figure 2.6b demonstrates that the $1000\ln^{18}\alpha_{\text{Cc-H}_2\text{O}}$ values increase with increasing exposure time at constant temperature, indicating the prevalence of the oxygen isotope non-equilibrium at longer exposure times. Interestingly, these non-equilibrium isotope effects show apparent temperature dependency at the same exposure time (flow rate). Flow rate effects on the $\delta^{18}\text{O}_{\text{Cc}}$ can result in $1000\ln^{18}\alpha_{\text{Cc-H}_2\text{O}}$ values varying from those of the experimental and theoretical calibrations (e.g., results from the lower watch glass in this study; Kim and O’Neil, 1997; Horita and Clayton, 2007) up to $1000\ln^{18}\alpha_{\text{Cc-H}_2\text{O}}$ values higher than Coplen (2007)’s empirical oxygen isotope fractionation (Fig. 2.6b).

The variability in the flow rate induces non-equilibrium oxygen isotope effects and two potential mechanisms are proposed for these isotopic effects: the evaporation of the

drip water and DIC depletion in the drip water (Mickler et al., 2004; Dreybrodt, 2008; Day and Henderson, 2011; Deininger et al., 2012; Dreybrodt and Deininger, 2014). Evaporation of the drip water can increase the $\delta^{18}\text{O}_{\text{Cc}}$ by two different mechanisms. The first isotopic mechanism has been thoroughly discussed in the theoretical work of Deininger et al. (2012) and Dreybrodt and Deininger (2014). In brief, evaporation of water increases the $\delta^{18}\text{O}_{\text{H}_2\text{O}}$. A subsequent transfer of this increment to the $\delta^{18}\text{O}$ value of DIC is limited by the slow oxygen isotope exchange between DIC species and water especially at low temperatures (Beck et al., 2005). Therefore, a minor or negligible isotopic effect is expected in the $\delta^{18}\text{O}$ record of stalagmites below 35 °C. Nevertheless, the physical evaporation process can instantaneously increase the $\delta^{18}\text{O}_{\text{Cc}}$ by evaporative cooling. Evaporative cooling lowers the temperature of the drip water with respect to the surrounding atmosphere, inducing larger oxygen isotope fractionation between calcite and water (e.g., Cuthbert et al., 2014). In this study, all of the experiments were carried out at a constant high relative humidity condition (95%) to minimize evaporation and isotopic effects. Figure 2.5 demonstrates that the effect of one hour evaporation at 95% relative humidity is insignificant.

During fast precipitation of carbonates, the DIC depletion quickly increases the $\delta^{18}\text{O}$ of bicarbonate ions in cave drip water and consequently the $\delta^{18}\text{O}_{\text{Cc}}$ due to the preferential C^{16}O_2 outgassing (Mickler et al., 2004; Day and Henderson, 2011). In this case, the $1000\ln^{18}\alpha_{\text{Cc-H}_2\text{O}}$ value increases with increasing flow time and temperature, hampering the use of the $1000\ln^{18}\alpha_{\text{Cc-H}_2\text{O}}$ as a paleotemperature proxy (Fig. 2.6b). Oxygen isotope exchange between bicarbonate ion and water can reduce (eliminate) the DIC

depletion impact on the $\delta^{18}\text{O}_{\text{Cc}}$; however, this exchange is negligible during fast CaCO_3 precipitation at low temperatures (Beck et al., 2005). In order to quantify the DIC depletion effect on the $\delta^{18}\text{O}_{\text{Cc}}$, the Rayleigh distillation model was employed by using the calculated [DIC] (t) and the oxygen isotope fractionation factors from Beck et al. (2005) and this study. The combination of these fractionation factors results in a total oxygen isotope fractionation factor between the products (CaCO_3 , CO_2 and H_2O) and reactant (HCO_3^-) during the carbonate precipitation of 0.9964, 0.9967 and 0.9969 at 15, 25 and 32 °C respectively. Consequently, the output of the Rayleigh distillation model is in a good agreement with the observed $1000\ln^{18}\alpha_{\text{Cc-H}_2\text{O}}$ in both trend and magnitude (Fig. 2.12). However, the slight offset between the predicted and observed $1000\ln^{18}\alpha_{\text{Cc-H}_2\text{O}}$ may be attributed to uncertainty in the time constant of precipitation (t_{pr}) (Polag et al., 2010; Hansen et al., 2013) due to the splashing of the drip water on the surface of the upper watch glasses. Applying Dreybrodt's (2008) kinetic model to quantify the effect of the DIC depletion on the $\delta^{18}\text{O}_{\text{Cc}}$ yields a perfect match between the predicted and observed $1000\ln^{18}\alpha_{\text{Cc-H}_2\text{O}}$. For example, using hypothetical γ values of 0.997 and 0.999 explains observed $1000\ln^{18}\alpha_{\text{Cc-H}_2\text{O}}$ values at 15 and 25 °C. Regardless of the small offset observed with the use of Rayleigh model, there is adequate agreement between Dreybrodt (2008)'s kinetic model and Rayleigh distillation model when both are used to estimate the effect of the DIC depletion on the $\delta^{18}\text{O}_{\text{Cc}}$ (in contrast to $\delta^{13}\text{C}_{\text{Cc}}$). The potential reasons of this agreement are: 1) The main difference between Rayleigh model and Dreybrodt (2008)'s kinetic model is the addition of γ to the kinetic model; when γ value is ≈ 1 , both models

show agreement; and 2) In contrast to carbon isotopes, the large water reservoir works as a barrier avoiding oxygen isotope exchange between DIC species and cave CO₂.

The implications of these results regarding the use of $\delta^{18}\text{O}_{\text{Cc}}$ in natural stalagmites are summarized below:

- 1) The calcite at the surface of stalagmites most likely precipitates under non-equilibrium oxygen isotope conditions (e.g., Mickler et al., 2006).
- 2) Similar to the case for $\delta^{13}\text{C}_{\text{Cc}}$, the non-equilibrium oxygen isotope record in a stalagmite might be used to infer qualitative paleoclimate information (e.g., wet/dry and warm/cold) only if the interpretation is supported by a rigorous cave monitoring program to characterize the stability of drip rate and cave temperature.
- 3) The replication test suggested by Dorale and Liu (2009) does not necessarily prove that the test-passed stalagmites are formed under equilibrium oxygen isotope conditions because the magnitude and direction of non-equilibrium isotope effects can be reproduced even under different conditions.

2.5.5 Insights into the debate of equilibrium oxygen isotope fractionation between calcite and water in cave environments

Oxygen isotope equilibrium between calcite and water can be attained under complete oxygen isotope exchange between DIC species and water, although continuous carbonate growth can only occur with chemical disequilibrium. In contrast, if there is no isotopic buffering effect between DIC and water, then non-equilibrium oxygen isotope effects in calcite precipitated from water can be modelled based upon the decrease in DIC

concentration (chemical disequilibrium; Eq. 2.2; Fig. 2.12). The maximum non-equilibrium isotope effect in calcite is expected when available DIC [$\text{DIC}_{\text{in}} - \text{DIC}_{\text{eq}}$] is completely consumed for CaCO_3 precipitation. To quantify the maximum non-equilibrium isotope effects in cave environments, our experimental oxygen isotope data from the slow and fast CaCO_3 precipitation experiments at 32 °C were used. At 32 °C, the slow precipitation experiments define the equilibrium $1000\ln^{18}\alpha_{\text{Cc-H}_2\text{O}}$ value, which should be the same as the one from the early stage of the fast CaCO_3 precipitation (i.e., 1 to 2 % of the [$\text{DIC}_{\text{in}} - \text{DIC}_{\text{eq}}$] is consumed) whereas the fast precipitation on the upper watch glasses covers CaCO_3 precipitation up to 87% of the [$\text{DIC}_{\text{in}} - \text{DIC}_{\text{eq}}$]. The exponential rise to maximum fit of the $1000\ln^{18}\alpha_{\text{Cc-H}_2\text{O}}$ versus the exposure time from the slow and fast CaCO_3 precipitation experiments at 32 °C yields the following equation:

$$1000\ln^{18}\alpha_{\text{Cc-H}_2\text{O}} (\text{neq}) = 26.86 (\pm 0.13) + 2.95 (\pm 0.14) [1 - \exp(-bt)] \quad (2.4)$$

$$R^2 = 0.98; P < 0.0001$$

where $1000\ln^{18}\alpha_{\text{Cc-H}_2\text{O}} (\text{neq})$ is non-equilibrium oxygen fractionation between calcite and water that is a function of flow time or the percentage of the remaining DIC fraction. The first number (26.86 ± 0.13) indicates the equilibrium $1000\ln^{18}\alpha_{\text{Cc-H}_2\text{O}}$, whereas the second number (2.95 ± 0.14) is the maximum predicted non-equilibrium oxygen isotope effect. $[1 - \exp(-bt)]$ term expresses the consumed fraction of [$\text{DIC}_{\text{in}} - \text{DIC}_{\text{eq}}$].

The maximum predicted non-equilibrium oxygen isotope effect is constrained to the equilibrium oxygen isotope fractionation between bicarbonate and water ($1000\ln^{18}\alpha_{\text{HCO}_3^- - \text{H}_2\text{O}}$) in the carbonate– CO_2 –water system (Fig. 2.13; Beck et al., 2005). This is consistent with the mechanism that was suggested by Clark and Lauriol (1992) and Mickler et al.

(2004) for non-equilibrium oxygen isotope effects. Beck et al. (2005) determined the equilibrium $1000\ln^{18}\alpha_{\text{HCO}_3^- \text{-H}_2\text{O}}$ between 15 °C and 40 °C. In this temperature range, the average difference between the equilibrium $1000\ln^{18}\alpha_{\text{HCO}_3^- \text{-H}_2\text{O}}$ from Beck et al. (2005) and equilibrium $1000\ln^{18}\alpha_{\text{Cc-H}_2\text{O}}$ in this study is $2.73 \pm 0.15 \text{ ‰}$, which is near identical to the maximum predicted non-equilibrium oxygen isotope effect of $2.95 \pm 0.14 \text{ ‰}$. A compilation of farmed modern calcite samples from nine monitoring caves in America, Europe and Asia shows a good agreement with the maximum predicted non-equilibrium oxygen isotope effect and equilibrium $1000\ln^{18}\alpha_{\text{Cc-H}_2\text{O}}$ in this study (Fig. 2.14). This agreement provides an opportunity to project the $1000\ln^{18}\alpha_{\text{Cc-H}_2\text{O}}$ from non-equilibrium to equilibrium conditions and therefore reconstruct absolute paleotemperature in ancient speleothems. Reynard et al. (2011) suggested that calcium isotopes in speleothem calcite can be used to infer the consumed DIC fraction from the drip water (PCP) and thus can provide approximate estimation of the remaining fraction of the DIC $[1 - \exp(-bt)]$. Moreover, the $\delta^{18}\text{O}$ values of fluid inclusions and calcite in speleothems potentially enable us to define $1000\ln^{18}\alpha_{\text{Cc-H}_2\text{O}}$ (*neq*). Therefore, one can obtain equilibrium $1000\ln^{18}\alpha_{\text{Cc-H}_2\text{O}}$ value by applying geochemical information obtained from fluid inclusion and calcium isotope studies from ancient speleothems to the equation (2.4).

The equilibrium $1000\ln^{18}\alpha_{\text{Cc-H}_2\text{O}}$ value determined in this study from the slow CaCO_3 precipitation experiments at the lower watch glass, along with the predicted maximum non-equilibrium oxygen isotope effect, can account for the variations existed in the published $1000\ln^{18}\alpha_{\text{Cc-H}_2\text{O}}$ values (e.g., Coplen, 2007; Tremaine et al., 2011; Fig. 2.13). For instance, Tremaine et al. (2011) used farmed calcite from the Hollow Ridge

Cave (HRC) in Florida and other caves in order to empirically define the temperature dependency of $1000\ln^{18}\alpha_{\text{Cc-H}_2\text{O}}$. This empirical approach might introduce some systematic errors in their $1000\ln^{18}\alpha_{\text{Cc-H}_2\text{O}}$ value because some calcite samples were impacted by PCP. Tremaine and Froelich (2013) later reported a wide range of PCP in the HRC by using trace elements. This explains the positive deviation of their empirical approach compared to our measured equilibrium $1000\ln^{18}\alpha_{\text{Cc-H}_2\text{O}}$ value.

2.6 Conclusions

A series of laboratory-based experiments were performed under tightly controlled conditions (i.e., temperature, relative humidity, solution chemistry, flow rate and cave $p\text{CO}_2$) in order to identify controlling factors on the growth rate of stalagmites and their carbon and oxygen isotopic systematics by simulating the growth of speleothems on a stalagmite surface as well as a pool setting in nature. The followings are the key findings of the experiments:

- (1) Both flow rate and temperature can affect the growth rate of stalagmites. When one or both of these variables are small, then a corresponding weak effect is observed on the growth rate.
- (2) Speleothems may form at or close to isotopic equilibrium under two CaCO_3 precipitation conditions: (i) slow CaCO_3 precipitation in pool settings and (ii) fast CaCO_3 precipitation at a stalagmite's surface under a fast flow rate of drip water. Under the first condition, an average temperature-independent $1000\ln^{13}\alpha_{\text{Cc-HCO}_3^-}$ value of 1.7 ± 0.7 ‰ was observed whereas the $1000\ln^{18}\alpha_{\text{Cc-H}_2\text{O}}$ value shows a strong correlation with temperature:

$$1000\ln^{18}\alpha_{\text{Cc-H}_2\text{O}} = 18.33 (10^3/T) - 33.14 \quad R^2 = 0.97; P < 0.0001$$

This relation is statistically indistinguishable from the equation proposed by Kim and O'Neil (1997) when the same acid fractionation factor is used for both studies.

- (3) DIC depletion during fast CaCO_3 precipitation can induce non-equilibrium isotope effects in stalagmites for both carbon and oxygen. Moreover, CO_2 exchange between DIC in drip water and cave atmosphere can promote non-equilibrium isotope effects for carbon. Both increasing temperature and flow rate intensify the non-equilibrium isotope effects in these two processes.
- (4) Non-equilibrium isotope effects in stalagmites can obscure the vegetation and absolute temperature information in the $\delta^{13}\text{C}_{\text{Cc}}$ and $\delta^{18}\text{O}_{\text{Cc}}$. However, a non-equilibrium isotope-based stalagmite record might be suitable to extract qualitative paleoclimate information (e.g., wet/dry and warm/cold) as the non-equilibrium carbon and oxygen isotope effects are controlled by temperature and/or flow rate (rainfall amount). Therefore, cave monitoring study is necessary to better interpret such non-equilibrium isotope record.
- (5) There is a potential to project the non-equilibrium oxygen isotope effects in stalagmites back to the equilibrium datum if a well-developed PCP proxy will be established in cave environments. Calcium isotopes might be a suitable candidate for this purpose because of the stability in the calcium source (host rock) over time and the weak temperature dependence of calcium isotope fractionation between carbonate and water and (Reynard et al., 2011).

(6) The results of these experiments provide reproducible data points from a wide range of temperature and flow rate that can be used to validate and improve existing numerical models. Moreover, the observed carbon and oxygen fractionation factors between calcite and water in this study can be used to assess equilibrium/disequilibrium isotope conditions in modern caves.

2.7 Acknowledgments

The authors would like to thank Martin Kynf for his technical support in the McMaster Research Group for Stable Isotopologues (MRSI). This work was supported by the NSERC Discovery Grants Program (386188-2010) to S.-T. Kim.

2.8 References

- Asmerom Y., Polyak V. J. and Burns S. J. (2010) Variable winter moisture in the southwestern United States linked to rapid glacial climate shifts. *Nat. Geosci.* **3**, 114–117.
- Baker A., Genty D., Dreybrodt W., Barnes W. L., Mockler N. J. and Grapes J. (1998) Testing Theoretically Predicted Stalagmite Growth Rate with Recent Annually Laminated Samples: Implications for Past Stalagmite Deposition. *Geochim. Cosmochim. Acta* **62**, 393–404.
- Baldini J. U. L., McDermott F., Baker A., Baldini L. M., Matthey D. P. and Railsback L. B. (2005) Biomass effects on stalagmite growth and isotope ratios: A 20th century analogue from Wiltshire, England. *Earth Planet. Sci. Lett.* **240**, 486–494.
- Baldini J., McDermott F. and Fairchild I. (2006a) Spatial variability in cave drip water hydrochemistry: implications for stalagmite paleoclimate records. *Chem. Geol.* **235**, 390–404.
- Banner J. L., Guilfoyle A., James E. W., Stern L. A. and Musgrove M. (2007) Seasonal Variations in Modern Speleothem Calcite Growth in Central Texas, U.S.A. *J. Sediment. Res.* **77**, 615–622.
- Bar-Matthews M., Ayalon A., Matthews A., Sass E. and Halicz L. (1996) Carbon and oxygen isotope study of the active water-carbonate system in a karstic Mediterranean cave.pdf. *Geochim. Cosmochim. Acta* **60**, 337–347.
- Beck W. C., Grossman E. L. and Morse J. W. (2005) Experimental studies of oxygen isotope fractionation in the carbonic acid system at 15°, 25°, and 40°C. *Geochim. Cosmochim. Acta* **69**, 3493–3503.
- van Breukelen M. R., Vonhof H. B., Hellstrom J. C., Wester W. C. G. and Kroon D. (2008) Fossil dripwater in stalagmites reveals Holocene temperature and rainfall variation in Amazonia. *Earth Planet. Sci. Lett.* **275**, 54–60.
- Buhmann D. and Dreybrodt W. (1985) The kinetics of calcite dissolution and precipitation in geologically relevant situations of karst areas. 2. Closed system. *Chem. Geol.* **53**, 109–124.
- Casteel R. C. and Banner J. L. (2015) Temperature-driven seasonal calcite growth and drip water trace element variations in a well-ventilated Texas cave: Implications for speleothem paleoclimate studies. *Chem. Geol.* **392**, 43–58.
- Chacko T. and Deines P. (2008) Theoretical calculation of oxygen isotope fractionation

- factors in carbonate systems. *Geochim. Cosmochim. Acta* **72**, 3642–3660.
- Clark I. D. and Lauriol B. (1992) Kinetic enrichment of stable isotopes in cryogenic calcites. *Chem. Geol.* **102**, 217–228.
- Coplen T. B. (2007) Calibration of the calcite-water oxygen-isotope geothermometer at Devils Hole, Nevada, a natural laboratory. *Geochim. Cosmochim. Acta* **71**, 3948–3957.
- Cuthbert M. O., Baker A., Jex C. N., Graham P. W., Treble P. C., Andersen M. S. and Ian Acworth R. (2014) Drip water isotopes in semi-arid karst: Implications for speleothem paleoclimatology. *Earth Planet. Sci. Lett.* **395**, 194–204.
- Daëron M., Guo W., Eiler J., Genty D., Blamart D., Boch R., Drysdale R., Maire R., Wainer K. and Zanchetta G. (2011) $^{13}\text{C}^{18}\text{O}$ clumping in speleothems: Observations from natural caves and precipitation experiments. *Geochim. Cosmochim. Acta* **75**, 3303–3317.
- Day C. C. and Henderson G. M. (2011) Oxygen isotopes in calcite grown under cave-analogue conditions. *Geochim. Cosmochim. Acta* **75**, 3956–3972.
- Deines P., Langmuir D. and Harmon R. S. (1974) Stable carbon isotope ratios and the existence of a gas phase in the evolution of carbonate ground waters. *Geochim. Cosmochim. Acta* **38**, 1147–1164.
- Deininger M., Fohlmeister J., Scholz D. and Mangini A. (2012) Isotope disequilibrium effects: The influence of evaporation and ventilation effects on the carbon and oxygen isotope composition of speleothems - A model approach. *Geochim. Cosmochim. Acta* **96**, 57–79.
- Dorale J. A. (1998) Climate and Vegetation History of the Midcontinent from 75 to 25 ka: A Speleothem Record from Crevice Cave, Missouri, USA. *Science*. **282**, 1871–1874.
- Dorale J. a. and Liu Z. (2009) Limitations of hendy test criteria in judging the paleoclimatic suitability of speleothems and the need for replication. *J. Cave Karst Stud.* **71**, 73–80.
- Dreybrodt, W. (1988) Processes in Karst Systems. Physics, Chemistry and Geology. Springer Series in Physical Environment 4. Springer, Berlin/Heidelberg/New York.
- Dreybrodt W. (2008) Evolution of the isotopic composition of carbon and oxygen in a calcite precipitating $\text{H}_2\text{O}-\text{CO}_2-\text{CaCO}_3$ solution and the related isotopic composition of calcite in stalagmites. *Geochim. Cosmochim. Acta* **72**, 4712–4724.

- Dreybrodt W. (2012) Comment on “ Oxygen isotopes in calcite grown under cave-analogue conditions” by C.C. Day and G.M. Henderson. *Geochim. Cosmochim. Acta* **85**, 383–387.
- Dreybrodt W. and Deininger M. (2014) The impact of evaporation to the isotope composition of DIC in calcite precipitating water films in equilibrium and kinetic fractionation models. *Geochim. Cosmochim. Acta* **125**, 433–439.
- Dreybrodt W., Hansen M. and Scholz D. (2016) Processes affecting the stable isotope composition of calcite during precipitation on the surface of stalagmites: Laboratory experiments investigating the isotope exchange between DIC in the solution layer on top of a speleothem and the CO₂ of the cave at. *Geochim. Cosmochim. Acta* **174**, 247–262.
- Dreybrodt W. and Scholz D. (2011) Climatic dependence of stable carbon and oxygen isotope signals recorded in speleothems: From soil water to speleothem calcite. *Geochim. Cosmochim. Acta* **75**, 734–752.
- Epstein S., Buchsbaum R., Lowenstam H. and Urey H. C. (1953) Revised carbonate-water isotopic temperature scale. *Bull. Geol. Soc. Am.* **64**, 1315–1326.
- Fantidis J. and Ehhalt D. H. (1970) Variations of the carbon and oxygen isotopic composition in stalagmites and stalactites: Evidence of non-equilibrium isotopic fractionation. *Earth Planet. Sci. Lett.* **10**, 136–144.
- Feng W., Casteel R. C., Banner J. L. and Heinze-Fry A. (2014) Oxygen isotope variations in rainfall, drip-water and speleothem calcite from a well-ventilated cave in Texas, USA: Assessing a new speleothem temperature proxy. *Geochim. Cosmochim. Acta* **127**, 233–250.
- Franke H. W. (1965) The theory behind stalagmite shapes. *Studies in Speleology* **1**, 89–95.
- Frisia S., Fairchild I. J., Fohlmeister J., Miorandi R., Spötl C. and Borsato A. (2011) Carbon mass-balance modelling and carbon isotope exchange processes in dynamic caves. *Geochim. Cosmochim. Acta* **75**, 380–400.
- Frumkin a, Ford D. C. and Schwarcz H. P. (2000) Paleoclimate and vegetation of the last glacial cycles in Jerusalem from a speleothem record. *Global Biogeochem. Cycles* **14**, 863–870.
- Gat J. R. and Gonfiantini R. (1981) Stable Isotope Hydrology: deuterium and Oxygen-18 in the Water Cycle. IAEA, Technical Reports Series No. 210, Vienna.

- Gascoyne M., Schwarcz H. P. and Ford D. C. (1980) A paleotemperature record for the mid-Wisconsin in Vancouver Island. *Nature* **285**, 474–476.
- Gebbinck C. D. K., Kim S. T., Knyf M. and Wyman J. (2014) A new online technique for the simultaneous measurement of the $\delta^{13}\text{C}$ value of dissolved inorganic carbon and the $\delta^{18}\text{O}$ value of water from a single solution sample using continuous-flow isotope ratio mass spectrometry. *Rapid Commun. Mass Spectrom.* **28**, 553–562.
- Genty D. and Quinif Y. (1996) Annually laminated sequences in the internal structure of some Belgian stalagmites - importance for paleoclimatology. *J. Sediment. Petrol.* **66**, 275–288.
- Hansen M., Dreybrodt W. and Scholz D. (2013) Chemical evolution of dissolved inorganic carbon species flowing in thin water films and its implications for (rapid) degassing of CO_2 during speleothem growth. *Geochim. Cosmochim. Acta* **107**, 242–251.
- Hellstrom J., McCulloch M. and Stone J. (1998) A Detailed 31,000-Year Record of Climate and Vegetation Change, from the Isotope Geochemistry of Two New Zealand Speleothems. *Quat. Res.* **178**, 167–178.
- Hendy C. (1971) The isotopic geochemistry of speleothems - I. The calculation of the effects of different modes of formation on the isotopic composition of speleothems and their applicability as paleoclimatic indicators. *Geochim. Cosmochim. Acta* **35**, 801–824.
- Horita J. and Clayton R. N. (2007) Comment on the studies of oxygen isotope fractionation between calcium carbonates and water at low temperatures by Zhou and Zheng (2003; 2005). *Geochim. Cosmochim. Acta* **71**, 3131–3135.
- Kaufmann G. (2003) Stalagmite growth and palaeo-climate: The numerical perspective. *Earth Planet. Sci. Lett.* **214**, 251–266.
- Kim S. T., Coplen T. B. and Horita J. (2015) Normalization of stable isotope data for carbonate minerals: Implementation of IUPAC guidelines. *Geochim. Cosmochim. Acta* **158**, 276–289.
- Kim S.-T., Hillaire-Marcel C. and Mucci A. (2006) Mechanisms of equilibrium and kinetic oxygen isotope effects in synthetic aragonite at 25°C. *Geochim. Cosmochim. Acta* **70**, 5790–5801.
- Kim S.-T. and O’Neil J. (1997) Equilibrium and nonequilibrium oxygen isotope effects in synthetic carbonates. *Geochim. Cosmochim. Acta* **61**, 3461–3475.

- Kaufmann G. (2003) Stalagmite growth and palaeo-climate: the numerical perspective. *Earth Planet. Sci. Lett.* **214**, 251–266.
- Kluge T., Affek H. P., Dublyansky Y. and Spötl C. (2014) Devils Hole paleotemperatures and implications for oxygen isotope equilibrium fractionation. *Earth Planet. Sci. Lett.* **400**, 251–260.
- Mickler P. J., Banner J. L., Stern L., Asmerom Y., Edwards R. L. and Ito E. (2004) Stable isotope variations in modern tropical speleothems: Evaluating equilibrium vs. kinetic isotope effects. *Geochim. Cosmochim. Acta* **68**, 4381–4393.
- Mickler P. J., Stern L. A. and Banner J. L. (2006) Large kinetic isotope effects in modern speleothems. *Bull. Geol. Soc. Am.* **118**, 65–81.
- Mattey D., Fairchild I., Atkinson T., Latin J., Ainsworth M. and Durell R. (2010) Seasonal microclimate control of calcite fabrics, stable isotopes and trace elements in modern speleothem from St. Michaels Cave, Gibraltar. *J. Geol. Soc.* **336**, 323–344, London, Special Publications.
- Mook W. G. (2000) Volume 1: Introduction – theory, methods, review. In: *Environmental Isotopes in the Hydrological Cycle. Principles and Applications*.
- Mühlhous C., Scholz D. and Mangini A. (2007) Modelling stalagmite growth and $\delta^{13}\text{C}$ as a function of drip interval and temperature. *Geochim. Cosmochim. Acta* **71**, 2780–2790.
- Mühlhous C., Scholz D. and Mangini A. (2009) Modelling fractionation of stable isotopes in stalagmites. *Geochim. Cosmochim. Acta* **73**, 7275–7289.
- O’Neil J., Clayton R. and Mayeda T. (1969) Oxygen Isotope Fractionation in Divalent Metal Carbonates. *J. Chem. Phys.* **51**, 5547–5558.
- Polag D., Scholz D., Mühlhous C., Spötl C., Schröder-Ritzrau A., Segl M. and Mangini A. (2010) Stable isotope fractionation in speleothems: Laboratory experiments. *Chem. Geol.* **279**, 31–39.
- Reynard L. M., Day C. C. and Henderson G. M. (2011) Large fractionation of calcium isotopes during cave-analogue calcium carbonate growth. *Geochim. Cosmochim. Acta* **75**, 3726–3740.
- Ridley H. E., Asmerom Y., Baldini J. U. L., Breitenbach S. F. M., Aquino V. V., Pruffer K. M., Culleton B. J., Polyak V., Lechleitner F. a., Kennett D. J., Zhang M., Marwan N., Macpherson C. G., Baldini L. M., Xiao T., Peterkin J. L., Awe J. and Haug G. H. (2015) Aerosol forcing of the position of the intertropical convergence zone since ad

1550. *Nat. Geosci.* **8**, 195–200.

- Riechelmann D. F. C., Deininger M., Scholz D., Riechelmann S., Schröder-Ritzrau A., Spötl C., Richter D. K., Mangini A. and Immenhauser A. (2013) Disequilibrium carbon and oxygen isotope fractionation in recent cave calcite: Comparison of cave precipitates and model data. *Geochim. Cosmochim. Acta* **103**, 232–244.
- Romanek C. S., Grossman E. L. and Morse J. W. (1992) Carbon isotopic fractionation in synthetic aragonite and calcite: Effects of temperature and precipitation rate. *Geochim. Cosmochim. Acta* **56**, 419–430.
- Scholz D., Mühlinghaus C. and Mangini A. (2009) Modelling $\delta^{13}\text{C}$ and $\delta^{18}\text{O}$ in the solution layer on stalagmite surfaces. *Geochim. Cosmochim. Acta* **73**, 2592–2602.
- Sharma T. and Clayton R. N. (1965) Measurement of $\text{O}^{18}/\text{O}^{16}$ ratios of total oxygen of carbonates. *Geochim. Cosmochim. Acta* **29**, 1347–1353.
- Tremaine D. M. and Froelich P. N. (2013) Speleothem trace element signatures: A hydrologic geochemical study of modern cave dripwaters and farmed calcite. *Geochim. Cosmochim. Acta* **121**,
- Tremaine D. M., Froelich P. N. and Wang Y. (2011) Speleothem calcite farmed in situ: Modern calibration of $\delta^{18}\text{O}$ and $\delta^{13}\text{C}$ paleoclimate proxies in a continuously-monitored natural cave system. *Geochim. Cosmochim. Acta* **75**, 4929–4950.
- Urey H. C. (1948) Oxygen isotopes in nature and in the laboratory. *Science* **108**, 489–496.
- Wainer K., Genty D., Blamart D., Daëron M., Bar-Matthews M., Vonhof H., Dublyansky Y., Pons-Branchu E., Thomas L., van Calsteren P., Quinif Y. and Caillon N. (2011) Speleothem record of the last 180 ka in Villars cave (SW France): Investigation of a large $\delta^{18}\text{O}$ shift between MIS6 and MIS5. *Quat. Sci. Rev.* **30**, 130–146.
- Wassenburg J. A., Immenhauser A., Richter D. K., Niedermayr A., Riechelmann S., Fietzke J., Scholz D., Jochum K. P., Fohlmeister J., Schröder-Ritzrau A., Sabaoui A., Riechelmann D. F. C., Schneider L. and Esper J. (2013) Moroccan speleothem and tree ring records suggest a variable positive state of the North Atlantic Oscillation during the Medieval Warm Period. *Earth Planet. Sci. Lett.* **375**, 291–302.
- Wiedner E., Scholz D., Mangini A., Polag D., Mühlinghaus C. and Segl M. (2008) Investigation of the stable isotope fractionation in speleothems with laboratory experiments. *Quat. Int.* **187**, 15–24.

2.9 Tables

Table 2.1
Calcite growth mass (mg/d) on the upper watch glasses at different temperatures and flow rates.

Experiment ID	Duration (d)	Total ppt (mg)	ppt /day (mg / d)
MIE-15-95-09-F	14	63.0	4.5
MIE-15-95-09-I	14	39.0	2.8
MIE-15-95-09-S	14	16.4	1.2
MIE-15-95-10-F	15	58.2	3.9
MIE-15-95-10-I	15	46.7	3.1
MIE-15-95-10-S	15	19.8	1.3
MIE-15-95-11-F	15	61.5	4.1
MIE-15-95-11-I	15	47.4	3.2
MIE-15-95-11-S	15	24.6	1.6
	F		4.2 ± 0.3
Mean ± Std	I		3.0 ± 0.2
	S		1.4 ± 0.2
MIE-25-95-06-F	6	97.2	16.2
MIE-25-95-06-I	7	39.5	5.6
MIE-25-95-07-F	7	129.2	18.5
MIE-25-95-07-I	7	58.8	8.4
MIE-25-95-07-S	7	19.2	2.7
MIE-25-95-08-F	7	128.4	18.3
MIE-25-95-08-I	7	50.3	7.2
MIE-25-95-08-S	7	20.0	2.9
MIE-25-95-09-F	7	113.0	16.1
MIE-25-95-09-I	7	44.5	6.4
MIE-25-95-09-S	7	13.1	1.9
MIE-25-95-10-F	7	112.1	16.0
MIE-25-95-10-S	7	14.0	2.0
	F		17.0 ± 1.3
Mean ± Std	I		6.9 ± 1.2
	S		2.4 ± 0.5
MIE-32-95-02-F	5.7	157.4	27.6
MIE-32-95-02-I	5.7	53.5	9.4
MIE-32-95-02-S	5.7	10.2	1.8
MIE-32-95-03-F	5.8	165.8	28.6
MIE-32-95-03-I	5.8	53.8	9.3
MIE-32-95-03-S	5.8	13.4	2.3
MIE-32-95-04-F	5.9	173.9	29.5
MIE-32-95-04-I	5.9	50.6	8.6
MIE-32-95-04-S	5.9	17.3	2.9
	F		28.6 ± 0.9
Mean ± Std	I		9.1 ± 0.4
	S		2.3 ± 0.6

Experiment ID = Initials of the experiment performer - temperature - relative humidity - run# -flow rate

Flow rate: F, I and S are Fast, Intermediate and Slow

Ph.D. Thesis – M. EL-Shenawy; McMaster University – School of Geography and Earth Sciences

Table 2.2
Chemical and isotopic composition of the liquids in the experimnts.

Experiment ID	Flow rate / watch glass	DIC conc. (mmol/L)	SD (1σ)	DIC conc. (%)	Average pH	SD (1σ)	Average		SD(1σ)	N	
							$\delta^{13}\text{C}_{\text{DIC}}(\text{‰})$	$\delta^{18}\text{O}_{\text{H}_2\text{O}}(\text{‰})$			
							VPDB	VSMOW			
MIE-15-95-9	F.U										
	I.U	3.83	0.14	100	7.22	0.17	-32.11	0.44	-7.67	0.11	55
	S.U										
	F.L	2.73	0.17	71.28	7.99		-26.46	0.17	-6.96	0.02	2
	I.L	2.34	0.09	61.10	7.92		-21.78	0.13	-6.58	0.02	2
	S.L	2.03	0.01	53.00	7.95		-15.77	0.01	-6.04	0.06	2
MIE-15-95-10	F.U										
	I.U	3.86	0.16	100	7.23	0.16	-32.63	0.53	-7.67	0.16	55
	S.U										
	F.L	2.76	0.12	71.50	7.96		-26.99	0.02	-7.29	0.04	2
	I.L	2.29	0.06	59.33	7.86		-22.23	0.05	-6.78	0.03	2
	S.L	2.04	0.11	52.85	7.91		-16.41	0.02	-6.17	0.02	2
MIE-15-95-11	F.U										
	I.U	3.95	0.13	100	7.22	0.17	-32.53	0.36	-7.50	0.21	55
	S.U										
	F.L	2.72	0.15	68.86	8.00		-27.54	0.10	-7.15	0.00	2
	I.L	2.44	0.15	61.77	7.96		-20.71	0.10	-6.69	0.01	2
	S.L	2.34	0.15	59.24	7.95		-16.08	0.10	-6.34	0.02	2
MIE-25-95-6	F.U										
	I.U	na	na		7.09	0.20	na	na	-7.72	0.06	22
	F.L	na	na		8.20		na	na	-7.1	0.02	2
	I.L	na	na		8.19		na	na	-6.61	0.01	2
MIE-25-95-7	F.U										
	I.U	4.19	0.16	100	7.07	0.17	-35.09	0.51	-7.66	0.03	26
	S.U										
	F.L	2.33	0.02	55.61	8.18		-25.18	0.12	-7.14	0.03	2
	I.L	1.84	0.13	43.91	8.14		-16.65	0.04	-6.66	0.01	2
	S.L	1.50	0.05	35.80	8.14		-10.72	0.05	-6.37	0.01	2
MIE-25-95-8	F.U										
	I.U	4.19	0.12	100	7.02	0.15	-34.54	0.35	-7.61	0.10	26
	S.U										
	F.L	2.41	0.33	57.52	8.04		-25.16	0.07	-7.05	0.03	2
	I.L	1.72	0.05	41.05	8.04		-15.58	0.02	-6.54	0.03	2
	S.L	1.48	0.00	35.32	8.04		-9.24	0.04	-6.37	0.04	2
MIE-25-95-9	F.U										
	I.U	4.09	0.15	100	7.05	0.19	-34.44	0.43	-7.74	0.05	26
	S.U										
	F.L	2.53	0.09	61.86	8.04		-25.82	0.02	-7.25	0.03	2
	I.L	1.79	0.00	43.77	8.09		-15.57	0.06	-6.63	0.05	2
	S.L	1.60	0.03	39.12	8.11		-10.12	0.03	-6.36	0.02	2
MIE-25-95-10	F.U										
	S.U	4.08	0.15	100	7.06	0.19	-34.51	0.40	-7.73	0.05	12
	F.L	2.51	0.04	61.52	8.08		-25.76	0.06	-7.19	0.01	2
	S.L	1.56	0.02	38.24	8.03		-10.51	0.14	-6.40	0.01	2
MIE-32-95-2	F.U										
	I.U	4.14	0.15	100	7.07	0.20	-35.43	0.38	-7.81	0.05	30
	S.U										
	F.L	1.88	0.04	45.41	8.16		-22.86	0.03	-7.14	0.03	2
	I.L	1.28	0.03	30.92	8.07		-13.63	0.08	-6.43	0.02	2
	S.L	1.30	0.01	31.40	8.2		-9.24	0.00	-6.22	0.01	2
MIE-32-95-3	F.U										
	I.U	4.15	0.15	100	7.04	0.20	-35.04	0.38	-7.71	0.14	30
	S.U										
	F.L	1.89	0.04	45.54	8.13		-22.88	0.03	-6.98	0.04	2
	I.L	1.37	0.05	33.01	8.12		-12.61	0.03	-6.38	0.02	2
	S.L	1.28	0.04	30.84	8.11		-9.37	0.03	-6.18	0.01	2
MIE-32-95-4	F.U										
	I.U	4.13	0.15	100	7.03	0.20	-35.19	0.49	-7.61	0.05	30
	S.U										
	F.L	1.81	0.04	43.83	8.09		-23.23	0.06	-6.80	0.04	2
	I.L	1.19	0.02	28.81	8.03		-13.86	0.02	-6.51	0.00	2
	S.L	1.16	0.04	28.09	8.09		-10.30	0.01	-6.12	0.00	2

Experiment ID = Initials of the experiment performer - temperature - relative humidity - run#

Flow rate/ watch glass = Fast (F), Intermediate (I) and Slow (S) / Upper watch glass (U) and Lower watch glass (L)

N = number of measurements on the starting solution (1 L bottle) before and after its replacement by a new bottle

Ph.D. Thesis – M. EL-Shenawy; McMaster University – School of Geography and Earth Sciences

Table 2.3
Carbon and oxygen isotope compositions of the calcite in the experiments.

Experiment	Drip rate	$\delta^{18}\text{O}_{\text{Cc}}$ (‰ VSMOW)					$\delta^{13}\text{C}_{\text{Cc}}$ (‰ VPDB)					$1000\ln^{18}\alpha_{\text{Cc-H}_2\text{O}}$	$1000\ln^{13}\alpha_{\text{Cc-DIC}}$	$\delta^{13}\text{C}_{\text{Cc}} - \delta^{13}\text{C}_{\text{DICin}}$
		S0	S1/5	S2	Average	Apex SD (1 σ)	S0	S1/5	S2	Average	Apex SD (1 σ)			
MIE-15-95-9	F.U	23.29	23.17	23.21	23.22	0.06	-28.95	-28.95	-29.09	-29.00	0.08	30.66	na	3.11
	I.U	23.25	23.2	23.2	23.22	0.03	-28.18	-28.38	-28.28	-28.28	0.10	30.65	na	3.83
	S.U	23.86	23.83	23.93	23.87	0.05	-26.29	-26.23	-25.96	-26.16	0.18	31.29	na	5.95
	F.L	23.72	23.69	na	23.71	0.02	-24.24	-24.13	na	-24.18	0.08	30.41	2.34	10.67
	I.L	23.91	23.8	na	23.86	0.08	-19.87	-19.69	na	-19.78	0.13	30.18	2.04	12.33
	S.L	24.14	24.36	na	24.25	0.16	-15.23	-15.03	na	-15.13	0.14	30.02	0.65	16.98
MIE-15-95-10	F.U	23.34	na	23.12	23.23	0.16	-29.62	na	-29.71	-29.66	0.06	30.66	na	2.97
	I.U	23.33	23.33	23.31	23.32	0.01	-28.71	-28.72	-28.60	-28.68	0.07	30.78	na	3.95
	S.U	23.93	23.95	23.97	23.95	0.02	-26.32	-26.18	-26.14	-26.21	0.09	31.38	na	6.42
	F.L	23.6	23.7	na	23.65	0.07	-25.24	-25.25	na	-25.25	0.01	30.69	1.79	8.87
	I.L	23.93	23.94	na	23.94	0.01	-20.31	-20.26	na	-20.29	0.04	30.46	1.99	12.35
	S.L	24.35	24.34	na	24.35	0.01	-14.21	-14.53	na	-14.37	0.23	30.24	2.07	18.26
MIE-15-95-11	F.U	23.27	23.2	23.24	23.24	0.04	-29.22	-29.17	-29.22	-29.20	0.03	30.50	na	3.33
	I.U	23.53	23.51	23.53	23.52	0.01	-28.36	-28.30	-28.38	-28.35	0.04	30.77	na	4.18
	S.U	23.98	23.99	24.08	24.02	0.06	-26.67	-26.57	-26.29	-26.51	0.20	31.26	na	6.02
	F.L	23.7	23.72	na	23.71	0.01	-25.23	-25.20	na	-25.22	0.02	30.61	2.39	8.29
	I.L	23.9	23.88	na	23.89	0.01	-19.25	-19.58	na	-19.42	0.23	30.32	1.32	13.12
	S.L	24.04	24.05	na	24.05	0.01	-14.84	-14.83	na	-14.84	0.01	30.12	1.26	17.70
MIE-25-95-6	F.U	21.78	21.77	21.84	21.79	0.04	-29.65	-29.61	-29.34	-29.54	0.17	29.31	na	na
	I.U	22.36	22.44	22.50	22.43	0.07	-26.89	-26.81	-26.59	-26.76	0.16	29.93	na	na
	F.L	21.35	21.42	na	21.39	0.05	-22.82	-22.64	na	-22.73	0.13	28.29	na	na
	I.L	21.56	21.51	na	21.53	0.03	-14.21	-14.20	na	-14.21	0.00	27.94	na	na
MIE-25-95-7	F.U	21.68	21.70	21.79	21.72	0.06	-30.15	-30.13	-29.73	-30.00	0.24	29.18	na	5.09
	I.U	22.41	22.50	22.46	22.46	0.05	-27.05	-26.95	-26.86	-26.95	0.10	29.90	na	8.14
	S.U	na	23.34	23.37	23.36	0.02	na	-23.22	-23.27	-23.25	0.04	30.78	na	11.85
	F.L	21.21	21.28	na	21.25	0.05	-23.28	-23.08	na	-23.18	0.14	28.19	2.05	14.44
	I.L	21.44	21.47	na	21.46	0.02	-15.40	-15.32	na	-15.36	0.06	27.91	1.31	19.73
	S.L	21.98	22.01	na	22.00	0.02	-8.82	-8.68	na	-8.75	0.10	28.15	1.99	26.34
MIE-25-95-8	F.U	21.76	21.71	21.76	21.74	0.03	-30.14	-30.18	-29.93	-30.08	0.13	29.15	na	4.46
	I.U	22.39	22.38	22.44	22.40	0.03	-26.98	-26.80	-26.75	-26.84	0.12	29.80	na	7.70
	S.U	23.36	23.44	23.53	23.44	0.09	-22.93	-22.53	-22.49	-22.65	0.24	30.81	na	11.89
	F.L	21.60	21.58	na	21.59	0.01	-23.57	-23.30	na	-23.44	0.19	28.44	1.77	12.28
	I.L	21.67	21.64	na	21.66	0.02	-15.28	-14.83	na	-15.06	0.32	27.99	0.53	19.49
	S.L	21.84	21.89	na	21.87	0.04	-8.88	-8.87	na	-8.88	0.01	28.02	0.37	25.67
MIE-25-95-9	F.U	21.60	21.57	21.64	21.60	0.04	-30.10	-30.15	-29.89	-30.05	0.14	29.14	na	4.39
	I.U	22.24	22.22	22.24	22.23	0.01	-26.82	-26.78	-26.77	-26.79	0.03	29.76	na	7.65
	S.U	23.31	23.29	23.24	23.28	0.04	-22.05	-22.07	-22.12	-22.08	0.04	30.78	na	12.36
	F.L	21.45	21.38	na	21.42	0.05	-23.35	-23.28	na	-23.32	0.05	28.47	2.57	13.69
	I.L	21.40	21.47	na	21.44	0.05	-14.73	-14.33	na	-14.53	0.28	27.86	1.06	19.91
	S.L	21.76	21.80	na	21.78	0.03	-8.96	-9.19	na	-9.08	0.16	27.93	1.06	25.37
MIE-25-95-10	F.U	21.60	21.65	21.61	21.62	0.03	-30.26	-30.41	-30.47	-30.38	0.11	29.15	na	4.13
	S.U	23.32	na	23.64	23.48	0.23	-22.32	na	-21.93	-22.12	0.28	30.97	na	12.39
	F.L	21.28	21.32	22.09	21.30	0.03	-23.81	-23.82	na	-23.82	0.01	28.29	1.99	10.69
	S.L	21.99	21.98	22.08	21.99	0.00	-9.23	-8.92	na	-9.08	0.22	28.17	1.45	25.43
MIE-32-95-2	F.U	20.57	20.63	20.65	20.62	0.04	-30.17	-30.06	-29.94	-30.06	0.12	28.25	na	5.37
	I.U	21.68	21.67	21.73	21.69	0.03	-25.45	-25.18	-24.96	-25.20	0.25	29.30	na	10.30
	S.U	21.97	22.05	22.11	22.04	0.07	-21.79	-21.64	-21.25	-21.56	0.28	29.64	na	13.99
	F.L	20.22	20.53	na	20.38	0.22	-22.18	-21.03	na	-21.61	0.81	27.34	1.28	15.04
	I.L	20.79	20.55	na	20.67	0.17	-13.31	-12.10	na	-12.71	0.86	26.91	0.94	22.73
	S.L	20.75	21.17	na	20.96	0.30	-8.41	-8.45	na	-8.43	0.03	26.98	0.82	27.00
MIE-32-95-3	F.U	20.86	20.87	20.90	20.88	0.02	-29.15	-29.12	-28.98	-29.08	0.09	28.40	na	5.96
	I.U	21.87	na	21.94	21.91	0.05	-24.37	na	-24.24	-24.31	0.09	29.41	na	10.74
	S.U	22.14	22.22	22.23	22.20	0.05	-21.53	-20.84	-20.77	-21.05	0.42	29.69	na	13.99
	F.L	19.98	19.94	na	19.96	0.03	-20.75	-20.55	na	-20.65	0.14	26.77	2.28	15.25
	I.L	20.27	20.24	na	20.26	0.02	-11.66	-11.34	na	-11.50	0.23	26.45	1.12	23.54
	S.L	20.50	20.69	na	20.60	0.13	-7.32	-7.12	na	-7.22	0.14	26.58	2.17	27.82
MIE-32-95-4	F.U	20.84	20.78	20.83	20.82	0.03	-29.55	-29.62	-29.51	-29.56	0.06	28.24	na	5.63
	I.U	21.82	21.85	21.90	21.86	0.04	-24.74	-24.59	-24.48	-24.60	0.13	29.26	na	10.59
	S.U	22.30	22.26	22.25	22.27	0.03	-21.61	-21.58	-21.47	-21.55	0.07	29.66	na	13.64
	F.L	20.25	20.30	na	20.25	0.04	-20.89	-20.59	na	-20.74	0.21	26.87	2.55	15.13
	I.L	20.48	20.48	na	20.48	0.00	-11.37	-11.52	na	-11.45	0.11	26.80	2.45	23.75
	S.L	20.55	20.78	na	20.67	0.16	-7.50	na	na	-7.50	na	26.59	2.83	27.69

Experiment ID = Initials of the experiment performer - temperature - relative humidity - run#
Flow rate/ watch glass = Fast (F), Intermediate (I) and Slow (S) / Upper watch glass (U) and Lower watch glass (L)
S = Location of sampling; S0 is the center of the watch glass, S1/5 is 1 cm from the center of the upper watch glass or 5 cm from the center of the lower watch glass, S2 is 2 cm far from the center of the upper watch glass

2.10 Figures

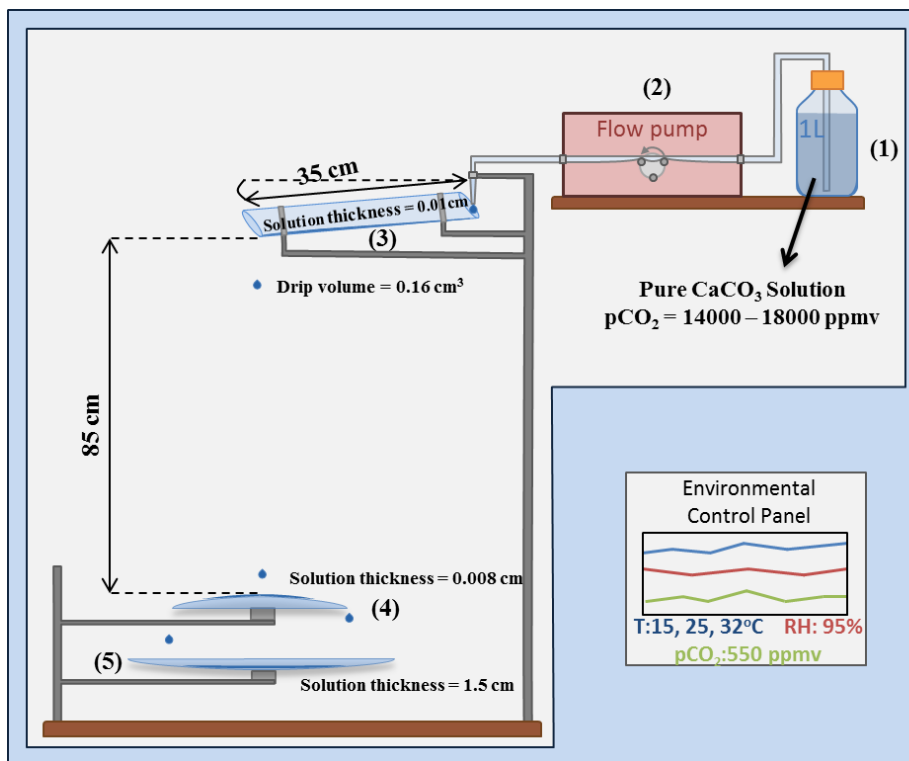
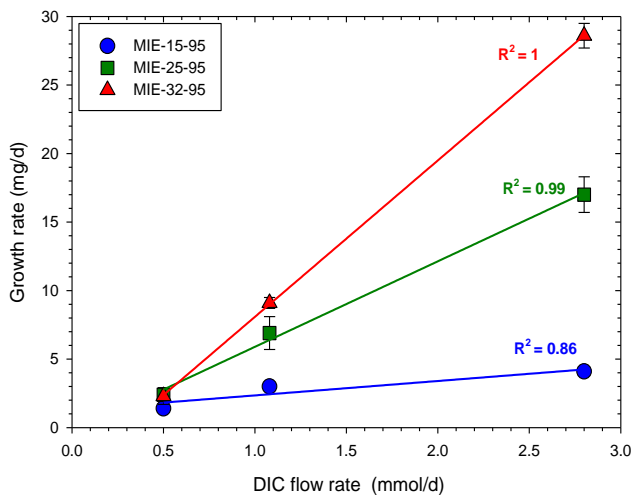


Fig. 2.1: Schematic diagram of the experimental setup. The five components of this setup are described in section 2.3.1. Three typical setups to the one shown in the figure are fitted into the growth chamber (Model: Conversion CMP4030).

a)



b)

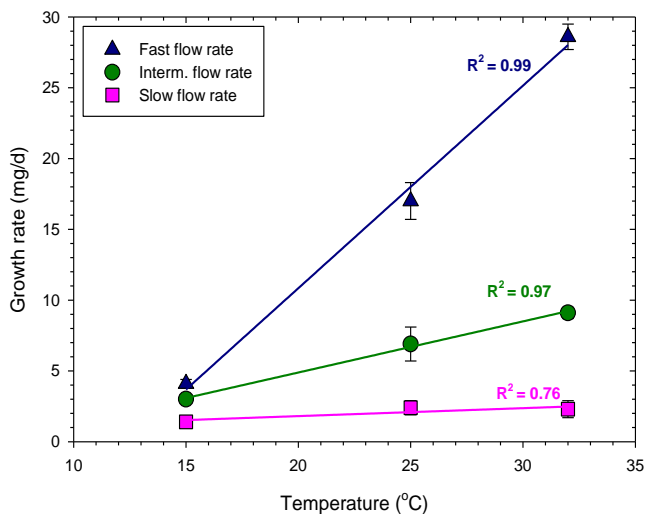
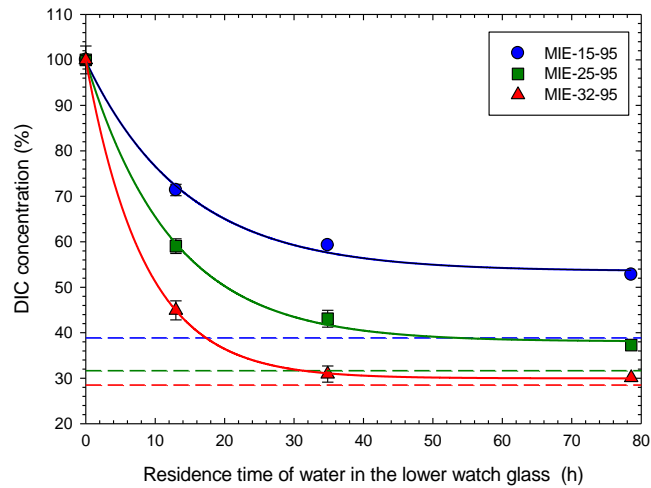


Fig. 2.2: (a) Growth rate (mg/d) of calcite on the upper watch glasses as a function of DIC flow rate (mmol/d). (b) Growth rate (mg/d) of calcite on the upper watch glasses as a function of temperature ($^{\circ}$ C). Error bars indicate mean \pm 1SD (n \geq 3).

Residence

a)



b)

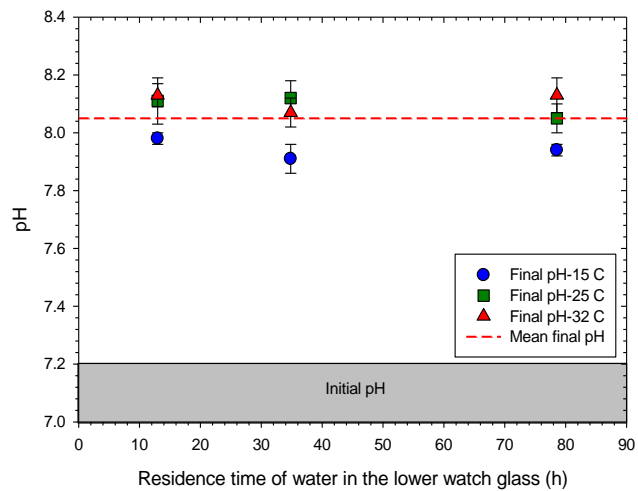


Fig. 2.3: (a) Relative DIC concentration (% of initial value) of the final water in the lower watch glass versus the residence time [h]. Solid lines are exponential fit to the experimental data from the three temperatures whereas dashed lines indicate the DIC concentration at equilibrium with our cave pCO_2 (estimated from Kaufmann, 2003). (b) pH of the final water versus the residence time [h]. The grey shaded area shows the range of the initial pH of the drip water. Error bars indicate mean \pm 1SD ($n \geq 3$).

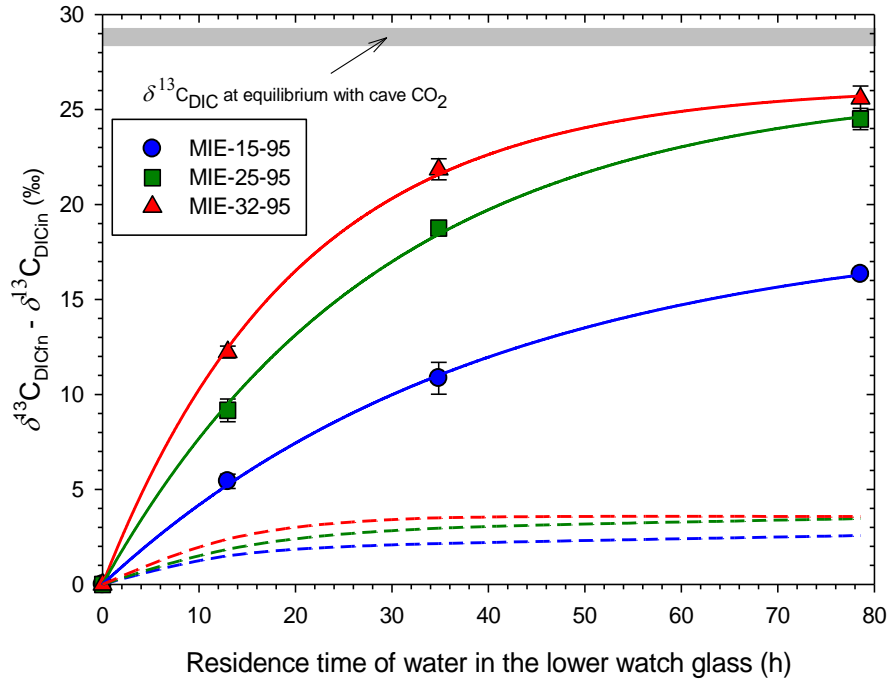


Fig. 2.4: Measured temporal evolution of carbon isotope compositions ($\delta^{13}\text{C}_{\text{DIC}_{\text{fin}}} - \delta^{13}\text{C}_{\text{DIC}_{\text{in}}}$) in DIC during calcite precipitation in the lower watch glasses. Solid lines are exponential rise to maximum fit of the experimental data. Dashed lines correspond to the predicted temporal evolution of the $\delta^{13}\text{C}_{\text{DIC}}$ based upon Rayleigh distillation model (fractionation factors from Mook, 2000 and Romanek et al., 1992). Grey shaded area indicates the predicted $\delta^{13}\text{C}_{\text{DIC}_{\text{fin}}}$ at carbon isotope equilibrium with cave CO_2 . Error bars indicate mean \pm 1SD ($n \geq 3$).

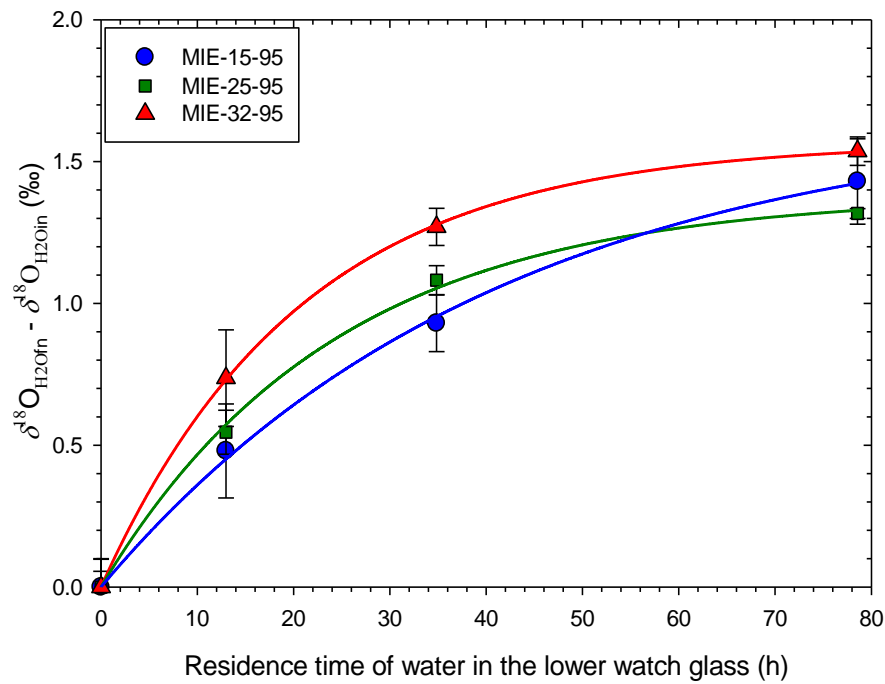
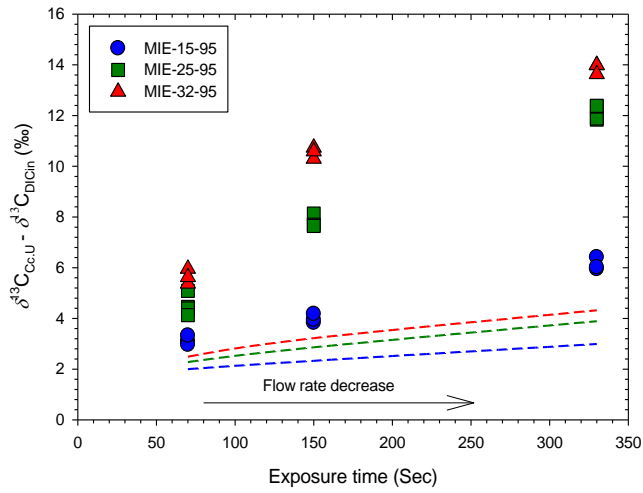


Fig. 2.5: Temporal evolution of oxygen isotopes ($\delta^{18}\text{O}_{\text{H}_2\text{O}_{\text{fln}}} - \delta^{18}\text{O}_{\text{H}_2\text{O}_{\text{in}}}$) of the drip water in the lower watch glass under relative humidity of 95%. Error bars indicate mean \pm 1SD ($n \geq 3$).

a)



b)

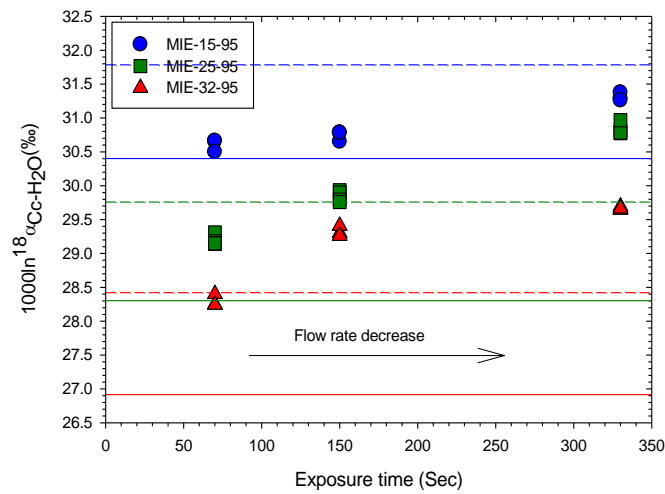


Fig. 2.6: (a) Measured differences between the carbon isotope composition of calcite ($\delta^{13}\text{C}_{\text{Cc,U}}$) formed on the upper watch glasses and that of initial DIC in drip water (i.e., $\delta^{13}\text{C}_{\text{Cc,U}} - \delta^{13}\text{C}_{\text{DICin}}$) versus the exposure time are shown by solid lines. Dashed lines indicate the predicted ($\delta^{13}\text{C}_{\text{Cc,U}} - \delta^{13}\text{C}_{\text{DICin}}$) values based upon the Rayleigh distillation. (b) Oxygen isotope fractionation between calcite formed on the upper watch glasses and water ($1000\ln^{18}\alpha_{\text{Cc-H}_2\text{Oin}}$) versus the exposure time. Horizontal solid lines define equilibrium $1000\ln^{18}\alpha_{\text{Cc-H}_2\text{O}}$ values at a given temperature based upon slow CaCO_3 precipitation experiments undertaken in this study. Horizontal dashed lines indicate corresponding equilibrium $1000\ln^{18}\alpha_{\text{Cc-H}_2\text{O}}$ values based upon Coplen (2007)'s empirical study.

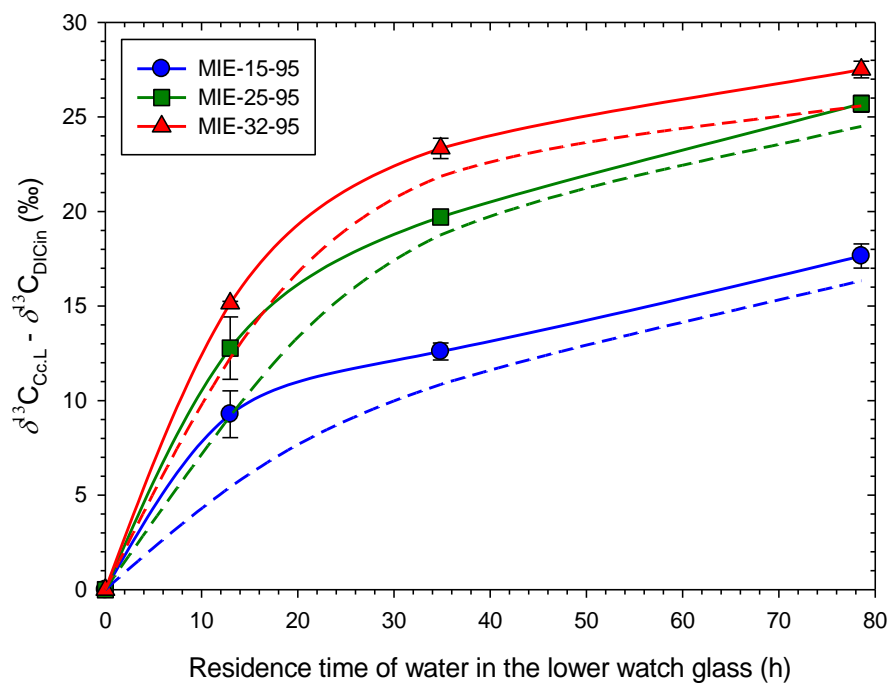


Fig. 2.7: Measured differences between the $\delta^{13}\text{C}_{\text{Cc.L}}$ of calcite formed on the lower watch glasses and the $\delta^{13}\text{C}$ of initial DIC in drip water (i.e., $\delta^{13}\text{C}_{\text{Cc.L}} - \delta^{13}\text{C}_{\text{DICin}}$) versus the residence time. Dashed lines show the measured temporal evolution of carbon isotopes ($\delta^{13}\text{C}_{\text{DICfin}} - \delta^{13}\text{C}_{\text{DICin}}$) in DIC during calcite precipitation. Error bars indicate mean \pm 1SD ($n \geq 3$).

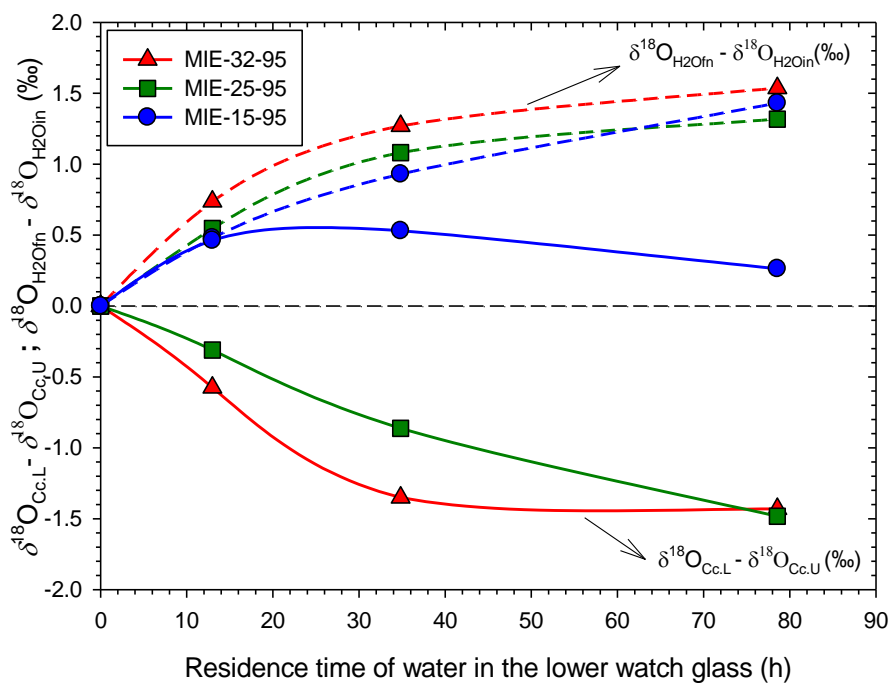


Fig. 2.8: Differences between the $\delta^{18}\text{O}_{\text{H}_2\text{O}}$ and $\delta^{18}\text{O}_{\text{C}_c}$ between the lower and upper watch glasses as a function of residence time of water in lower watch glass. Dashed lines show the average difference between final $\delta^{18}\text{O}$ of drip water ($\delta^{18}\text{O}_{\text{H}_2\text{O}_{\text{fn}}}$) in lower watch glasses and initial $\delta^{18}\text{O}$ of drip water ($\delta^{18}\text{O}_{\text{H}_2\text{O}_{\text{in}}}$) on the upper watch glasses. Solid lines indicate the average difference between the $\delta^{18}\text{O}$ of the calcite formed in the lower watch glasses ($\delta^{18}\text{O}_{\text{C}_c.\text{L}}$) and the $\delta^{18}\text{O}$ of calcite formed on the upper watch glasses ($\delta^{18}\text{O}_{\text{C}_c.\text{U}}$).

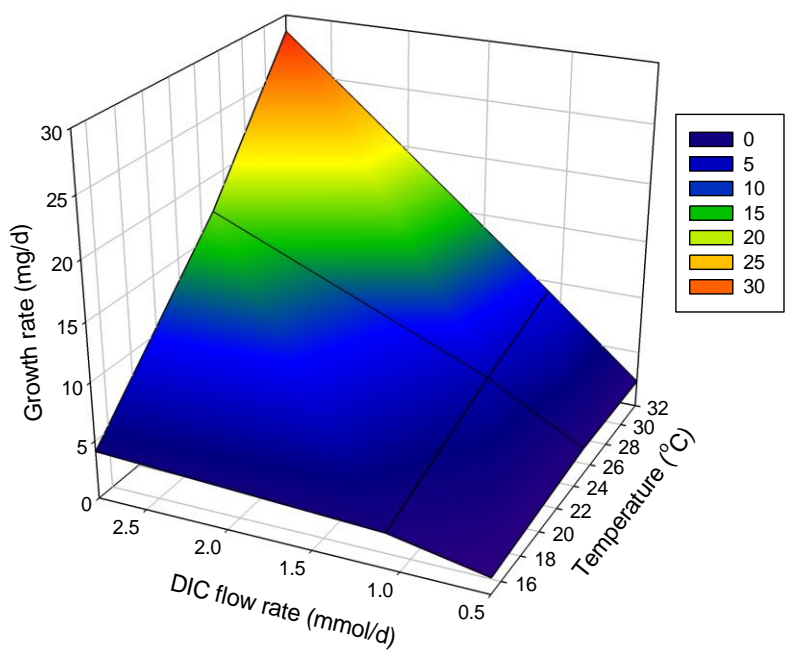


Fig. 2.9: Variation of calcite growth rate (mg/d) relative to DIC flow rate (mmol/d) and temperature (°C) under relative humidity of 95%.

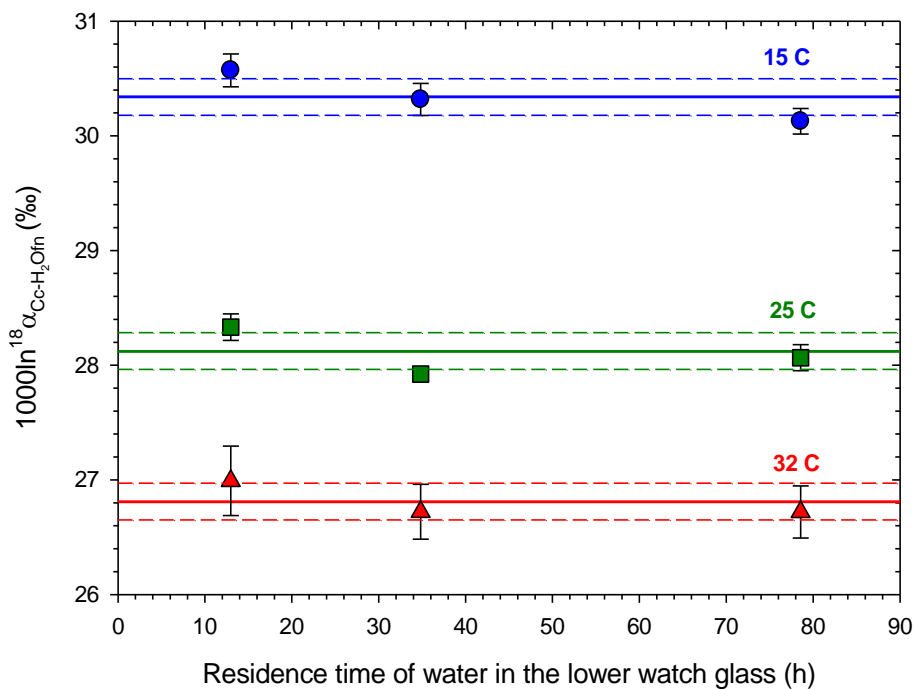


Fig. 2.10: Oxygen isotope fractionation between calcite and water in the lower watch glasses ($1000 \ln^{18} \alpha_{\text{Cc-H}_2\text{O}_{\text{fm}}}$) as a function of temperature and residence time. Solid lines indicate the average $1000 \ln^{18} \alpha_{\text{Cc-H}_2\text{O}_{\text{fm}}}$ value from the three different flow rates at each temperature, whereas the dashed lines show the analytical error of $\pm 0.16 \text{ ‰}$. Error bars indicate mean $\pm 1 \text{ SD}$ ($n \geq 3$).

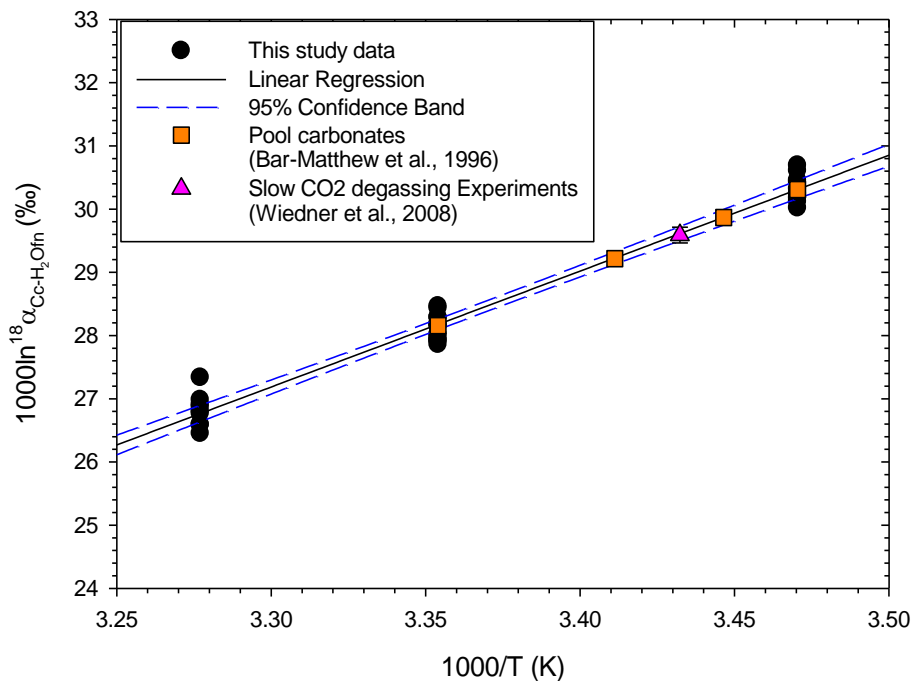


Fig. 2.11: Relation between $1000 \ln^{18} \alpha_{\text{calcite-water}}$ and temperature for slow calcite precipitation in the lower watch glasses. The least squares fit to these experimental data is proposed for the temperature dependence of the equilibrium oxygen isotope fractionation between calcite and water in cave environments. Note that pool carbonates from Soreq cave (Bar-Matthew et al., 1996) and synthetic carbonates from slow degassing experiments (Wiender et al., 2008) are in excellent agreement with the proposed relation from this study.

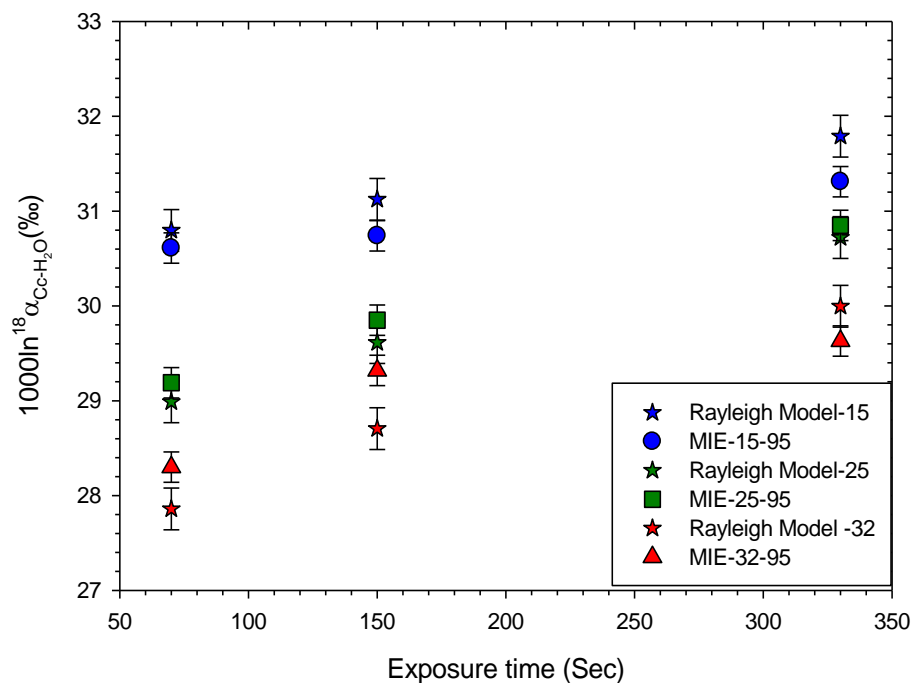


Fig. 2.12: Comparison of the measured $1000\ln^{18}\alpha_{\text{calcite-water}}$ values from this study with the predicted $1000\ln^{18}\alpha_{\text{calcite-water}}$ values based upon the Rayleigh distillation model. Colored circles and their black error bars show the average of the experimental data and the analytical error (0.16 ‰). Colored stars and their black bars show the computed values by the Rayleigh model and the standard error of the equation of the $1000\ln^{18}\alpha_{\text{calcite-water}}$ at equilibrium in this study (0.20 ‰).

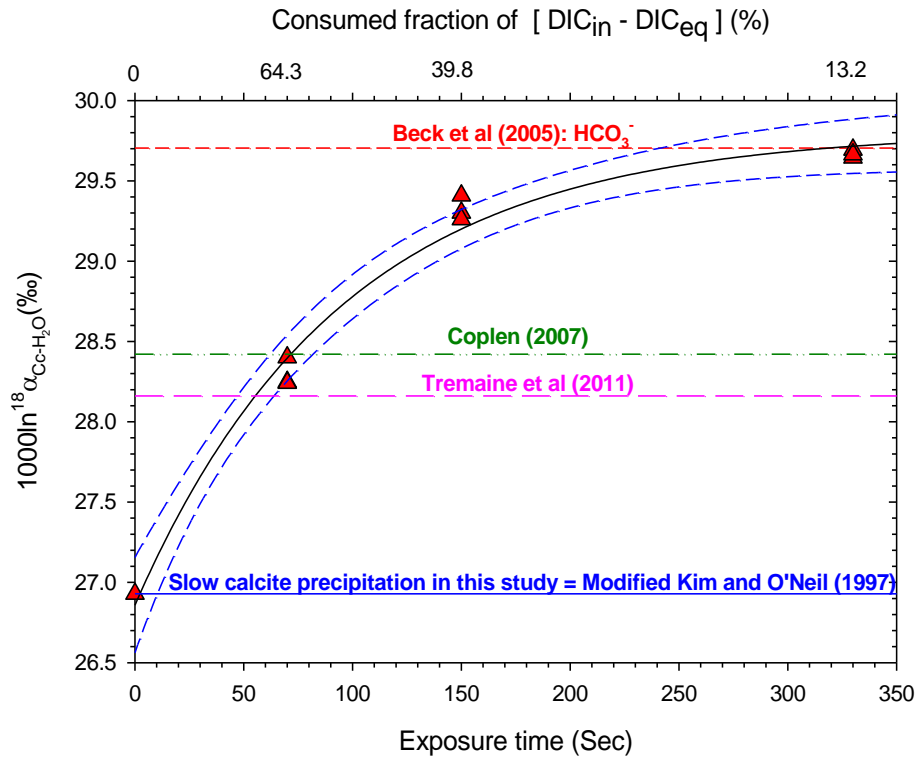


Fig. 2.13: Evolution of $1000\ln^{18}\alpha_{Cc-H_2O}$ as a function of exposure time or the depletion of DIC. Triangles show our experimental data from 32 °C. The black curve defines the exponential rise to maximum fit of the measurements; whereas the two blue dashed lines defines 95% confidence interval bands.

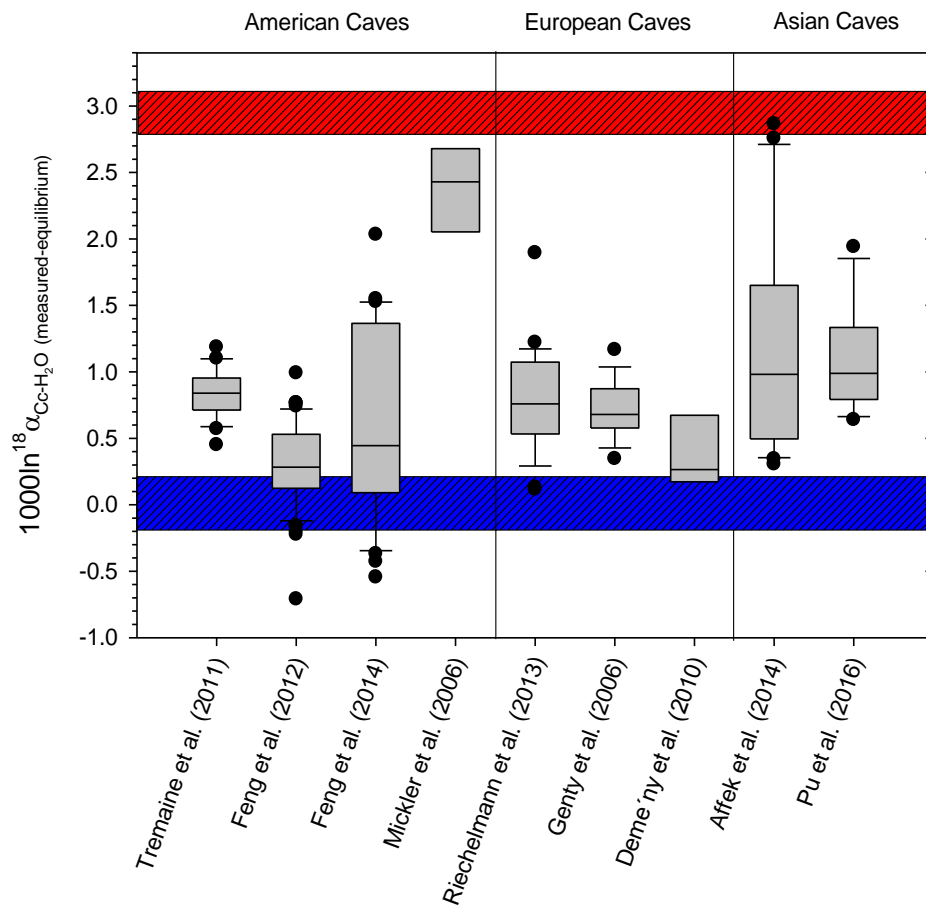


Fig. 2.14: A box plot showing differences between measured and equilibrium $1000\ln^{18}\alpha_{\text{Cc-H}_2\text{O}}$ from nine caves in America, Europe and Asia. The shaded area in blue shows the equilibrium $1000\ln^{18}\alpha_{\text{Cc-H}_2\text{O}}$ datum ($\pm 0.2 \text{ ‰}$; this study). The shaded area in red indicates the maximum predicted $1000\ln^{18}\alpha_{\text{Cc-H}_2\text{O}}$ value of $2.95 \pm 0.14 \text{ ‰}$, based upon equation (2.4).

2.11 Supplementary Materials

Table S1: Mineralogy from the XRD measurements of selected synthetic carbonate samples

Experiment ID	Watch glass	Duration (d)	Mineralogy
MIE-15-95-09-F	Upper	14	Calcite (100 %)
MIE-15-95-09-F	Lower	14	Calcite (100 %)
MIE-15-95-10-I	Upper	15	Calcite (100 %)
MIE-15-95-10-I	Lower	15	Calcite (100 %)
MIE-15-95-11-S	Upper	15	Calcite (100 %)
MIE-15-95-11-S	Lower	15	Calcite (100 %)
MIE-25-95-07-F	Upper	7	Calcite (100 %)
MIE-25-95-07-F	Lower	7	Calcite (98.42 %), Vaterite (1.58 %)
MIE-25-95-08-I	Upper	7	Calcite (100 %)
MIE-25-95-08-I	Lower	7	Calcite (100 %)
MIE-25-95-09-S	Upper	7	Calcite (100 %)
MIE-25-95-09-S	Lower	7	Calcite (100 %)
MIE-32-95-02-F	Upper	5.7	Calcite (99.8 %), Aragonite (0.2 %)
MIE-32-95-02-F	Lower	5.7	Calcite (93.54 %), Vaterite (6.46 %)
MIE-32-95-03-I	Upper	5.8	Calcite (99.85 %), Beta Ca (HCOO) ₂ (0.15 %)
MIE-32-95-03-I	Lower	5.8	Calcite (96.71 %), Vaterite (3.29 %)
MIE-32-95-04-S	Upper	5.9	Calcite (100 %)
MIE-32-95-04-S	Lower	5.9	Calcite (100 %)

Table S2: DIC remaining fraction on the upper watch glasses from equation (2.2).

a (cm)	temp (°C)	α cm/s	t_{pr} (s)	Average exposure time (s)	DIC remaining					
					15 °C		25 °C		32 °C	
					mmol/L	%	mmol/L	%	mmol/L	%
0.008	15	0.0000202	396.04	60	3.55	0.91	3.40	0.82	3.08	0.74
0.008	25	0.0000402	199.00	125	3.24	0.84	2.82	0.68	2.35	0.57
0.008	32	0.00005896	135.69	275	2.70	0.70	2.02	0.49	1.56	0.38

a : average thin film thickness (cm) flowing in the pyrx tube and on the upper watch glass

α : precipitation rate constant = $(0.52 + 0.4 T + 0.004 T^2) * 10^{-5}$; T is temperature in celsius

Average Exposure(s): is a sum of the flow time of water in the pyrx tube plus 1/2 drip interval

Reason for using average exposure time (s) to calculate the remaining DIC in the Rayleigh model is that the enrichment in C-13 and O-18 in the calcite precipitate on the upper watch glass is the sum of the total enrichment of C-13 and O-18 in DIC along the pyrx tube plus the average enrichment in these isotopes on the upper watch glass (see Fig. 2.1)

Chapter 3 - Speleothem evidence for the greening of the Sahara and its implications for the early human dispersal out of Africa

Mohammed I. EL-Shenawy^{a,b,1}, Sang-Tae Kim^a, Henry P. Schwarcz^a, Yemane Asmerom^c and Victor J. Polyak^c

^aSchool of Geography and Earth Sciences, McMaster University, Hamilton, ON, L8S 4K1, Canada.

^bDepartment of Geology, Beni Suef University, Beni Suef, 62111, Egypt.

^cDepartment of Earth and Planetary Sciences, University of New Mexico, Albuquerque, NM, 87131, USA.

To be submitted to *Quaternary Science Reviews*

3.1 Abstract

Although there is a consensus that there were wet periods (greening events) in the Sahara in the past, the spatial extent and the timing of these greening events are still in dispute, yet critical to our understanding of the early human dispersal out of Africa. Our U-series dates of speleothems from the Northeastern Sahara (Wadi Sannur cave, Egypt) reveal that the periods of speleothem growth were brief and restricted to the interglacial Marine Isotope Stages MIS 5.5, MIS 7.3, and the early MIS 9 with a remarkable absence of the Holocene deposition. These growth periods of Wadi Sannur cave speleothems correspond to periods of high rainfall (green Sahara). Distinct low $\delta^{18}\text{O}$ values of speleothems indicate a distal moisture source that we interpret to be the Atlantic Ocean. These two lines of geochemical evidence from the Wadi Sannur speleothems thus suggest that maximal northward shifts in the West African monsoon system occurred during the growth periods of the speleothems, leading to full greening of the Sahara, facilitating human migration into Eurasia. The two latest periods of speleothem growth at Wadi Sannur are contemporaneous with two important archeological events to the north in Levant: the sharp technological break between the Acheulo-Yabrudian and the Mousterian industries, and the arrival of *Homo sapiens*, indicating a key role of the Sahara route in early human dispersal out of Africa.

3.2 Introduction

The Sahara desert is one of the warmest and driest places on Earth today. However, a wealth of marine and surface continental archives suggests that the Sahara had been periodically transformed to a green landscape (green Sahara) in the past (e.g., Castañeda et al., 2009; Kuper and Kröpelin, 2006; Larrasoana et al., 2003). While a dry Sahara would have been a human migration barrier, a green Sahara could have been habitable, facilitating the migration of early humans out of Africa (Drake et al., 2011; Scerri et al., 2014). Palynological investigation of marine sediments offshore from northwestern Africa showed that the spatial extension of the greening events in the Sahara was restricted to latitude 23°N in the last 250 ka (Hooghiemstra et al., 2006), while lacustrine sediments from northeast Africa indicate the existence of paleolakes at 25°N within the same period (Kieniewicz and Smith, 2009; Schwarcz and Morawska 1993). Paleolakes define an uninterrupted humid corridor that extended between latitudes 21°N to 30°N in the central Sahara during MIS 5 (Osborne et al., 2008). Although lacustrine remnants provide excellent records of wetter periods in the past, their records in most cases are partly lost as a result of erosional processes (de Menocal, 2013). Consequently, the past climate of the Sahara has not been well understood both spatially and temporally.

Speleothems are terrestrial carbonate deposits, formed in caves, isolated from various surface weathering processes. The formation of dripstone and flowstone speleothems such as stalagmites is a function of water and vegetation availability. Rainfall water is a carrier for the soluble calcium carbonate, which is originally leached from the host rock and made available primarily by the CO₂ respiration of plants in soils (Ford and Williams,

2007). In arid regions, such as the Sahara, the absence of water and/or vegetation terminates speleothem growth (Vaks et al., 2010). Therefore, speleothem growth in the Sahara is a powerful proxy for the greening of the Sahara and consequently its human accessibility. The periods of speleothem growth can be dated by U-Th method back to 500,000 years (Cheng et al., 2016; Vaks et al., 2013). Moreover, the oxygen isotope composition of speleothem carbonates is an invaluable geochemical tracer for their moisture source (Asmerom et al., 2010).

A double stalagmite, sample WS-5d, was collected from Wadi Sannur cave (28° 37' N and 31° 17' E, 200 m above sea level; Fig. 3.1) in central Egypt. This cave is best suited for the assessment of greening of the Sahara and its implication for early human migration out of Africa for two reasons: (a) presently, the cave has no active dripping sites and no vegetation cover above it. However, the existence of the surface karst profile and the terra-rossa residue in the fractures above the cave indicates intensive paleorainfall and paleovegetation in the area; (b) The Wadi Sannur cave region of the Sahara is the gateway to the Sinai triangle, hindering (during arid intervals) or facilitating (during wet periods) human migration out of Africa.

3.3 Analytical Methods

U-series isotope measurements were made at the Radiogenic Isotope Laboratory, University of New Mexico. Subsample powders (80-290 mg) were milled out and completely dissolved in concentrated nitric acid and spiked with a mixed ^{229}Th - ^{233}U - ^{236}U spike. U and Th were separated using conventional anion-exchange chromatography.

Isotope ratio measurements were made with a Thermo Neptune plus multicollector inductively coupled plasma mass spectrometer (MC-ICPMS). The MC-ICPMS measurements were run in static mode using a mix of 10^{10} , 10^{11} and 10^{12} Ω resistors in conjunction with Faraday cup detectors and an ion-counting secondary electron multiplier detector. NBL-112A U isotope standard was measured with the samples, obtaining the published $\delta^{234}\text{U}$ value of -38.0 (Cheng et al., 2013). The analytical uncertainties are 2σ of the mean. The corrected age uncertainties include analytical errors and uncertainties in the initial $^{230}\text{Th}/^{232}\text{Th}$ ratios, where an initial $^{230}\text{Th}/^{232}\text{Th}$ atomic ratio of 4.4 ± 2.2 ppm was used in the age calculations. ^{234}U and ^{230}Th decay constants were taken from Cheng et al. (2013). The oxygen isotope analyses were conducted by the McMaster Research Group for Stable Isotopologues (MRSI) at McMaster University. The WS-5d stalagmite was sampled at 5 mm interval along the growth axis of the large stalagmite. The collected carbonate samples were analyzed with an automated carbonate device at 90°C for their $\delta^{18}\text{O}$ value using an OPTIMA gas source stable isotope ratio mass spectrometer. Reported $\delta^{18}\text{O}$ values were normalized to the recommended values for two isotopic reference materials NBS 18 and NBS 19. Long-term internal precision of these reference materials is better than 0.08 ‰. All oxygen isotope compositions are reported in standard δ notation on the VPDB scale.

3.4 Timing of speleothem growth in the Wadi Sannur cave

The chronology of double stalagmite WS-5d is based on a total of 18 U-Th dates (Table 3.1). Fourteen dates were determined on the larger part of the double stalagmite

and the other four dates on the smaller branch (Fig. 3.2). Dating profiles along the growth axes of the large and small stalagmites show that both of them grew during three discrete phases corresponding to interglacials MIS 5.5, MIS 7.3 and MIS 9 with a remarkable absence of deposition during the Holocene (Fig. 3.3). Age reversals exist in the two oldest growth phases of the large stalagmite (e.g., Burns et al., 2001; Fleitmann et al., 2011) that might be caused by the migration of U into/out of the stalagmite, possibly due to immersion in water during subsequent wet episodes. However, the overall chronology of the large stalagmite was confirmed by its replication along the growth axis of the small stalagmite (Fig. 3.2).

The youngest period of stalagmite WS-5d growth in the Wadi Sannur cave occurred in a brief interval between 129.82 ± 0.64 and 127.98 ± 0.45 ka BP. The duration of this interval ranged from 600 to 3000 years (1840 ± 1090 years) as inferred from uncertainties in the U-Th dates (Supplementary Materials, Fig. S1). The age reversals and the possibility of brief speleothem growth in the two oldest phases of stalagmite WS-5d prohibit resolving their growth duration. Therefore, we estimated the timing of these periods by calculating the weighted mean age for each phase, accounting for both analytical and systematic (i.e., possible U mobilization) uncertainties. The weighted mean age calculation includes all the measured ages from each phase without rejecting any age data (Ludwig, 2003). Consequently, the weighted mean ages ($\pm 2\sigma$) of the two oldest periods of speleothem growth are 219.4 ± 7.3 ka BP and 335 ± 12 ka BP, respectively.

The timing of the three growth phases in stalagmite WS-5d coincides with the occurrence of three well-defined sapropels in the Mediterranean Sea (i.e., S10, S8, and

S5; Fig. 3.3) (Ziegler et al., 2010), suggesting a coherent relationship between the North African Monsoon and Wadi Sannur cave speleothem growth. The time span for stalagmite WS-5d growth also coincides with the periods of speleothem growth in the neighboring caves in central and southern Negev desert (Vaks et al., 2010). This agreement indicates that greening extended widely over the area between 28°N and 30°N latitudes during MIS 9, MIS 7.3, and MIS 5.5 (Fig. 3.1, 3.3). The absence of speleothem deposition during the Holocene in both regions suggests that regional long-term aridity or insufficient humidity for speleothem growth persisted continuously since MIS 5.5. During MIS 5.5, two rainfall balanced-paleolakes (at Dakhleh and Bir Tarfawi) existed south of Wadi Sannur cave at the latitudinal belt between latitudes 22°N and 25°N in the Northeast Sahara (Kieniewicz and Smith, 2009; Schwarcz and Morawska 1993). In contrast, Lisan, Samra, and Amora lakes in the Levant, north of the Negev desert, exhibited lower water levels than those in glacial MIS 6 period (Frumkin et al., 2011; Kiro et al., 2015; Torfstein et al., 2015, 2009). Further south in the Arabian Peninsula, four major discrete intervals of speleothem deposition have been reported in Mukalla and Hoti caves, which cover the area between 15°N and 23°N latitudes. These four intervals correspond to MIS 9, MIS 7, MIS 5, and MIS 1 (Burns et al., 2001; Fleitmann et al., 2011). The oldest three intervals of speleothem deposition in southern Arabia are in good agreement with the speleothem growth chronology in the Wadi Sannur and Negev desert caves (Fig. 3.3, S2). Recently, Rosenberg et al. (2013) reported humid periods in Nafud desert, northern Arabia (28°N), that are synchronous to those in the Wadi Sannur and Negev desert caves based upon luminescence dating of paleolake deposits.

Climate modelling and field studies have estimated a rainfall amount of ≥ 400 mm/yr to maintain the existence of the Dakhla and Bir Tarfawi paleolakes during MIS 5.5 (Kieniewicz and Smith, 2009; Wendorf et al., 1993), whereas speleothem records in the northern Sahara and the Negev deserts indicate sufficient rainfall for speleothem growth, but not enough for maintaining the Levantine lakes at levels comparable to their levels during glacial isotope stages (Torfstein et al., 2015; Vaks et al., 2010). The rainfall amount required to trigger speleothem growth in the Levant and Arabia has been shown to range between 100 to 300 mm/yr (Bar-Matthews et al., 2003; Fleitmann et al., 2011; Frumkin et al., 2011). Therefore, we suggest that humidity decreased along a South-North transect during the periods of speleothem growth in the Sahara and Arabia, fueled by a southern moisture source (Fig. 3.1). This suggestion is opposite to the northern moisture source (i.e., the Mediterranean Sea), which was proposed by Vaks et al. (2010).

3.5 Source of paleorainfall and its driving mechanism

To identify the source of moisture above the Wadi Sannur cave in the past, we determined oxygen isotope compositions of stalagmite WS-5d and then compared them with those from other modern and ancient carbonate deposits from the Northeast Sahara and Levant (Fig. 3.3). We assume that temperature differences between interglacial stages have a smaller effect on the $\delta^{18}\text{O}$ value of calcitic stalagmite formed than changes in the $\delta^{18}\text{O}$ value of source water, because a 4 °C change in temperature can only shift $\delta^{18}\text{O}$ value of calcite by 1 ‰ (Kim and O'Neil, 1997). This assumption is in agreement with the similarity in paleotemperature between the Holocene and MIS 5 ($\pm 1^\circ\text{C}$) that is

estimated based upon fluid inclusions in Soreq cave speleothems (McGarry et al., 2004). The stalagmite WS-5d has an average $\delta^{18}\text{O}$ value of -11.6 ± 0.8 ‰ relative to VPDB ($n = 72$; Table S1). Other synchronous carbonates from Dajara cave and Kurkur area in the Northeast Sahara possess near-identical oxygen isotope composition of -12.1 ± 0.9 ‰ ($n = 18$) and -12.0 ± 1.7 ‰ ($n = 14$) VPDB respectively (Brook et al., 2002; Crombie et al., 1997). These $\delta^{18}\text{O}$ values from multiple northeastern Sahara speleothems indicate the presence of a single moisture source. Moreover, the mean $\delta^{18}\text{O}$ value of speleothems to the north of our study area in the Negev desert (-10.5 ± 0.4 ‰ VPDB; $n = 25$) (Vaks et al., 2010) also lie within the range of the $\delta^{18}\text{O}$ pool (between -9.2 ‰ and -13.8 ‰) for the northeastern Sahara carbonates, suggesting a similar moisture source (Fig. 3.4).

Two main sources for the rainfall above the Northeast Sahara and Negev desert have been proposed: (1) the Mediterranean Sea via the Mediterranean cyclones and (2) the Atlantic Ocean through either the West African Monsoon or the Westerlies (Crombie et al., 1997; Sultan et al., 1997; Vaks et al., 2010). Modern and late Holocene speleothems from Soreq cave in Levant, inferred to have formed from Mediterranean-derived rainfall, have $\delta^{18}\text{O}$ values of -5.3 ± 0.6 ‰ VPDB (Affek et al., 2014; Bar-Matthews et al., 2003; Frumkin et al., 1999), which are about 5 to 7 ‰ higher than the $\delta^{18}\text{O}$ of the carbonate in the Northeast Sahara and Negev desert. Therefore, the low $\delta^{18}\text{O}$ value of Wadi Sannur carbonates, relative to modern Mediterranean-derived values, indicates a more distal moisture source, although some depletion of Mediterranean's rain in ^{18}O could have occurred as storms migrated southwards during intensive rainfall events. However, instrumental rainfall observations and hydroclimate history, as revealed by lake levels in

central Levant, show that the central Levant had experienced intensive rainfall, more than normal, during the glacial (cold) periods and less intensive rain during the interglacial periods (Frumkin et al., 2011; Kiro et al., 2015; Kushnir and Stein, 2010; Torfstein et al., 2015, 2009), ruling out the Mediterranean as the source of the interglacial discrete carbonates in the Northeast Sahara and Negev desert.

We suggest that humid Atlantic air masses travelling long distances over Africa became depleted in ^{18}O due to the continental effect, resulting in rainfall $\delta^{18}\text{O}$ values as low as -11 to -12 ‰ (VSMOW) when these air masses reach the Northeast Sahara and Negev desert (Rozanski et al., 1992). This is supported by the progressive depletion of deuterium (^2H) and ^{18}O in the Saharan groundwater along a West-East transect (Sonntag et al., 1978). Mechanisms for bringing rainfall of an Atlantic Ocean origin to the Northeast Sahara are via either the Westerlies or the West African Monsoon (Fig. 3.1). The position of the Westerlies has been shown to vary with global temperature (Toggweiler and Russell, 2008). During glacial (cold) periods, the Westerlies become weaker and shift toward the equator; conversely, during interglacial periods, the Westerlies are stronger and forced toward the poles (Asmerom et al., 2010; Blome et al., 2012). Westerlies would most likely provide moisture to the Northeast Sahara and Negev desert during glacial periods, contrary to what we observe. Speleothem growth in the Wadi Sannur cave coincides with high summer insolation and high greenhouse gas (e.g., CO_2 and CH_4) concentrations in the atmosphere during the MIS 9, MIS 7.3, and MIS 5.5, which lead us to attribute the rainfall driven mechanism to the West African Monsoon system (Fig. 3.1). Threshold values of 506 W/m^2 and 286 ppm for summer insolation and

CO₂ concentration are required to expand the West African Monsoon far north to trigger speleothem growth in the Wadi Sannur and Negev caves during MIS 9 and MIS 5.5 (Laskar et al., 2004; Lüthi et al., 2008). During MIS 7.3, the highest summer insolation for the last 500 ka seems to have compensated for the relatively lower CO₂ concentration in this period compared to that of MIS 9 and MIS 5.5 (Fig. S3a, b, c). These observations are supported by recent modeling experiments that demonstrate the northward shifting of the West African monsoon system in response to high summer insolation and increasing greenhouse gas concentrations during the last deglaciation (Otto-bliesner et al., 2012). However, during the last deglaciation, the summer insolation was lower compared to other interglacials, potentially explaining the absence of rainfall and thus absence of speleothem growth at Sannur and Negev caves during the Holocene (Fig. S3d).

The Atlantic-monsoonal origin of paleorainfall above the Wadi Sannur and Negev desert caves is also supported by other paleoclimate records:

- I. The dominance of megalake conditions in the Chad and Fazzan Basins in the Sahara desert at 125 and 130 ka respectively (Drake et al., 2011, Gaven et al., 1981).
- II. The existence of a paleoriver of limited–evaporation in the Central Sahara, extending from latitudes 21°N to 30°N during the MIS 5.5 (Osborne et al., 2008; Rohling et al., 2002). The Nd isotope signature in marine sediments offshore of Libya clearly points to basaltic bedrock sources upstream of this paleoriver at latitude 21°N (Osborne et al., 2008), while its limited–evaporation nature was inferred from the distinctively light oxygen isotope anomaly

observed in planktic foraminifera from Mediterranean cores (Rohling et al., 2002).

- III. The formation of paleolakes in the Nafud desert that is inferred to be discharged by long travelling rains across Africa to North Arabia via the African Monsoon system (Rosenberg et al., 2013).
- IV. Surprisingly, the two lowest $\delta^{18}\text{O}$ peaks in the speleothem records from central Levant (Bar-Matthews et al., 2003; Frumkin et al., 1999) are synchronous with the last two speleothem growth periods in the Sahara and Negev deserts. These $\delta^{18}\text{O}$ minima could be accounted for by a mixture of approximately equal amount of Atlantic-monsoonal and Mediterranean Sea rains (Fig. 3.4). This observation supports the far north extent of the African Monsoon rainfall to the central Levant during MIS 5.5 as suggested by Torfstein et al. (2015). Moreover, the mixture of these two moisture sources potentially explains the decreasing of the layer thickness in speleothems along the North-South transect of the Negev desert. Our new interpretation of the $\delta^{18}\text{O}$ values of speleothems from Soreq cave suggests that the Levant was a transitional climate zone in the past; although it received less than normal amount of rainfall in winter during interglacial (warm) periods, it was still influenced by summer monsoonal rainfall.

The west to southwest rainfall source and the timing patterns of speleothem growth matched by lake records from Sahara, Arabia and Levant would indicate that, during early MIS 9, MIS 7.3, and MIS 5.5, the North Sahara lay approximately between the 400

mm isohyet at 23°N and 200 mm isohyet at 30 °N. This rainfall zone would be sufficient to activate the dense network of paleo-rivers and channels in the Sahara (Drake et al., 2011; Scerri et al., 2014), facilitating the full greening of the Sahara. A Holocene greening event is also inferred from pollen analysis of continental sediment cores in the Sahara at 22°N (Schulz, 1991) with annual rainfall ranging from 250 to 300 mm, which was apparently enough to support the growth of speleothems in Hoti cave in Arabia at 23°N (Burns et al., 2001), but was not enough to rejuvenate the Bir Tarfawi and Dakhla lakes and/or to reinitiate speleothem deposition at Wadi Sannur cave (Kieniewicz and Smith, 2009; Wendorf et al., 1993).

3.6 The green Sahara and the early human dispersal out of Africa

Water and vegetation are vital resources for early humans. Timing of stalagmite WS-5d growth at Wadi Sannur cave suggests the existence of these two key resources at a critical human migration location during three periods of widespread rainfall in the Sahara centered at 335 ± 12 ka, 219.4 ± 7.3 ka, and 128.5 ± 1.1 ka. These brief wet periods indicated by Wadi Sannur cave speleothem growth are critical periods when the dry Sahara did not pose as an inhabitable barrier, and during which human dispersal out of Africa could have occurred. Similar events undoubtedly would have occurred further into the past. The last of these greening periods appears to have only lasted for 600 to 3000 years. This was long enough, however, to allow early modern humans to cross the whole Sahara based upon the estimated rates of early human expansion of 5-11 km/yr (Hamilton and Buchanan, 2007; Hazelwood and Steele, 2004). If the evidence from lake

records in the presently hyper-arid Sahara is also considered, the zone of increased rainfall would resemble the present wooded grassland zone at the African equator (Good and Caylor, 2011), explaining the wide spread of archeological sites dating from MIS 5 as well as earlier periods of greening in the North Sahara (Stringer and Barton, 2008).

The latest speleothem growth period in Wadi Sannur cave at 128.5 ± 1.1 ka is contemporaneous with the archeological presence of Early Modern Human (i.e., *Homo sapiens*) in the Levant, which has a time range of 130 to 100 ka (Grün et al., 2005). Moreover, the concurrent greening conditions in the Sahara and Arabia during MIS 5.5 obviate the need of a southern route crossing the Red Sea (Armitage et al., 2011).

The middle speleothem growth period in Wadi Sannur cave (219.4 ± 7.3 ka) coincides with a sharp technological break between the Acheulo-Yabrudian and the Mousterian industries observed at Misliya cave in the Levant at 244 ± 30 ka (Valladas et al., 2013). This sharp technological break may have involved a change in human populations (Bar-Yosef, 1998). The speleothem growth record in the Sahara and the archeological evidence from the Levant assign a high credibility to the Sinai land bridge as a link between the green Sahara and the Levant in the past. However, as shown in Fig. 3.3, the absence of speleothem growth in Wadi Sannur cave after MIS 5.5 suggests that subsequent aridity in the Northern part of the Sahara made the Sinai land bridge an ineffective route for later human dispersal waves out of Africa (e.g., MIS 4; Hershkovitz et al., 2015).

3.7 Conclusion

The growth timing of the Wadi Sannur stalagmites, along with other paleoclimate data from North Africa, indicates that the African Monsoon system has covered the entire Sahara desert three times in the past 350 ka, promoting the full greening of the Sahara. The two latest green episodes in the Sahara were associated with two important archeological events in the Levant: the arrival of *Homo sapiens* and the sharp technological break between the Acheulo-Yabrudian and the Mousterian industries, supporting the view of the key role of the Sahara as a gateway for human dispersal (Derricourt, 2005).

3.8 Acknowledgements

The authors thank Yasser Salama and Rabea Ali for their help during the field work and Martin Knyf for laboratory assistance and discussion. M.I. EL-Shenawy is thankful for the Farouk EL-Baz student research grant (2013) for desert research. This research was supported by NSERC Discovery Grant Program (386188-2010) to S.-T. Kim.

3.9 References

- Affek, H.P., Matthews, A., Ayalon, A., Bar-Matthews, M., Burstyn, Y., Zaarur, S., Zilberman, T., 2014. Accounting for kinetic isotope effects in Soreq Cave (Israel) speleothems. *Geochim. Cosmochim. Acta* 143, 303–318.
- Armitage, S.J., Jasim, S. A, Marks, A.E., Parker, A.G., Usik, V.I., Uerpmann, H.-P., 2011. The Southern Route “Out of Africa”: Evidence for an Early Expansion of Modern Humans into Arabia. *Science* 453, 453–156.
- Asmerom, Y., Polyak, V.J., Burns, S.J., 2010. Variable winter moisture in the southwestern United States linked to rapid glacial climate shifts. *Nat. Geosci.* 3, 114–117.
- Bar-Matthews, M., Ayalon, A., Gilmour, M., Matthews, A., Hawkesworth, C.J., 2003. Sea-land oxygen isotopic relationships from planktonic foraminifera and speleothemes on the Eastern Mediterranean region and their implications for paleorainfall during interglacial intervals. *Geochim. Cosmochim. Acta* 67, 3181–3199.
- Bar-Yosef, O., 1998. The chronology of the Middle Palaeolithic of the Levant. In: Akazawa, T., Aoki, K., Bar-Yosef, O. (Eds.), *Neandertals and Modern Humans in Western Asia*. Plenum Press, New York, pp. 39–56.
- Blome, M.W., Cohen, A.S., Tryon, C. a., Brooks, A.S., Russell, J., 2012. The environmental context for the origins of modern human diversity: A synthesis of regional variability in African climate 150,000-30,000 years ago. *J. Hum. Evol.* 62, 563–592.
- Brook, G.A., Embabi, N.S., Ashour, M.M., Edwards, R.L., Cheng, H., Cowart, J.B., Dabous, A.A., 2002. Djara cave in the Western desert of Egypt: morphology and evidence of Quaternary climatic change: *Cave and Karst Science* 29, 57–66.
- Burns, S.J., Fleitmann, D., Matter, A., Neff, U., Mangini, A., 2001. Speleothem evidence from Oman for continental pluvial events during interglacial periods. *Geology* 29, 623–626.
- Castañeda, I.S., Mulitza, S., Schefuss, E., Lopes dos Santos, R. a, Sinninghe Damsté, J.S., Schouten, S., 2009. Wet phases in the Sahara/Sahel region and human migration patterns in North Africa. *Proc. Natl. Acad. Sci. U. S. A.* 106, 20159–20163.
- Cheng, H., Lawrence Edwards, R., Shen, C.C., Polyak, V.J., Asmerom, Y., Woodhead, J., Hellstrom, J., Wang, Y., Kong, X., Spötl, C., Wang, X., Calvin Alexander, E., 2013.

Improvements in ^{230}Th dating, ^{230}Th and ^{234}U half-life values, and U-Th isotopic measurements by multi-collector inductively coupled plasma mass spectrometry. *Earth Planet. Sci. Lett.* 371-372, 82–91.

Cheng, H., Edwards, R.L., Sinha, A., Spötl, C., Yi, L., Chen, S., Kelly, M., Kathayat, G., Wang, X., Li, X., Kong, X., Wang, Y., Ning, Y., Zhang, H., 2016. The Asian monsoon over the past 640,000 years and ice age terminations. *Nature* 534, 640–646.

Crombie, M. K., Arvidson, R. E., Struchio, N. C., El Alfy, Z., Abu Zied, K., 1997. Age and isotopic constraints on Pleistocene episodes in the Western Desert, Egypt. *Palaeogeogr. Palaeoclimatol. Palaeoecol.* 130, 337–355.

De Menocal, P.B., 2013. Marine Sediment Records of African Climate Change: Progress and Puzzles. *Treatise Geochemistry Second Ed.* 14, 99–108.

Derricourt, R., 2005. Getting “Out of Africa”: Sea crossings, land crossings and culture in the Hominin migrations. *J. World Prehistory* 19, 119–132.

Drake, N. a, Blench, R.M., Armitage, S.J., Bristow, C.S., White, K.H., 2011. Ancient watercourses and biogeography of the Sahara explain the peopling of the desert. *Proc. Natl. Acad. Sci.* 108, 458–462.

Fleitmann, D., Burns, S.J., Pekala, M., Mangini, A., Al-Subbary, A., Al-Aowah, M., Kramers, J., Matter, A., 2011. Holocene and Pleistocene pluvial periods in Yemen, southern Arabia. *Quat. Sci. Rev.* 30, 783–787.

Ford, D., Williams, P.D., 2007. *Karst hydrogeology and geomorphology.* Wiley, Chichester.

Frumkin, A., Bar-Yosef, O., Schwarcz, H.P., 2011. Possible paleohydrologic and paleoclimatic effects on hominin migration and occupation of the Levantine Middle Paleolithic. *J. Hum. Evol.* 60, 437–451.

Frumkin, A., Ford, D.C., Schwarcz, H.P., 1999. Continental Oxygen Isotopic Record of the Last 170,000 Years in Jerusalem. *Quat. Res.* 51, 317–327.

Gaven, C., Hillaire-Marcel, C., Petit-Maire, N., 1981. A Pleistocene lacustrine episode insoutheastern Libya. *Nature* 290,131–133.

Good, S.P., Caylor, K.K., 2011. Climatological determinants of woody cover in Africa. *Proc. Natl. Acad. Sci. U. S. A.* 108, 4902–4907.

- Grün, R., Stringer, C., McDermott, F., Nathan, R., Porat, N., Robertson, S., Taylor, L., Mortimer, G., Eggins, S., McCulloch, M., 2005. U-series and ESR analyses of bones and teeth relating to the human burials from Skhul. *J. Hum. Evol.* 49, 316–334.
- Hamilton, M.J., Buchanan, B., 2007. Spatial gradients in Clovis-age radiocarbon dates across North America suggest rapid colonization from the north. *Proc. Natl. Acad. Sci. U. S. A.* 104, 15625–15630.
- Hazelwood, L., Steele, J., 2004. Spatial dynamics of human dispersals Constraints on modelling and archaeological validation. *J. Archaeol. Sci.* 31, 669–679.
- Hershkovitz, I., Marder, O., Ayalon, A., Bar-matthews, M., Yasur, G., Boaretto, E., Caracuta, V., Alex, B., Frumkin, A., Goder-goldberger, M., Gunz, P., Holloway, R.L., Latimer, B., Lavi, R., Matthews, A., Slon, V., Mayer, D.B., Berna, F., Bar-oz, G., 2015. Levantine cranium from Manot Cave (Israel) foreshadows the first European modern humans. *Nature* 520, 216–219.
- Hooghiemstra, H., Lézine, A.M., Leroy, S. a G., Dupont, L., Marret, F., 2006. Late Quaternary palynology in marine sediments: A synthesis of the understanding of pollen distribution patterns in the NW African setting. *Quat. Int.* 148, 29–44.
- Kieniewicz, J.M., Smith, J.R., 2009. Paleoenvironmental reconstruction and water balance of a mid-Pleistocene pluvial lake, Dakhleh Oasis, Egypt. *Bull. Geol. Soc. Am.* 121, 1154–1171.
- Kim, S.-T., O’Neil, J., 1997. Equilibrium and nonequilibrium oxygen isotope effects in synthetic carbonates. *Geochim. Cosmochim. Acta* 61, 3461–3475.
- Kiro, Y., Goldstein, S.L., Lazar, B., Stein, M., 2015. Environmental implications of salt facies in the Dead Sea. *Geol. Soc. Am. Bull.* in press, 1–18. doi: 10.1130/B31357.1
- Kuper, R., Kröpelin, S., 2006. Climate-controlled Holocene occupation in the Sahara: motor of Africa’s evolution. *Science* 313, 803–807.
- Kushnir, Y., Stein, M., 2010. North Atlantic influence on 19th-20th century rainfall in the Dead Sea watershed, teleconnections with the Sahel, and implication for Holocene climate fluctuations. *Quat. Sci. Rev.* 29, 3843–3860.
- Larrasoana, J.C., Roberts, a. P., Rohling, E.J., Winklhofer, M., Wehausen, R., 2003. Three million years of monsoon variability over the northern Sahara. *Clim. Dyn.* 21, 689–698.

- Laskar, J., Robutel, P., Joutel, F., Gastineau, M., Correia, a. C.M., Levrard, B., 2004. A long-term numerical solution for the insolation quantities of the Earth . *Astron. Astrophys.* 428, 261–285.
- Ludwig, K.R., 2003. User's manual for Isoplot 3.0: A geochronological toolkit for Microsoft Excel. Berkeley Geochronology Center Special Publication, Berkeley, California, 4, 1–71.
- Lüthi, D., Le Floch, M., Bereiter, B., Blunier, T., Barnola, J.-M., Siegenthaler, U., Raynaud, D., Jouzel, J., Fischer, H., Kawamura, K., Stocker, T.F., 2008. High-resolution carbon dioxide concentration record 650,000-800,000 years before present. *Nature* 453, 379–382.
- McGarry, S., Bar-Matthews, M., Matthews, A., Vaks, A., Schilman, B., Ayalon, A., 2004. Constraints on hydrological and paleotemperature variations in the Eastern Mediterranean region in the last 140ka given by the δD values of speleothem fluid inclusions. *Quat. Sci. Rev.* 23, 919–934.
- Osborne, A.H., Vance, D., Rohling, E.J., Barton, N., Rogerson, M., Fello, N., 2008. A humid corridor across the Sahara for the migration of early modern humans out of Africa 120,000 years ago. *Proc. Natl. Acad. Sci.* 105, 16444–16447.
- Otto-bliesner, B.L., Russell, J.M., Clark, P.U., Liu, Z., Overpeck, J.T., Konecky, B., Nicholson, S.E., He, F., Lu, Z., 2012. Coherent changes of southeastern equatorial and northern African rainfall during the last deglaciation. *Science* 346, 1223–1227.
- Rohling, E.J., Cane, T.R., Cooke, S., Sprovieri, M., Bouloubassi, I., Emeis, K.C., Schiebel, R., Kroon, D., Jorissen, F.J., Lorre, a., Kemp, a. E.S., 2002. African monsoon variability during the previous interglacial maximum. *Earth Planet. Sci. Lett.* 202, 61–75.
- Rosenberg, T.M., Preusser, F., Risberg, J., Pliikk, A., Kadi, K. a., Matter, A., Fleitmann, D., 2013. Middle and Late Pleistocene humid periods recorded in palaeolake deposits of the Nafud desert, Saudi Arabia. *Quat. Sci. Rev.* 70, 109–123.
- Scerri, E.M.L., Drake, N. A., Jennings, R., Groucutt, H.S., 2014. Earliest evidence for the structure of *Homo sapiens* populations in Africa. *Quat. Sci. Rev.* 101, 207–216.
- Schulz, E., 1991. Holocene environments in the central Sahara. *Hydrobiologia* 214, 359–365.
- Schwarcz, H., Morawska, L., 1993. Uranium-series dating of carbonates from Bir Tarfawi and Bir Sahara East. In: Wendorf, F., Schild, R., Close, A. (Eds.), *Egypt During the Last Interglacial*. Plenum Press, New York, pp. 205–217.

- Stringer, C.B., Barton, N., 2008. Putting North Africa on the Map of Modern Human Origins. *Evol. Anthropol.* 17, 5–7.
- Sultan, M., Sturchio, N., Hassan, F. A., Hamdan, M. A. R., Mahmood, A. M., El Alfy, Z., Stein, T., 1997. Precipitation Source Inferred from Stable Isotopic Composition of Pleistocene Groundwater and Carbonate Deposits in the Western Desert of Egypt. *Quat. Res.* 48, 29–37.
- Toggweiler, J.R., Russell, J., 2008. Ocean circulation in a warming climate. *Nature* 451, 286–288.
- Torfstein, A., Goldstein, S.L., Kushnir, Y., Enzel, Y., Haug, G., Stein, M., 2015. Dead Sea drawdown and monsoonal impacts in the Levant during the last interglacial. *Earth Planet. Sci. Lett.* 412, 235–244.
- Torfstein, A., Haase-Schramm, A., Waldmann, N., Kolodny, Y., Stein, M., 2009. U-series and oxygen isotope chronology of the mid-Pleistocene Lake Amora (Dead Sea basin). *Geochim. Cosmochim. Acta* 73, 2603–2630.
- Vaks, A., Gutareva, O.S., Breitenbach, S.F.M., Avirmed, E., Mason, a J., Thomas, A.L., Osinzev, A.V, Kononov, A.M., Henderson, G.M., 2013. Speleothems Reveal 500,000-Year History of Siberian Permafrost. *Science* 340, 183–186.
- Vaks, A., Bar-Matthews, M., Matthews, A., Ayalon, A., Frumkin, A., 2010. Middle-Late Quaternary paleoclimate of northern margins of the Saharan-Arabian Desert: Reconstruction from speleothems of Negev Desert, Israel. *Quat. Sci. Rev.* 29, 2647–2662.
- Valladas, H., Mercier, N., Hershkovitz, I., Zaidner, Y., Tsatskin, A., Yeshurun, R., Vialettes, L., Joron, J.L., Reyss, J.L., Weinstein-Evron, M., 2013. Dating the Lower to Middle Paleolithic transition in the Levant: A view from Misliya Cave, Mount Carmel, Israel. *J. Hum. Evol.* 65, 585–593.
- Wendorf, F., Schild, R., Close, A.E., 1993. *Egypt during the Last Interglacial: The Middle Paleolithic of Bir Tarfawi and Bir Sahara East.* Plenum Press, New York.
- Ziegler, M., Tuenter, E., Lourens, L.J., 2010. The precession phase of the boreal summer monsoon as viewed from the eastern Mediterranean (ODP Site 968). *Quat. Sci. Rev.* 29, 1481–1490.

3.10 Tables

Table 3.1: Uranium-series data for the WS-5d stalagmite from the Wadi Sannur cave, Egypt.

Distance from the stalagmite top (mm)	^{238}U (ng/g)	^{232}Th (pg/g)	$^{230}\text{Th}/^{232}\text{Th}$ activity ratio	$^{230}\text{Th}/^{238}\text{U}$ activity ratio	measured $\delta^{234}\text{U}$ (‰)	initial $\delta^{234}\text{U}$ (‰)	uncorrected age (yrs BP)	corrected age (yrs BP)
Larger of double stalagmite								
5	1659.1 ± 1.0	1574 ± 35	2243 ± 50	0.6962 ± 0.0010	6.7 ± 1.0	9.6 ± 1.4	128006 ± 450	127979 ± 450
40	2398.9 ± 1.3	12 ± 38	439157 ± 1404240	0.7051 ± 0.0008	12.7 ± 1.0	18.3 ± 1.5	129431 ± 403	129431 ± 403
53	1759.5 ± 1.7	223 ± 30	17418 ± 2364	0.7214 ± 0.0017	31.3 ± 1.0	45.1 ± 1.5	129822 ± 643	129818 ± 643
68	157.7 ± 0.1	13 ± 39	34925 ± 107918	0.9198 ± 0.0018	49.5 ± 1.1	91.9 ± 2.0	219204 ± 1605	219202 ± 1605
94	199.2 ± 0.2	2137 ± 32	287 ± 4	1.0069 ± 0.0016	118.5 ± 1.1	225.1 ± 2.3	227686 ± 1479	227431 ± 1481
134	212.9 ± 0.1	9 ± 51	66376 ± 364201	0.9497 ± 0.0015	83.7 ± 1.1	153.2 ± 2.1	214283 ± 1262	214282 ± 1262
142	287.9 ± 0.3	785 ± 49	1053 ± 66	0.9389 ± 0.0029	69.2 ± 1.3	127.8 ± 2.6	217575 ± 2292	217505 ± 2291
163	450.2 ± 0.3	55 ± 37	24849 ± 16628	0.9919 ± 0.0012	32.1 ± 1.0	81.3 ± 2.8	329492 ± 3677	329489 ± 3677
211	507.7 ± 0.4	64 ± 32	24056 ± 12242	0.9871 ± 0.0012	24.0 ± 1.0	63.0 ± 2.8	341508 ± 4319	341505 ± 4319
241	898.1 ± 0.6	41 ± 30	69397 ± 51349	1.0328 ± 0.0012	52.0 ± 1.1	146.0 ± 3.6	365922 ± 5094	365921 ± 5094
274	1931.1 ± 1.4	14 ± 31	448528 ± 991400	1.0766 ± 0.0013	88.0 ± 1.1	241.7 ± 4.4	358193 ± 4647	358193 ± 4647
308	3508.9 ± 2.1	419 ± 47	26783 ± 3011	1.0458 ± 0.0012	72.5 ± 1.1	186.4 ± 3.4	334875 ± 3689	334872 ± 3689
327	2554.0 ± 2.4	288 ± 36	27888 ± 3460	1.0296 ± 0.0014	67.2 ± 1.1	164.4 ± 3.1	317214 ± 3391	317212 ± 3391
338	2192.6 ± 1.8	85128 ± 58	82.1 ± 0.1	1.0431 ± 0.0014	68.6 ± 1.1	178.2 ± 3.5	339382 ± 4074	338420 ± 4067
Smaller of double stalagmite								
13	2056.2 ± 1.3	39 ± 30	114161 ± 88617	0.7000 ± 0.0008	11.7 ± 1.0	16.7 ± 1.5	127923 ± 406	127923 ± 406
44	1805.9 ± 1.2	488 ± 33	7962 ± 545	0.7033 ± 0.0012	15.4 ± 1.0	22.1 ± 1.5	128058 ± 503	128050 ± 503
83	259.4 ± 0.2	86546 ± 127	8.42 ± 0.02	0.9192 ± 0.0024	40.4 ± 1.0	74.5 ± 2.2	226548 ± 2169	217126 ± 5036
126	333.6 ± 0.2	37035 ± 53	27.57 ± 0.05	1.0014 ± 0.0012	39.1 ± 1.0	98.7 ± 2.8	330702 ± 3680	327722 ± 3877

All errors are absolute 2σ . Subsample powder sizes range from 90 to 160 mg. Initial $^{230}\text{Th}/^{232}\text{Th}$ atomic ratio used to correct ages is 0.0000044 (activity ratio = 0.8) ± 50%. Yrs BP = years before present, where present = AD 2014.

3.11 Figures

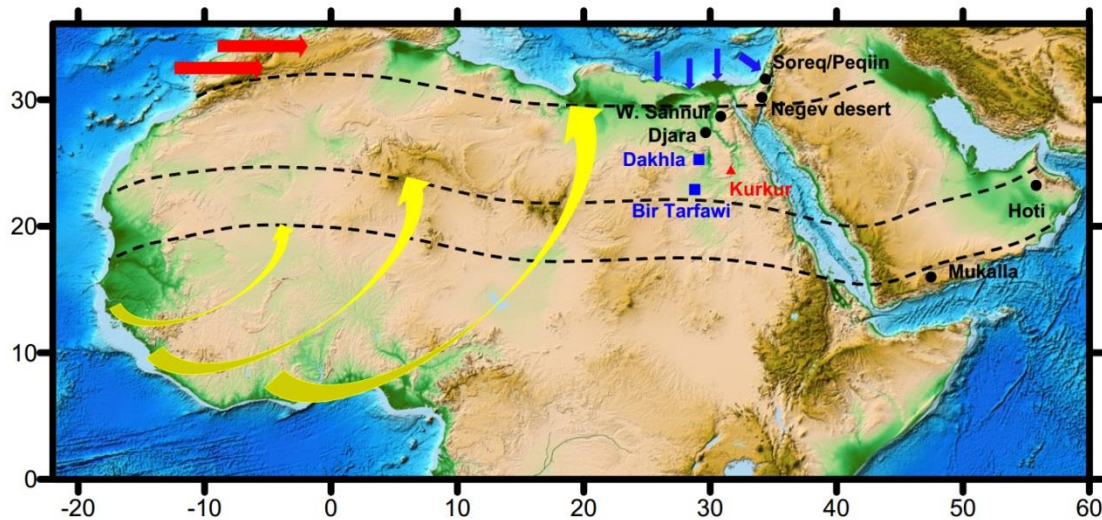


Fig. 3.1: Location map of caves, lakes and travertines used in this study. Black circles represent different cave locations; the two blue squares indicate the Northeastern Sahara paleolakes; and the red triangle show travertines in Kurkur site. Red and blue straight arrows indicate the trajectory of potential westerlies and Mediterranean rainfall, respectively. The yellow curved arrows define the Atlantic-humid air masses path during the boreal summer, whereas the dashed lines delineate the northern limit of this path (i.e., Inter Tropical Convergence Zone; ITCZ). The dashed lines from south to north are the ITCZ positions at present, Holocene, and during speleothem growth periods in the Wadi Sannur cave (i.e., MIS 9, 7.3, 5.5), respectively. Base relief map is taken from the NOAA website: <http://www.ngdc.noaa.gov/mgg/global/global.html>.

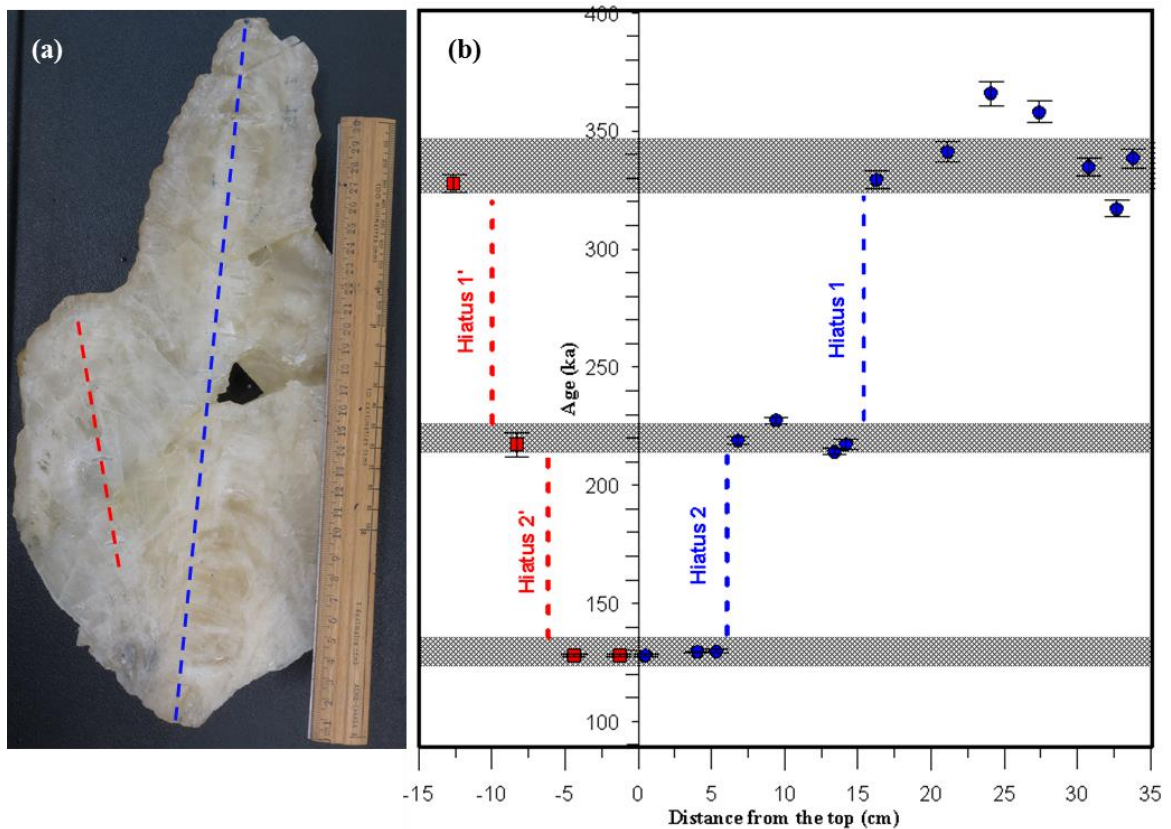


Fig. 3.2: (a) Longitudinal cross section in WS-5d double stalagmite. (b) U-Th-dates along the growth axis of the WS-5d stalagmite. Blue circles and positive depth values refer to the large stalagmite; red squares and negative depth values refer to the small stalagmite. Shaded horizontal bars indicate stalagmite growth intervals (i.e., weighted mean age $\pm 2\sigma$). Blue and red dashed vertical lines define two major growth hiatuses. U-Th dates lied outside of the weighted mean range are considered as outliers ($> 2\sigma$) and therefore excluded from their age cluster.

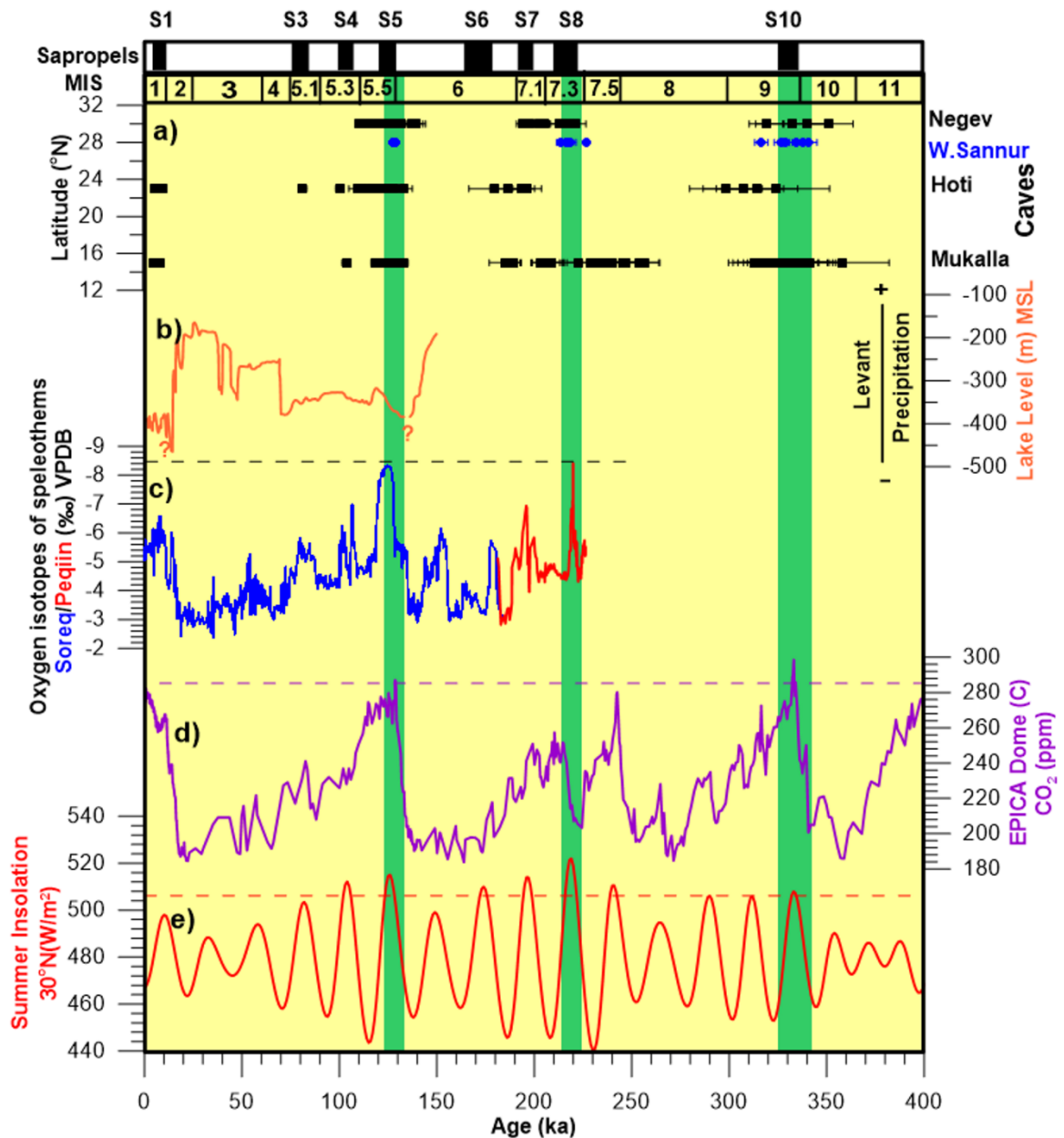


Fig. 3.3: Greening and drying periods in the Sahara over the last 350 ka. (a) Spatial and temporal speleothem growth patterns in the Sahara, Negev and Arabia deserts (this study, Vaks et al., 2010; Burns et al., 2001; Fleitmann et al., 2011). (b) Reconstructed lake levels in central Levant (Frumkin et al., 2011). (c) $\delta^{18}\text{O}$ of speleothems in Soreq (blue) and Peqiin (red) caves (Bar-Matthews et al., 2003); the black dashed line is the 50:50 source mixture line of the Northeastern Sahara and Modern/late Holocene Levant carbonates. (d) CO₂ concentrations as inferred from EPICA Dome C (Lüthi et al., 2008); the purple dashed line indicates the CO₂ threshold value discussed in this paper. (e) Summer insolation at 30°N (Laskar et al., 2004); the red dashed line shows the summer insolation

threshold magnitude discussed in this paper. Sapropel layer records from the
Mediterranean Sea are shown on the top of graph.

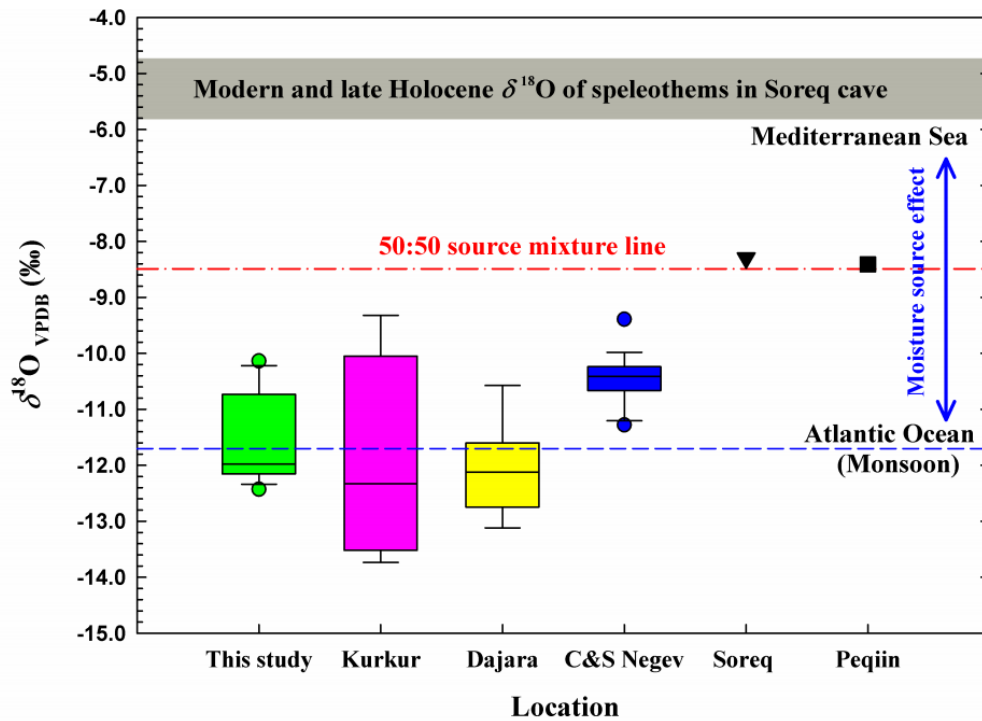


Fig. 3.4: Box plot of $\delta^{18}\text{O}$ value of carbonates in the Northeast Sahara desert, Central and Southern Negev desert, and Central Levant. The colored boxes, their whiskers and dots show 5th/95th percentiles of each data set. The black line in the box center marks the median value. The purple box shows $\delta^{18}\text{O}$ values in the Kurkur travertines (Crombie et al., 1997). The other three boxes present $\delta^{18}\text{O}$ values in speleothems from Wadi Sannur, Dajara, and central and the southern Negev desert caves during MIS 9, 7.3, 5.5 (Brook et al., 2002; Vaks et al., 2010). The black square is the minimum $\delta^{18}\text{O}$ value observed in the Peqiin cave record at MIS 7.3, whereas the triangle is the $\delta^{18}\text{O}$ minimum in the Soreq cave record during MIS 5.5 (Bar-Matthews et al., 2003). The grey horizontal bar shows the range of $\delta^{18}\text{O}$ in speleothems from Soreq cave during the late Holocene and the present (Affek et al., 2014). The blue dashed line indicates the mean $\delta^{18}\text{O}$ value in the northeastern Sahara carbonates. The red dash-dot-dash line defines the 50:50 source mixture line of the northeastern Sahara (i.e., Sannur, Dajara, and Kurkur) and Modern / late Holocene central Levant carbonates (i.e., Soreq speleothems).

3.12 Supplementary Materials

Table S1: Oxygen isotope composition of WS-5d stalagmite

Distance from the stalagmite top (mm)	$\delta^{18}\text{O}$ (VPDB, ‰)	Distance from the stalagmite top (mm)	$\delta^{18}\text{O}$ (VPDB, ‰)
0	-12.48	180	-10.54
5	-12.93	185	-12.40
10	-12.13	190	-11.94
15	-12.11	195	-11.80
20	-12.20	200	-12.08
25	-12.04	205	-12.16
30	-12.11	210	-11.96
35	-12.25	215	-12.41
40	-12.36	220	-12.47
45	-12.12	225	-12.16
50	-12.16	230	-12.11
55	-10.11	235	-12.04
60	-10.56	240	-11.91
65	-10.60	245	-12.19
70	-10.60	250	-12.27
75	-11.23	255	-11.65
80	-10.21	260	-12.10
85	-10.73	265	-11.94
90	-10.24	270	-11.93
95	-9.75	275	-11.99
100	-10.20	280	-12.13
105	-10.07	285	-12.16
110	-10.15	290	-12.03
115	-10.76	295	-12.12
120	-10.55	300	-12.28
125	-11.54	305	-11.97
130	-10.49	310	-11.66
135	-11.00	315	-12.13
140	-10.66	320	-12.38
145	-11.38	325	-11.99
150	-10.69	330	-12.21
155	-11.38	335	-12.20
160	-10.16	340	-12.18
165	-11.23	345	-12.09
170	-10.90	350	-12.08
175	-10.51	355	-11.43
Mean $\delta^{18}\text{O}$ = -11.6 ± 0.8 ‰ VPDB			

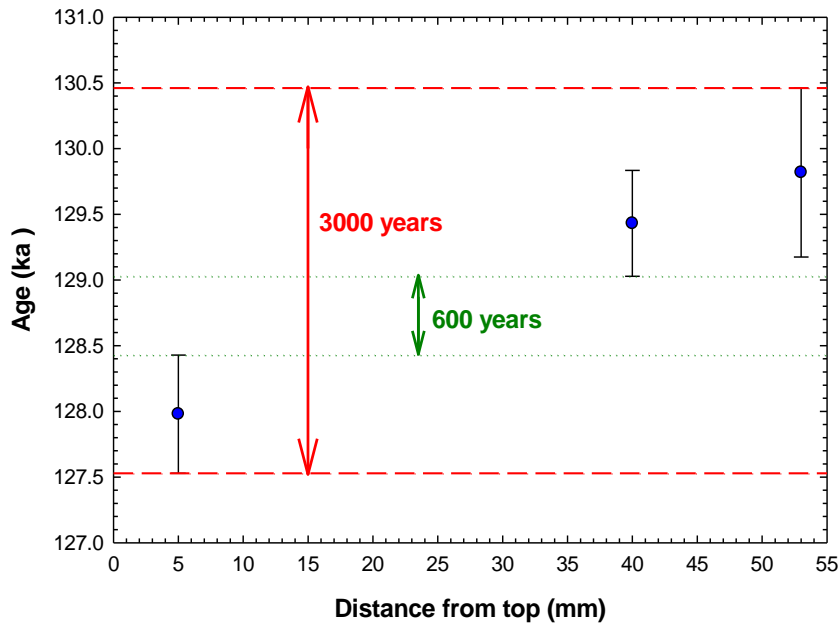


Fig. S1: The duration of the greening of the Sahara during the MIS 5.5. Blue dots show the U-Th dates ± 2 sigma errors. Red dashed and green dotted lines define the upper and lower limits of the greening period, respectively.

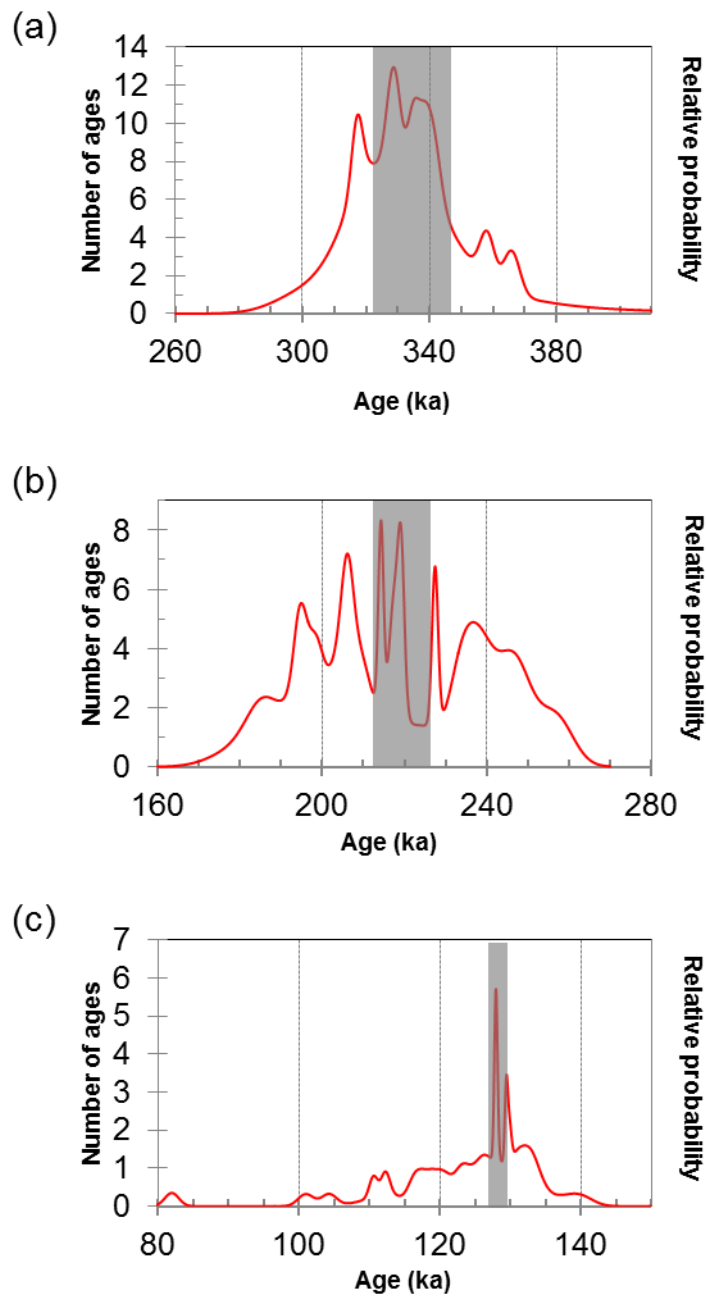


Fig. S2: Probability density plot of speleothem ages in the Northeast Sahara, Negev, and Southern Arabia deserts: (a) Speleothem growth peak during MIS 9, (b) Speleothem growth peak during MIS 7 (c) Speleothem growth peak during MIS 5. Grey shades show weighted mean age range of stalagmite growth in Wadi Sannur cave.

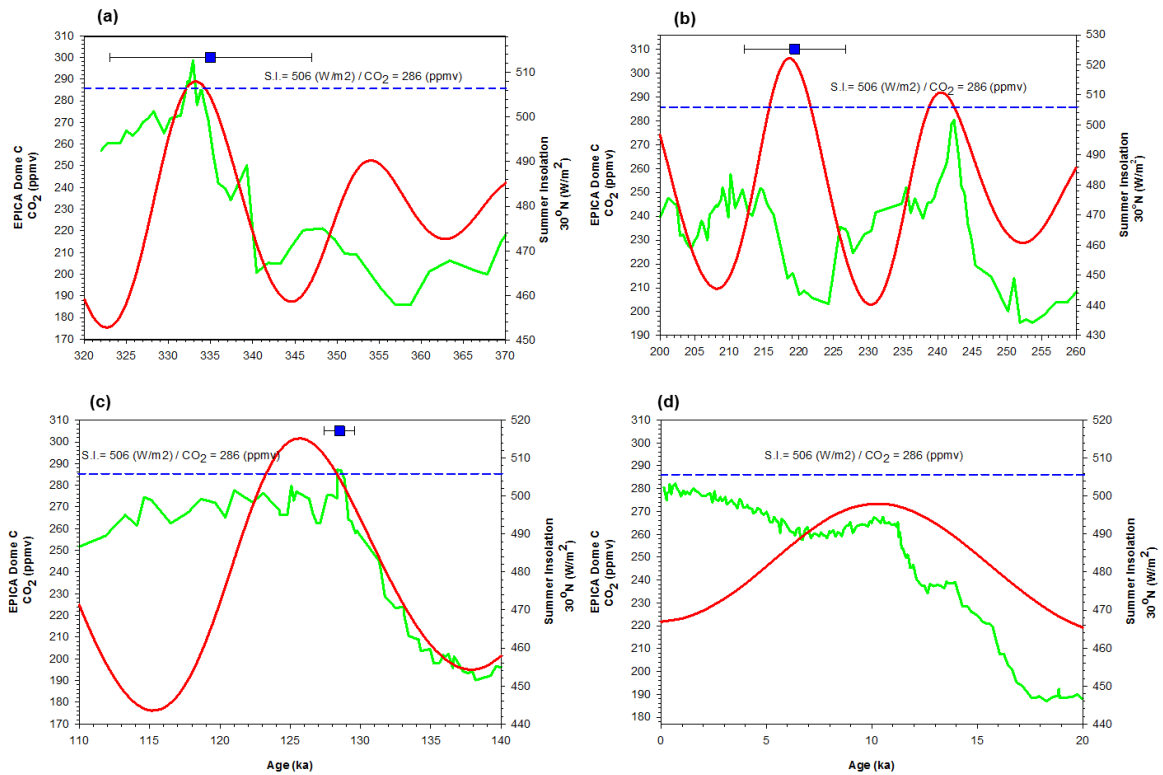


Fig. S3: Climate forcing factors of the West African Monsoon: (a) MIS 9; (b) MIS 7.3; (c) MIS 5.5; (d) MIS 1. The blue squares show the weighted mean age range of the stalagmite (WS-5d) growth in Wadi Sannur cave. The green curve represents the variability in the CO₂ concentration in EPICA Dome C (Lüthi et al., 2008). The red curve shows the cyclic variation in summer insolation. The blue dashed line defines the threshold values of the CO₂ and summer insolation required to trigger speleothem growth in Wadi Sannur cave (Laskar et al., 2004).

Chapter 4 - Disordering of ^{13}C - ^{18}O bond in CO_2 gas over a heated quartz surface at 50 – 1100 °C: Insights into the abundance of mass 47 (Δ_{47}) in CO_2 gas at thermodynamic equilibrium

Mohammed I. EL-Shenawy^{1,2} and Sang-Tae Kim¹

¹School of Geography and Earth Sciences, McMaster University, 1280 Main Street West, Hamilton, ON, L8S 4K1, Canada

²Department of Geology, Beni-Suef University, Beni- Suef, 62111, Egypt

To be submitted to *Rapid Communications in Mass Spectrometry*

3.1 Abstract

RATIONALE: CO₂ clumped isotope measurements (Δ_{47}) relate the abundance of ¹³C¹⁸O¹⁶O isotopologues in CO₂ molecules to the formation temperature of their parent CO₂ gas or carbonate minerals. The standardization of the Δ_{47} measurements relies on theoretically calculated equilibrium Δ_{47} values (i.e., Wang et al., 2004), which have not been experimentally measured yet.

METHODS: A series of CO₂ gases were purified using a custom-designed automated purification system, baked in a pre-cleaned dry quartz tubes and measured for their Δ_{47} values using an isotope ratio mass spectrometer, to study the kinetics of Δ_{47} in the CO₂ gas over a heated quartz surface between 50 and 1100 °C. To evaluate the effect of the conventional cleaning procedures on the Δ_{47} value, another subset of CO₂ gases was examined, but treated differently in the following order: baked, purified and measured for Δ_{47} values.

RESULTS: We demonstrated that Δ_{47} value of the CO₂ gas over a heated quartz surface attains thermodynamic equilibrium in 191, 7, 0.23 and 0.1 hour at 50, 100, 491 and 1000 °C, respectively. Our experimentally determined Δ_{47} – T relationship in CO₂ gas between 50 and 1100 °C was estimated as (Δ_{47} in ‰, T in °C; $R^2 = 0.99$, $P < 0.0001$):

$$\Delta_{47\text{equ}} = 0.9791 (\pm 0.0029) \text{ EXP } (-0.0045 * T)$$

We also found that the purification process can alter the original Δ_{47} value of the CO₂ gas by 0.04 to 0.07 ‰.

CONCLUSIONS: Heated CO₂ gas in a dehumidified quartz tube between 50 and 1100 °C can be used, as an alternative to preparing CO₂ standard gases to normalize raw Δ_{47}

data. Our heated CO₂ gas method enabled the experimental determination of the Δ_{47} – T relationship in CO₂, the preparation of CO₂ standard gases using a single method, and the measurement of any CO₂ sample against standards of similar Δ_{47} .

4.2 Introduction

In the past decade, clumped isotope measurements of CO₂ gas have been widely employed to resolve fundamental questions regarding the atmospheric budget of CO₂^[1-3], Earth and planetary paleoclimate^[4-8], continental tectonics^[9] and thermophysiology of extinct animal species.^[10] These measurements examined the abundance of the ¹³C-¹⁸O bond, mass 47 anomaly (Δ_{47}) \approx ¹³C¹⁸O¹⁶O isotopologue, in CO₂ molecules relative to that expected for stochastic distribution (i.e., all CO₂ isotopologues are randomly distributed). The abundance of the ¹³C-¹⁸O bond is thermodynamically controlled, being more dominant at low temperatures^[11]. As a result, the measured Δ_{47} in CO₂ molecules from either gas or solid origins is negatively correlated with the original formation temperature.^[2,12-14] However, the tight Δ_{47} -temperature scale (i.e., 1 ‰ reflects a 1000 °C change in temperature) and the extremely small fraction of the ¹³C¹⁸O¹⁶O isotopologue in CO₂ (46 ppm) require a rigorous analytical protocol to obtain absolute Δ_{47} values and thus accurate absolute temperature.^[15-17]

To obtain absolute Δ_{47} value of unknown CO₂ sample, several steps of corrections and standardizations need to be conducted on the measured raw Δ_{47} from the mass spectrometric analysis. These steps have been established to account for mass spectrometric artifacts, including nonlinearity between δ^{47} and Δ_{47} relationship and isotope scrambling effects in the ion source.^[15,16] Theoretically, CO₂ gases of a different bulk isotopic composition (i.e., δ^{47} is a combination of $\delta^{18}\text{O}$ and $\delta^{13}\text{C}$) equilibrated at a given temperature should possess the same Δ_{47} value.^[18] However, a positive δ^{47} - Δ_{47} relationship for the gases has been observed in practice.^[15,16] The slope and intercept of

the $\delta^{47} - \Delta_{47}$ relationship is shown to change over time (e.g., weeks to months). Therefore, a frequent characterization of the slope and the intercept of the $\delta^{47} - \Delta_{47}$ relationship is required to correct the measured Δ_{47} value of a CO_2 sample for its nonlinearity by projecting the measured Δ_{47} to the nonlinearity intercept using the measured slope.^[15] He *et al.*^[17] investigated the cause of the nonlinearity and attributed it to a negative drift in the base line reading when the CO_2 introduced to the ion source. They showed that the implementation of the pressure base line (PBL) can minimize and stabilize the nonlinearity over time (i.e., the slope).

Dennis *et al.*^[16] suggested that the measured raw Δ_{47} value might be altered by potential fragmentation and recombination of CO_2 molecules (the scrambling effect) when these molecules reside in the ion source of the isotope ratio mass spectrometer. They put forward an assumption that the magnitude of this scrambling effect is proportional to the abundance of $^{13}\text{C}-^{18}\text{O}$ bond in CO_2 molecules (i.e., the scrambling effect increases with increasing the Δ_{47} value). This can led to scale compression when raw Δ_{47} values of water-equilibrated CO_2 gases at low temperature and a heated CO_2 gas at 1000 °C are plotted against their corresponding Δ_{47} values from the theoretical work by Wang *et al.*^[11] Subsequently, the scrambling effect can be corrected for an unknown CO_2 sample by accounting for the scale compression in the nonlinearity-corrected Δ_{47} measurement. However, it is unclear whether the scale compression is caused by the scrambling effect in the ion source and/or the CO_2 cleaning procedures. Moreover, uncertainties in the theoretical calculations of Δ_{47} values might result in an erroneous scale compression.

Recently, Prasanna *et al.*^[19] showed that heated quartz can catalyze the breakdown of C-O bond in CO₂ gas at 500 to 1100 °C due to the interaction between the CO₂ molecules and the heated quartz surface. This breakdown of the C-O bond enabled the randomization of the isotopologues in CO₂ molecules and derived their Δ_{47} values toward the stochastic distribution with increasing temperature. However, two questions regarding the catalytic nature of the heated quartz remain unanswered and they are:

- (1) Does the physicochemical interaction between CO₂ molecules and the heated quartz surface drive the Δ_{47} value of the CO₂ gas to thermodynamic equilibrium value at a given temperature?
- (2) If so, how long does it take for CO₂ molecules to establish thermodynamic equilibrium with the quartz tube at a given temperature?

In this paper, we demonstrated that heating a purified CO₂ gas in a dry quartz tube can effectively breakdown the C-O bond from 50 to 1100 °C and the thermodynamic equilibrium with respect to Δ_{47} can be established within 1 week and few minutes, respectively. We also found that the CO₂ cleaning procedures are the main cause for the scale compression in the normalization of Δ_{47} data. Therefore, we isolated the CO₂ cleaning effect on the Δ_{47} value by reversing the purification protocol of the CO₂ (i.e., reversing the CO₂ baking – cleaning – measuring protocol to CO₂ cleaning – baking – measuring protocol) in order to experimentally determine the Δ_{47} – temperature relationship of CO₂ gas between 50 and 1100 °C.

4.3 Experimental

Experiments and mass spectrometric measurements were undertaken in the McMaster Research Group for Stable Isotopologues (MRSI) laboratory. Two experimental protocols were employed in this study: 1) CO₂ cleaning – baking – measuring (CBM) protocol and 2) CO₂ baking – cleaning – measuring (BCM) protocol. The name of each protocol provides the sequence of the analytical steps that are conducted on the CO₂ gas. The goal of the first protocol is to provide an independent measure of the temperature dependence of the equilibrium Δ_{47} in CO₂ by avoiding any potential reordering of the ¹³C-¹⁸O bond (raw Δ_{47}) due to the CO₂ cleaning procedures. The comparison between the two analytical protocols enables us to systematically compare the effect of the CO₂ cleaning procedures on the raw Δ_{47} value.

A number of 50 μ mol aliquots (equivalent to 5 mg carbonates) of CO₂ gases were collected in Pyrex® (for the 1st protocol) or quartz (for the 2nd protocol) break seals of a 15 cm length. Prior the CO₂ gas collection, the quartz tubes (GE 214) were carefully cleaned in three steps to eliminate any unfavorable reactions between CO₂ and the quartz surface in the presence of different contaminants during the baking process. These cleaning steps are:

- I. Soaking the quartz tubes in 10 % HNO₃ acid for 24 hours to dissolve potential alkali-ion carbonates that might form on the inside quartz surface in the presence of CO₂ and water vapour.
- II. Subsequent rinsing of the tubes by using tap water, distilled water and 18 M Ω deionized water (three times each) and drying them in an oven at 70 °C.

III. Heating the dried tubes in a high temperature furnace to 1000 °C for 2 hours to remove any organic contaminants^[20] and release water and hydroxyl groups attached to the quartz surface.^[21] After intermediate cooling, the quartz tubes were stored in a closed jar for future use.

The Pyrex® tubes were also heated to 550 °C for 2 hours before the gas collection to remove any possible organic contaminants.

In the first protocol, the CO₂ gases collected in the Pyrex® tubes were cleaned by using the automated purification system built by the MRSI. In this system, the CO₂ gas passes through three double-looped cryogenic U-traps (stainless steel) to remove water and non-condensable gases. Subsequently, the dehumidified CO₂ was released at -80 °C into the third cryogenic trap, which is connected to a U- trap of 15 cm (length) x 4 mm (I.D.) filled with PoraPak Q material (50 – 80 mesh; Supelco, Bellefonte, USA). The PoraPak trap was held at -20 °C and its downstream end was fitted to a LN₂ trap (-190 °C). The pressure gradient between the third cryogenic trap and the downstream LN₂ trap permits the dehumidified CO₂ to pass through the PoraPak Q trap, which is cold enough to allow slowdown CO₂ transfer (20 mins) and facilitate efficient removal of chlorocarbon and/or hydrocarbon contaminants. The downstream LN₂ trap was then warmed up to -80 °C to assure complete CO₂ transfer by comparing the CO₂ pressure before and after the PoraPak Q trap. The purified CO₂ gases were collected in the pre-cleaned quartz break seals. Note that these quartz break seals were aggressively heated with a hot flame when they were attached to the vacuum line (before the starting of the CO₂ purification process) in order to remove any residue water vapor. Finally, the quartz

break seals containing the purified CO₂ gas were baked (heated) for a chosen time period at given temperature (50 -1100 °C). Upon the completion of this baking process, the quartz break seals are immediately quenched in cold water (18 °C) to eliminate gradual cooling, which may cause the isotopic reordering of the CO₂ isotopologues at lower temperatures than those of the baking temperature.

Using the first protocol, the kinetics of Δ_{47} of CO₂ gas over a heated quartz surface was examined. Three different CO₂ gases were used to conduct the experiments in the first protocol. Two of the CO₂ gases (i.e., MRSI-T2 and MRSI-T4) are Coleman instrument grade (purity 99.99 %) and the third CO₂ gas was prepared by the acid (ultrapure 103 % H₂PO₃) digestion of Carrara marble at room temperature. The carbon and oxygen isotope compositions of the three CO₂ gases are listed in Table 4.1. We studied the time evolution of the Δ_{47} in CO₂ gas (i.e., MRESI-T4) at four temperatures (50, 100, 491 and 1000 °C). Once the Δ_{47} attains a steady state (i.e., no change in the Δ_{47} value with time after continues evolution from the starting Δ_{47} value at time zero), the equilibration time for a given experimental condition was defined. These equilibration times were used as a reference to prepare three CO₂ gases (δ^{47} values range from -39 ‰ to 20 ‰) at their isotopic equilibria in regard to mass 47 (Δ_{47}) at multiple temperatures between 50 and 1100 °C.

In the second protocol (CO₂ baking – cleaning - measuring protocol), the CO₂ gases (no prior cleaning) collected in the quartz break seals were baked first, for the equilibration times used in the first protocol, at 100, 200, and 1000 °C. The hot quartz break seals are then quenched in cold water after the completion of the baking process.

Subsequently, the quenched CO₂ gas was cleaned, as described in the 1st protocol, and measured for its Δ_{47} value. The second protocol was conducted on two CO₂ gases (MRSI-T2 and CARRARA).

The end product CO₂ gases from the two protocols were analyzed on a Thermo Finnigan MAT 253 DI-IRMS equipped with faraday cups to measure masses 44 – 49. Each CO₂ sample measurement consisted of 6 acquisitions with 20.5 cycles per acquisition (i.e., 4.5 off-peak cycles, 12 on-peak cycles and 4 off-peak cycles, respectively). The off-peak cycles were implemented to correct the pressure baseline (PBL), which is found to reduce the dependency of Δ_{47} on δ^{47} and stabilize the linear δ^{47} - Δ_{47} relationship over time (e.g., up to 5 months^[17]). The integration time was 26 s per change over. The bellows pressure was adjusted to 16 V at mass 44 before the beginning of each acquisition. The CO₂ gases were measured against an OzTech reference gas ($\delta^{13}\text{C}_{\text{VPDB}} = 5.62 \text{ ‰}$ and $\delta^{18}\text{O}_{\text{VSMOW}} = -25.05 \text{ ‰}$). CO₂ samples were measured on the mass spectrometer within the same day of completing each experimental protocol and the analytical time was about 3.5 hours. The PBL- corrected Δ_{47} values measured in this study were used in the section of results and discussions without any further corrections (e.g., based upon heated gas or absolute reference frame) to provide independent measure of the temperature dependence of the equilibrium Δ_{47} in CO₂ gas.

In this study, we measured Δ_{47} and Δ_{48} (i.e, contamination indicator) for CO₂ isotopologues and they were calculated as:^[15]

$$\Delta_{47} = \left[\left(\frac{R^{47}}{R^{47*}} - 1 \right) - \left(\frac{R^{46}}{R^{46*}} - 1 \right) - \left(\frac{R^{45}}{R^{45*}} - 1 \right) \right] \quad (4.1)$$

$$\Delta_{48} = \left[\left(\frac{R^{48}}{R^{48*}} - 1 \right) - 2 \left(\frac{R^{46}}{R^{46*}} - 1 \right) \right] \quad (4.2)$$

where R^{45} , R^{46} , R^{47} , R^{48} are the observed ratios of masses 45 to 48 relative to mass 44 in CO₂; whereas R^{45*} , R^{46*} , R^{47*} , R^{48*} represent the corresponding stochastic distribution ratios based on the $\delta^{18}\text{O}$ and $\delta^{13}\text{C}$ of the sample and are calculated as follows:

$$R^{45*} = R^{13} + 2R^{17}, \quad (4.3)$$

$$R^{46*} = 2R^{18} + 2R^{13} \times R^{17} + (R^{17})^2, \quad (4.4)$$

$$R^{47*} = 2R^{13} \times R^{18} + 2R^{17} \times R^{18} + R^{13} \times (R^{17})^2, \quad (4.5)$$

$$R^{48*} = (R^{18})^2 + R^{13} \times 2R^{17} \times R^{18} \quad (4.6)$$

We also measured the bulk isotopic composition of the CO₂ (δ^{47}), which is defined as:^[15]

$$\delta^{47}_{(\text{SG-WG})} = \left(\frac{R^{47}_{\text{SG}}}{R^{47}_{\text{WG}}} - 1 \right) \quad (4.7)$$

where the R^{47}_{SG} and R^{47}_{WG} are the intensities of mass 47 to the intensity of mass 44 for the sample (heated CO₂, HG, in this study) and working (standard) gases, respectively.

The Δ_{47} , Δ_{48} and δ^{47} are all measured in permil unit (‰).

4.4 RESULTS AND DISCUSSION

4.4.1 Time series experiments

The results from baking the MRESI-T4 CO₂ gas at temperatures 50, 100, 491 and 1000 °C for chosen periods of time using the first experimental protocol are listed in Table 4.2.

4.4.1.1 Carbon and oxygen isotope compositions of the baked CO₂ gases

The carbon isotope composition of the baked CO₂ gases ($\delta^{13}\text{C}_{\text{VPDB}}$) used in this study has an average of $29.99 \pm 0.07 \text{ ‰}$ (1σ), which has not been significantly evolved from that of the starting gas ($30.04 \pm 0.01 \text{ ‰}$) with baking time and temperature during the experiments (Fig. 4.1). This is due to the presence of a single carbon reservoir (CO₂ gas) in the quartz tubes. The oxygen isotope values of the baked CO₂ gases ($\delta^{18}\text{O}_{\text{VSMOW}}$) stayed constant with baking time at 50, 100 and 491 °C (Fig. 4.1). The $\delta^{18}\text{O}_{\text{VSMOW}}$ values of the baked gases at 100 and 491 °C are identical to those of the starting gas ($12.30 \pm 0.02 \text{ ‰}$) suggesting that there was no oxygen isotope exchange between the CO₂ gas and the inside surface of the quartz tubes at these temperatures. However, the $\delta^{18}\text{O}_{\text{VSMOW}}$ value of the baked gases at 50 and 1000°C (11.29 ± 0.01) is lower than the $\delta^{18}\text{O}_{\text{VSMOW}}$ of the starting gas by 1 ‰ (Table 4.2). This might be explained by oxygen isotope exchange between the large CO₂ reservoir and water traces in the Pyrex tubes after the collection and during the storage of the CO₂ gas before the cleaning procedures. We assume that this oxygen isotope exchange has no effect on the Δ_{47} value of the starting gas because the exchange occurred at room temperature. In addition, a small gradual increase of 0.54 ‰ in the $\delta^{18}\text{O}_{\text{VSMOW}}$ value of CO₂ was observed over four hours of baking at 1000 °C. This gradual increase suggests slow oxygen isotope exchange between the CO₂ gas and quartz tube at a high temperature.

Overall, the constant $\delta^{13}\text{C}_{\text{VPDB}}$ along with the 1 ‰ shift in the $\delta^{18}\text{O}_{\text{VSMOW}}$ of the CO₂ gases resulted in a small change of 1.67 ‰ in the δ^{47} of CO₂ gases during the experiments (Fig. 4.1). Large changes in the δ^{47} of CO₂ gases require a non-linearity correction (δ^{47} -

Δ_{47}) to enable the comparison between the measured raw Δ_{47} values in CO_2 gases of different bulk isotopic compositions (δ^{47}). However, the 1.67 ‰ change in δ^{47} observed in our time evolution experiments can cause only a maximum error of 0.0015 ‰ in the raw Δ_{47} value, which is smaller than the analytical error (see section 4.4.3 for details).

4.4.1.2 Time evolution of Δ_{47} in baked CO_2 gases

In contrast to the $\delta^{13}\text{C}_{\text{VPDB}}$ and $\delta^{18}\text{O}_{\text{VSMOW}}$ values, the raw Δ_{47} value of the baked gases decreases exponentially with increasing the baking time from the value of the starting gas (raw $\Delta_{47}(t_0) = 0$ ‰) toward a time-invariant Δ_{47} value at a given test temperature (Fig. 4.2). This time-invariant Δ_{47} value decreases with increasing the baking temperature, which is in agreement with the temperature dependency of the Δ_{47} value in CO_2 gas.^[1,11] The observed decrease in the Δ_{47} value with baking temperature and time reflects a significant disordering of the ^{13}C - ^{18}O bond in the CO_2 gas and therefore decreasing abundance of the $^{13}\text{C}^{18}\text{O}^{16}\text{O}$ isotopologues, which contribute approximately 97 % of mass 47. Consequently, the time evolution of the Δ_{47} value is a mirror to the abundance of the $^{13}\text{C}^{18}\text{O}^{16}\text{O}$ isotopologues and can be expressed by the following equation:^[20]

$$\Delta_{47}(t) = \Delta_{47\text{equ}} + (\Delta_{47}(t_0) - \Delta_{47\text{equ}}) \exp(-kt) \quad (4.8)$$

where $\Delta_{47}(t)$ and $\Delta_{47}(t_0)$ are the Δ_{47} values of the baked CO_2 gas at a given time and the starting CO_2 gas, respectively, which are in isotopic disequilibrium at the baking temperature; $\Delta_{47\text{equ}}$ defines the time-invariant Δ_{47} value (i.e., isotopic equilibrium with baking temperature); k is the rate constant of the Δ_{47} evolution, and t is the baking time.

We fit our Δ_{47} data from the time evolution experiments to equation (4.8) in order to estimate the rate constant (k) and the equilibration time at a given temperature. The rate constants of the Δ_{47} decrease are equal to $0.021 \pm 0.002 \text{ h}^{-1}$, $0.577 \pm 0.036 \text{ h}^{-1}$, $0.288 \pm 0.008 \text{ min}^{-1}$ and $1.700 \pm 0.136 \text{ min}^{-1}$ at 50, 100, 491 and 1000 °C, respectively. Based upon these rate constants, the $\Delta_{47\text{st}}$ value of the baked gases attains isotopic equilibrium ($\Delta_{47\text{equ}}$) in 191, 7, 0.23 and 0.1 hour at 50, 100, 491 and 1000 °C respectively. This temperature dependence of the rate constant reflects the T-dependence of the breaking of the ^{13}C - ^{18}O bond. The breaking of the C-O bond in a pure CO_2 gas phase is extremely slow below several hundred degrees Celsius (activation energy (E_a) of 128.6 kJ/mol).^[20] However, the breaking of the C-O bond can be accelerated by either oxygen isotope exchange between CO_2 and water at low temperatures^[20,22] or interaction between CO_2 and the heated surface of a catalyst (e.g., platinum or quartz) at high temperatures.^[19] In our experiments, cryogenically cleaned CO_2 was baked in dry quartz tubes. However, the activation energy calculated from the Arrhenius plot of our data (Fig. 4.3) possesses a similar value ($27.86 \pm 4.27 \text{ kJ/mol}$) to the estimated value ($21.8 \pm 2.6 \text{ kJ/mol}$) from the study of $\text{CO}_2 - \text{H}_2\text{O}$ equilibration.^[20] While the activation energy of the breakdown of C-O bond via the interaction between the heated quartz surface and CO_2 molecules may be similar to that of $\text{CO}_2 - \text{H}_2\text{O}$ equilibration, the similarity in activation energies may suggest that traces of water released off the quartz surface during the baking process accelerated the breaking of the C-O bond in CO_2 through oxygen isotope exchange between CO_2 and water.

To test this possibility, we pumped empty quartz tubes under high vacuum for ten minutes (equal to the pumping time before the starting of CO₂ cleaning process on the automated line). The tubes were sealed and baked for 2 hours at 1000 °C and then the contents were introduced into the mass spectrometer to measure the intensity of the m/e = 18 (water) signal. The intensity of m/e = 18 was identical to the background value (183 mv) when the sample bellow (pumped overnight) is opened to the ion source, suggesting that no water was released from the quartz surface during the baking process. This suggests that the activation energy of C-O bond breaking that we measured is only coincidentally similar to that for the water-catalyzed process. Notwithstanding the dryness of the quartz tubes however, we cannot rule out the presence of water traces in the cryogenically cleaned CO₂ but these traces might not be enough to facilitate the breakdown of all C-O bonds in the major oxygen reservoir (CO₂ gas) through oxygen isotope exchange between CO₂ and water.

4.4.2 Effect of the CO₂ cleaning procedures on the raw Δ_{47}

In our first working protocol, we carried out the cleaning of the CO₂ gas before the baking process to avoid any potential isotopic reordering of the baked CO₂ gas during the gas cleaning process, which might alter the measured Δ_{47} value. Avoiding any isotopic reordering of the CO₂ gas after the baking process is critical in this study because the purpose of this study is to examine the temperature dependence of the equilibrium Δ_{47} value of CO₂. However, the failure to eliminate any contaminants (e.g., organics and water) released from the quartz tubes during the baking process in the first protocol might

affect the measured Δ_{47} value as well. Therefore, we employed the two protocols to CO₂ gases MRSI-T2 and CARARRA, baking them for our measured equilibration times at 100, 200 and 1000 °C. This exercise enabled us to directly compare the measured Δ_{47} values from the two protocols in order to:

- 1) Check the release of contaminants into the CO₂ during the baking process in the first protocol.
- 2) Quantify any potential isotopic reordering inducing by the cleaning procedures of CO₂ gas in the second protocol.

A significant release of organics, such as chlorocarbons and hydrocarbons, into the baked CO₂ gas in the first protocol would result in a higher Δ_{48} value (≥ 2 ‰) than that measured in a clean gas of a same bulk isotopic composition.^[23,24] Elevated Δ_{48} values have been shown to positively correlate with spurious Δ_{47} values.^[1] Figure 4.4 shows the Δ_{48} offset for CO₂ gases measured in the first protocol from the mean Δ_{48} values of the same CO₂ gases which are measured in the second protocol at same baking temperatures. The Δ_{48} offset values vary between -0.47 and 1.03 ‰ within the acceptable limit (≤ 2 ‰)^[e.g., 23,24] and suggest no significant release of chlorocarbons and hydrocarbons into the baked CO₂ gas in the first protocol. In addition, the monitoring of water background carried out in this study implied that the quartz tubes were dry and did not contribute any water traces over the course of the baking process. As results, the Δ_{47} values of the CO₂ gases baked at same temperature in the first and second protocol are expected to be statistically indistinguishable if the CO₂ cleaning process has no effect on the Δ_{47} value in the second protocol.

However, a comparison between the Δ_{47} measured in CO₂ gases from the two protocols in this study demonstrates that all gases measured in the first protocol displayed lower Δ_{47} values than those values measured in the second protocol (Fig. 4.5). Moreover, the magnitude of the decrease in the Δ_{47} values in the first protocol from those values in the second protocol increases in CO₂ gases toward the stochastic distribution (i.e., 0.04 ‰ at 100 and 200 °C to 0.07 ‰ at 1000 °C). The difference in the Δ_{47} values between the two protocols (Fig. 4.5) might be explained by stronger isotopic reordering (increase in Δ_{47}) of the CO₂ isotopologues formed at high temperatures than those formed at low temperature during the CO₂ cleaning procedures in the second protocol. Isotopic equilibration of CO₂ isotopologues to low temperatures (-190, -80, -20 °C) during the cleaning process would produce an increase in the Δ_{47} value. This increment will depend on how far the CO₂ gas is from the stochastic distribution, resulting in larger increase in the Δ_{47} value of CO₂ near stochastic distribution and smaller increase in Δ_{47} of CO₂ far from stochastic distribution. Dennis *et al.*^[16] reported four different values of scale compression when they compared the measured Δ_{47} values from four different laboratories (different mass spectrometers and cleaning lines) to the theoretical isotopic equilibrium Δ_{47} values.^[11] They explained this scale compression by the isotope scrambling effects in the ion source. Our experimental observations from the comparison study between the two experimental protocols (BCM and CBM) suggest that scale compression values observed in routine clumped isotope analyses (usually using the BCM protocol) might be a result of the isotopic reordering induced by the CO₂ cleaning process rather than the scrambling effects in the ion source.

4.4.3 Temperature dependence of equilibrium Δ_{47} of CO_2 gas at MRSI

Using the first protocol, three CO_2 gases, namely MRSI-T2, MRSI-T4 and CARARRA, were baked for a longer time than the measured equilibration time measured (i.e., \geq equilibration time from time evolution experiments) at a given temperature to assure that the CO_2 isotopologues attained thermodynamic equilibrium with respect to Δ_{47} . During the preparation and the baking processes of CO_2 gases, small changes in the bulk isotopic composition (δ^{47}) of the three gases were measured. These changes were mainly due to oxygen isotope exchange between CO_2 and water traces at room temperature during the CO_2 storage in the Pyrex tubes and oxygen isotope exchange between the CO_2 gas and the quartz at high temperatures of baking. These changes in δ^{47} vary from 1.76 ‰ in MRSI-T4 gas to 2.71 ‰ in Carrara gas. The change of 2.71 ‰ in the δ^{47} can only cause a maximum shift of 0.0024 ‰ (= 2.76 * nonlinearity slope (slope_{HGL})) in the measured Δ_{47} value from the true Δ_{47} of CO_2 gas of a stable δ^{47} , due to the nonlinearity effect ($\delta^{47} - \Delta_{47}$; Fig. 4.6). However, this shift cannot be analytically resolved by the current generation of mass spectrometers (MAT 253); therefore, we treated each gas as if it had a stable δ^{47} over the 50 – 1100 °C temperature range. The very shallow nonlinearity slope of 0.009 measured on our MAT 253 is due to the implementation of the pressure base line correction protocol.^[17] The PBL-corrected Δ_{47} (raw) measurements of each gas at thermodynamic equilibrium between 50 and 1100 °C are shown in Figure 4.7 and Table 4.3.

To define the temperature dependence of equilibrium Δ_{47} in CO₂ gas, we performed a three parameter-exponential fit on all the measurements of the Δ_{47} from each gas individually (Fig. 4.7). The exponential fit is used for two reasons: 1) The raw Δ_{47} data are well-fitted by this exponential function ($R^2 = 0.99$ and $p < 0.0001$); and 2) CO₂ isotopologues are expected to attain stochastic distribution at high temperature.^[11] The best fit of the raw Δ_{47} of each gas versus temperature is expressed as:

for MRSI-T2;

$$\text{Raw } \Delta_{47\text{equ}} = - 0.9054 (\pm 0.0035) + 0.9739 (\pm 0.0070) \exp (- 0.0044 * T) \quad (4.9)$$

for MRSI-T4;

$$\text{Raw } \Delta_{47\text{equ}} = - 0.9248 (\pm 0.0029) + 0.9736 (\pm 0.0050) \exp (- 0.0045 * T) \quad (4.10)$$

for Carrara;

$$\text{Raw } \Delta_{47\text{equ}} = - 0.8659 (\pm 0.0040) + 0.9851 (\pm 0.0083) \exp (- 0.0045 * T) \quad (4.11)$$

where Raw $\Delta_{47\text{equ}}$ is the value of Δ_{47} at thermodynamic equilibrium (in ‰) of the baked gas relative to the working gas. The constant term indicates the estimated Δ_{47} at stochastic distribution for each gas relative to the working gas, which has a Δ_{47} value at thermodynamic equilibrium with room temperature. The coefficient of the exponential term is the difference between the Δ_{47} at stochastic distribution and the Δ_{47} in thermodynamic equilibrium at zero °C. The number within the exponential brackets is the temperature – dependence constant. T is the temperature in °C. Errors are given as 1 SE from the fit calculations. Both values of the temperature – dependence constant and difference between the Δ_{47} at stochastic distribution and that value at zero °C for the three gases in Eqs (4.9), (4.10) and (4.11) are nearly identical (within the 1 SE); therefore they are not gas-specific but they might be influenced by the isotope scrambling effects in the

ion source. However, these two values reflect the stability of the nonlinearity measured from the mass spectrometer over the duration of our experiments (i.e., three months). Using the pressure base line correction protocol, He *et al.*,^[17] showed that the intercept and the slope of the $\delta^{47} - \Delta_{47}$ relationship were stable for 5 months under constant source tuning conditions. The value of Δ_{47} at stochastic distribution, in Eqs (4.9), (4.10) and (4.11), increases with increasing the δ^{47} of the CO₂ gas (i.e., gas-specific) due to the nonlinearity effect (Fig. 4.6). Figure 4.7 demonstrates that the Δ_{47} of the three CO₂ gases decreases with increasing temperature approaching stochastic distribution at temperatures > 1000 °C.^[11]

4.4.4 Correction and standardization of the raw Δ_{47} – temperature relationship

Equations (4.9), (4.10) and (4.11) represent a laboratory-specific Δ_{47} – temperature calibration in regard to the working gas standard and ion source effects of the mass spectrometer used in MRSI laboratory. In order to transfer this laboratory-specific Δ_{47} – temperature calibration to an absolute Δ_{47} – temperature calibration, two steps of correction and standardization are required. These steps are: (1) correction for any isotope scrambling induced by the ion source in mass spectrometer (if present), and (2) standardization of the equations (4.9), (4.10) and (4.11) by substituting the negative Δ_{47} value relative to the working gas at stochastic distribution for each gas by zero (i.e., absolute $\Delta_{47} = 0$ at stochastic distribution).

Dennis *et al.*^[16] evaluated the scrambling effects in the ion source by comparing the raw Δ_{47} values from heated gases at the intercept of the $\delta^{47} - \Delta_{47}$ relationship (i.e., $\Delta_{47-[HG-wG]_0}$) to the theoretical reference frame by Wang *et al.*^[11] and estimating the scale

compression. However, the scale compression in Dennis *et al.*,^[16]'s study might be partly a result of the cleaning procedures. In this study, we have isolated the effect of cleaning process and consequently estimated ion source effects using a similar approach to that of Dennis *et al.*,^[16] The $\Delta_{47-[\text{HG-WG}]_0}$ values were estimated from the linear regression of the raw Δ_{47} data with one common slope in Figure 4.6. Subsequently, these $\Delta_{47-[\text{HG-WG}]_0}$ values were plotted against their corresponding predicted Δ_{47} values from Wang *et al.*,^[11] (Fig. 4.8). The slope of linear regression in Figure 4.8 enables us to either evaluate the scrambling effects in the ion source (when the slope is > 1) or accuracy of the theoretical predictions (when the slope is ≤ 1).^[25] Figure 4.8 shows that the slope between the $\Delta_{47-[\text{HG-WG}]_0}$ values and predicted Δ_{47} values from Wang *et al.*,^[11] is very close to unity (i.e., slope = 0.9987), suggesting absence of isotope scrambling effects in the ion source of the MRSI-MAT 253^[e.g., 1] as well as excellent agreement between Wang *et al.*^[11]'s model and our experimental values for Δ_{47} . As a result, the standardization of the Eqs (4.9), (4.10) and (4.11) (i.e., substituting the constant terms in the three equations by 0) yields the following absolute Δ_{47} – temperature calibration (Δ_{47} in ‰, T in °C; $R^2 = 0.99$, $P < 0.0001$):

$$\text{Absolute } \Delta_{47\text{equ}} = 0.9791 (\pm 0.0029) \exp (-0.0045 * T) \quad (4.12)$$

This absolute Δ_{47} – temperature calibration is the first experimental calibration of the mass 47 in CO₂ gas between 50 and 1100 °C. The standard error of the absolute $\Delta_{47\text{equ}}$ estimated from the fit of our experimental data is ± 0.004 ‰.

4.4.5 Comparison with the theoretical Δ_{47} – temperature relationship^[11]

The expected abundance of mass 47 (Δ_{47}) in CO₂ gas at thermodynamic equilibrium has been theoretically determined based upon the application of quantum mechanical and statistical thermodynamic principles to spectroscopic data of CO₂^[11] and is shown in Figure 4.9. These theoretical calculations are the base of the absolute reference frame for Δ_{47} measured in CO₂ studies.^[16] Our experimental Δ_{47} – temperature calibration is in excellent agreement with the theoretical Δ_{47} – temperature calibration calculated by Wang *et al.*^[11] between 100 and 400 °C (Fig. 4.9). However, the theoretical Δ_{47} values are higher than those from our experimental calibration by about ≤ 0.0225 ‰ and ≤ 0.0186 ‰ at low temperature (<100 – 50 °C) and high temperature (> 400 °C), respectively. These offsets between the theoretical and experimental calibrations can lead to errors in the determination of the apparent equilibrium temperature ranging from several °C at low temperatures to hundreds of degrees at high temperatures. Three sources of errors might affect our experimental approach and cause disagreement with the theoretical calculations (if the theoretical calculations are correct). These sources are: (1) the baked CO₂ did not reach thermodynamic equilibrium in regard to Δ_{47} at a given temperature; (2) the effects of isotope scrambling in the ion source; and (3) the uncertainty in the exponential fit of our experimental data.

If the first source is the main cause for disagreement between the experimental and theoretical calibrations, we should observe a significant difference in the internal and external coefficients of the exponential term among equations (4.9), (4.10) and (4.11) because the starting Δ_{47} ($\Delta_{47}(t_0)$) of the three gases were different. In particular, the Δ_{47}

(t_0) of MRSI-T2 and MRSI-T4 were close to zero whereas, the Δ_{47} (t_0) of Carrara was - 0.489 ‰. Moreover, incomplete equilibration of MRSI-T2 and MRSI-T4 gases at given temperatures between 50 and 1100 °C would result in higher absolute Δ_{47} than those values predicted in Wang *et al.* ^[11] Our experimental data shows near identical values for the coefficients of equations (4.9), (4.10) and (4.11), and lower absolute Δ_{47} than those values calculated in Wang *et al.*,^[11] ruling out the first source as a cause for the disagreement between our experimental data and the theoretical calculations. Second, Figure 4.8 indicates that no isotopic scrambling effects occurred in the ion source. Third, the uncertainty in the exponential fit of our experimental data (i.e., 0.004 ‰) cannot account for these offsets at low and high temperatures. Nevertheless, Wang *et al.*, ^[11] have not reported a numerical value for uncertainty in their calculations of Δ_{47} , which might engender errors due to the complication in the correction terms used in their calculation model.^[26] If the uncertainty in Wang *et al.*,^[11]'s approach is as high as 0.0225 ‰ (?), their calculated Δ_{47} values are in a complete agreement with those measured in our experiment. Other researchers^[e.g., 26,27] applied different theoretical methods to estimate the Δ_{47} in CO₂ gas at thermodynamic equilibrium. These theoretical methods showed a discrepancy of up to 0.1 ‰ in the Δ_{47} value calculated at a given temperature, suggesting that theoretical methods might introduce large errors in the calculated Δ_{47} value.

4.4.6 Implications for the correction scheme of the carbonate clumped isotope thermometry

Clumped isotopes in carbonate minerals have been used to reflect the temperature of the environment in which these minerals formed; these temperature calculations do not

require any knowledge of the oxygen isotope composition of the carbonate parent water.^[6,12] Clumped isotopes in carbonates are obtained by measuring the Δ_{47} of purified CO_2 after its liberation by the digestion of these carbonates in phosphoric acid. The measured Δ_{47} (raw) of this CO_2 has to be calibrated against CO_2 standard gases of known Δ_{47} values (i.e., equilibrated and heated gases of Δ_{47} values predicted by the theoretical work of Wang *et al.*,^[11]). The equilibrated gases of known Δ_{47} values are generated by complete oxygen isotope exchange between CO_2 and H_2O at low temperatures (0 - 50 °C) and heating CO_2 in quartz tubes at 1000 °C.^[15,16] Non-identical treatment (IT principle) of the CO_2 standard gases may cause artificial empirical transfer function (i.e., raw Δ_{47} versus theoretical Δ_{47}) and therefore lead to miscalculated absolute Δ_{47} in unknown CO_2 samples. For instance, after equilibrating CO_2 with water the reaction vial is submerged into liquid nitrogen to avoid any exchange between CO_2 and H_2O at room temperature and subsequently, the CO_2 released under vacuum by replacing the LN_2 by alcohol slush (-80 °C). This might lead to deviation of the raw Δ_{47} of CO_2 from equilibrium at the equilibration temperature due to potential fractionation of CO_2 caused by the high solubility of CO_2 in water at low temperatures (i.e., unrecovered fraction of CO_2 ^[20]) and/or partial equilibration of CO_2 with water at -80 °C. In contrast, heated gas is treated differently because the quartz tube containing the CO_2 is quenched in cold water or room air after the equilibration, preserving the raw Δ_{47} constant for a long time at room temperature.^[16]

Our experiments show that heating CO_2 gases in quartz tubes can drive the Δ_{47} of CO_2 to thermodynamic equilibrium at 50 to 1100 °C within 1 week to a few minutes,

respectively. Therefore, these experiments provide an alternative way to generate CO₂ standard gases of known Δ_{47} values and facilitate identical treatment of all the standard gases at low and high temperatures (i.e., using a single method). Moreover, it is well known in conventional stable isotope analysis that samples should be measured along with standards of similar isotope ratios to those of the samples to obtain accurate isotopic ratio for the measured samples. Similarly, CO₂ samples in clumped isotope analysis should be calibrated against CO₂ standards of similar Δ_{47} values to these samples. In the absolute reference frame proposed by Dennis *et al.*^[16] equilibrated gases at low temperatures have raw Δ_{47} values close to those of carbonate formed at ≤ 20 °C (when carbonate digestion performed at 90 °C) whereas the raw Δ_{47} values of the 1000 °C gases are lower than those of carbonate formed at stochastic distribution by about 0.280 ‰ (i.e., acid fractionation factor). However, CO₂ standard gases of similar raw Δ_{47} to the carbonates formed at intermediate and high temperatures (e.g. NBS 19, Carrara, and high temperature synthetic carbonates) cannot be generated by the CO₂-H₂O equilibration technique; use of this method might lead to errors in the corrected Δ_{47} values of these carbonate samples. In this study, heated CO₂ gas in quartz tubes produced CO₂ standards spanning the complete low to high temperature Δ_{47} scale enabling precise calibration of carbonate samples of different formation temperatures.

Finally, if the experimental Δ_{47} - T calibration in this study is used in the absolute reference frame as an alternative to the theoretical predictions of the Δ_{47} values^[11], the offset between the measured^[e.g.,28] and the theoretical^[13,14] Δ_{47} - T relationship in carbonates would be minimal.

4.5 Conclusions

Our experiments show that the interaction between CO₂ and heated quartz surfaces disordered the C-O bond and drove the CO₂ isotopologues to thermodynamic equilibrium with respect to Δ₄₇. Consequently, the first experimental calibration of the Δ₄₇ – T relationship in CO₂ gas phase between 50 and 1100 °C was proposed, based upon reproducible Δ₄₇ measurements in three CO₂ gases of different bulk isotopic compositions (δ⁴⁷). The exponential fit of these measurements yields the following equation:

$$\Delta_{47\text{equ}} = 0.9791 (\pm 0.0029) \exp (-0.0045 * T)$$

This equation is a pure temperature dependent relationship and not influenced by artifacts in the mass spectrometric analysis (e.g. nonlinearity and ion source effects).

Our results also demonstrate that the CO₂ cleaning procedures might be the main cause for the scale compression observed in the empirical transfer function of the absolute reference frame (e.g. Dennis et al., 2011). We encourage the clumped isotope community to test this suggestion using the two experimental protocols described in this study.

Finally, the use of heated CO₂ gases from different temperatures between 50 and 1100 °C will lead to improvement in the correction scheme of raw Δ₄₇ measurements in mass spectrometric analysis because of the following reasons:

- (1) unlike the combination of CO₂-H₂O equilibrated gases and heated gas in Dennis et al. (2011)'s protocol, heating CO₂ gases between 50 and 1100 °C enables the identical treatment (i.e., single method for preparation) of the CO₂ standards used to construct the empirical transfer function.

- (2) Heated CO₂ gases between 50 and 1100 °C can be used to generate CO₂ standards similar in their Δ_{47} values to those of the measured samples.
- (3) The heated CO₂ gases allow the experimental determination of the $\Delta_{47} - T$ relationship in CO₂ gas phase to test/validate the theoretical models.

4.6 Acknowledgments

The authors would like to thank Prof. Henry Schwarcz for his insightful review and comments on the original manuscript. We gratefully acknowledge the technical support of Martin Kynf in the laboratory of McMaster Research Group for Stable Isotopologues (MRSI). This work was supported by the NSERC Discovery Grants Program (386188-2010) to S.-T. Kim.

4.7 References

- [1] J. M. Eiler, E. Schauble. $^{18}\text{O}^{13}\text{C}^{16}\text{O}$ in Earth's atmosphere. *Geochim. Cosmochim. Acta* **2004**, 68, 4767.
- [2] H. P. Affek, J. M. Eiler. Abundance of mass 47 CO_2 in urban air, car exhaust, and human breath. *Geochim. Cosmochim. Acta* **2006**, 70, 1.
- [3] H. P. Affek, X. Xu, J. M. Eiler. Seasonal and diurnal variations of $^{13}\text{C}^{18}\text{O}^{16}\text{O}$ in air: Initial observations from Pasadena, CA. *Geochim. Cosmochim. Acta* **2007**, 71, 5033.
- [4] R. E. Came, J. M. Eiler, J. Veizer, K. Azmy, U. Brand, C. R. Weidman. Coupling of surface temperatures and atmospheric CO_2 concentrations during the Palaeozoic era. *Nature* **2007**, 449, 198.
- [5] H. P. Affek, M. Bar-Matthews, A. Ayalon, A. Matthews, J. M. Eiler. Glacial/interglacial temperature variations in Soreq cave speleothems as recorded by "clumped isotope" thermometry. *Geochim. Cosmochim. Acta* **2008**, 72, 5351.
- [6] B. H. Passey, N. E. Levin, T. E. Cerling, F. H. BROWN, J. M. Eiler, K. K. Turekian. High-temperature environments of human evolution in East Africa based on bond ordering in paleosol carbonates. *Proc. Natl. Acad. Sci. U. S. A.* **2010**, 107, 11245.
- [7] I. Halevy, W. W. Fischer, J. M. Eiler. Carbonates in the Martian meteorite Allan Hills 84001 formed at 18 ± 4 degrees $^{\circ}\text{C}$ in a near-surface aqueous environment. *Proc. Natl. Acad. Sci. U. S. A.* **2011**, 108, 16895.
- [8] A. K. Tripathi, S. Sahany, D. Pittman, R. a Eagle, J. D. Neelin, J. L. Mitchell, L. Beaufort. Modern and glacial tropical snowlines controlled by sea surface temperature and atmospheric mixing. *Nat. Geosci.* **2014**, 7, 205.
- [9] K. W. Huntington, A. R. Lechler. Carbonate clumped isotope thermometry in continental tectonics. *Tectonophysics* **2015**, 647, 1.
- [10] R. A. Eagle, T. Tütken, T. S. Martin, A. K. Tripathi, H. C. Fricke, M. Connely, R. L. Cifelli, J. M. Eiler. Ordering in Fossil Biominerals. *Science*. **2011**, 333, 443.
- [11] Z. Wang, E. a. Schauble, J. M. Eiler. Equilibrium thermodynamics of multiply substituted isotopologues of molecular gases. *Geochim. Cosmochim. Acta* **2004**, 68, 4779.
- [12] P. Ghosh, J. Adkins, H. Affek, B. Balta, W. Guo, E. A. Schauble, D. Schrag, J. M. Eiler. ^{13}C - ^{18}O bonds in carbonate minerals: A new kind of paleothermometer. *Geochim. Cosmochim. Acta* **2006**, 70, 1439.

- [13] E. A. Schauble, P. Ghosh, J. M. Eiler. Preferential formation of ^{13}C – ^{18}O bonds in carbonate minerals, estimated using first-principles lattice dynamics. *Geochim. Cosmochim. Acta* **2006**, *70*, 2510.
- [14] W. Guo, J. L. Mosenfelder, W. a. Goddard, J. M. Eiler. Isotopic fractionations associated with phosphoric acid digestion of carbonate minerals: Insights from first-principles theoretical modeling and clumped isotope measurements. *Geochim. Cosmochim. Acta* **2009**, *73*, 7203.
- [15] K. W. Huntington, J. M. Eiler, H. P. Affek, W. Guo, M. Bonifacie, L. Y. Yeung, N. Thiagarajan, B. Passey, A. Tripathi, M. Daëron, R. Came. Methods and limitations of “clumped” CO_2 isotope (Δ_{47}) analysis by gas-source isotope ratiomass spectrometry. *J. Mass Spectrom.* **2009**, *44*, 1318.
- [16] K. J. Dennis, H. P. Affek, B. H. Passey, D. P. Schrag, J. M. Eiler. Defining an absolute reference frame for “clumped” isotope studies of CO_2 . *Geochim. Cosmochim. Acta* **2011**, *75*, 7117.
- [17] B. He, G. A. Olack, A. S. Colman. Pressure baseline correction and high-precision CO_2 clumped-isotope (Δ_{47}) measurements in bellows and micro-volume modes. *Rapid Commun. Mass Spectrom.* **2012**, *26*, 2837.
- [18] X. Cao, Y. Liu. Theoretical estimation of the equilibrium distribution of clumped isotopes in nature. *Geochim. Cosmochim. Acta* **2012**, *77*, 292.
- [19] K. Prasanna, S. K. Bhattacharya, P. Ghosh, S. Mahata, M.-C. Liang. Isotopic homogenization and scrambling associated with oxygen isotopic exchange on hot platinum: studies on gas pairs (O_2 , CO_2) and (CO , CO_2). *RSC Adv.* **2016**, *6*, 51296.
- [20] M. Clog, D. Stolper, J. M. Eiler. Kinetics of $\text{CO}_2(\text{g})$ - $\text{H}_2\text{O}(1)$ isotopic exchange, including mass 47 isotopologues. *Chem. Geol.* **2015**, *395*, 1.
- [21] L. T. Zhuravlev. The surface chemistry of amorphous silica. Zhuravlev model. *Colloids Surfaces A Physicochem. Eng. Asp.* **2000**, *173*, 1.
- [22] H. P. Affek. Clumped isotopic equilibrium and the rate of isotope exchange between CO_2 and water. *Am. J. Sci.* **2013**, *313*, 309.
- [23] T. Kluge, C. M. John, A. L. Jourdan, S. Davis, J. Crawshaw. Laboratory calibration of the calcium carbonate clumped isotope thermometer in the 25-250 °C temperature range. *Geochim. Cosmochim. Acta* **2015**, *157*, 213.
- [24] S. V. Petersen, I. Z. Winkelstern, K. C. Lohmann, K. W. Meyer. The effects of Porapak(TM) trap temperature on $\delta^{18}\text{O}$, $\delta^{13}\text{C}$, and Δ_{47} values in preparing samples for clumped isotope analysis. *Rapid Commun. Mass Spectrom.* **2015**, *30*, 1.
- [25] D. A. Stolper, A. L. Sessions, A. A. Ferreira, E. V. Santos Neto, A.

Schimmelmann, S. S. Shusta, D. L. Valentine, J. M. Eiler. Combined ^{13}C -D and D-D clumping in methane: Methods and preliminary results. *Geochim. Cosmochim. Acta* **2014**, *126*, 169.

- [26] M. A. Webb, T. F. Miller. Position-specific and clumped stable isotope studies: Comparison of the urey and path-integral approaches for carbon dioxide, nitrous oxide, methane, and propane. *J. Phys. Chem. A* **2014**, *118*, 467.
- [27] P. S. Hill, A. K. Tripathi, E. A. Schauble. Theoretical constraints on the effects of pH, salinity, and temperature on clumped isotope signatures of dissolved inorganic carbon species and precipitating carbonate minerals. *Geochim. Cosmochim. Acta* **2014**, *125*, 610.
- [28] K. J. Dennis, D. P. Schrag. Clumped isotope thermometry of carbonatites as an indicator of diagenetic alteration. *Geochim. Cosmochim. Acta* **2010**, *74*, 4110.

4.8 Tables

Table 4.1: Isotopic composition of the gases used in this study

Gas	Grad	$\delta^{13}\text{C}_{\text{VPDB}} (\text{‰})$	$\delta^{18}\text{O}_{\text{VSMOW}}(\text{‰})$
MRSI-T2	Coleman	-13.05	28.00
MRSI-T4	Coleman	-30.04	-12.30
Cararra	In-house gas	2.44	40.53

Ph.D. Thesis – M. EL-Shenawy; McMaster University – School of Geography and Earth Sciences

Table 4.2: Experimental conditions, conventional and clumped isotope compositions during the time series experiments on MRSI-T4 gas

Experiment ID	N	Equilibration temperature (°C)	Equilibration time (h)	$\delta^{13}\text{C}_{\text{VPDB}}$ (‰)	$\delta^{18}\text{O}_{\text{VSMOW}}$ (‰)	δ^{47} (‰)	Raw Δ_{47} (‰)
MIE-d47kin-T4-initial	8	Room temp	1 year	-30.04 ± 0.01	12.30 ± 0.02	-37.99 ± 0.02	0.000 ± 0.007
MIE-d47kin-T4-1	5	100.0	1.000	-30.05 ± 0.00	12.27 ± 0.01	-38.16 ± 0.02	-0.133 ± 0.005
MIE-d47kin-T4-2	5	100.0	1.970	-30.04 ± 0.01	12.31 ± 0.01	-38.18 ± 0.04	-0.195 ± 0.010
MIE-d47kin-T4-3	5	100.0	3.000	-30.04 ± 0.00	12.30 ± 0.00	-38.24 ± 0.02	-0.259 ± 0.008
MIE-d47kin-T4-4	5	100.0	5.750	-30.04 ± 0.00	12.28 ± 0.01	-38.29 ± 0.02	-0.283 ± 0.005
MIE-d47kin-T4-5	5	100.0	7.000	-30.05 ± 0.00	12.29 ± 0.01	-38.30 ± 0.02	-0.297 ± 0.007
MIE-d47kin-T4-6	5	100.0	50.00	-30.04 ± 0.00	12.31 ± 0.01	-38.27 ± 0.02	-0.299 ± 0.007
MIE-d47kin-T4-7	5	100.0	96.00	-30.04 ± 0.00	12.31 ± 0.00	-38.27 ± 0.00	-0.301 ± 0.002
MIE-d47kin-T4-8	5	491.0	0.042	-30.04 ± 0.00	12.29 ± 0.01	-38.41 ± 0.02	-0.407 ± 0.008
MIE-d47kin-T4-9	5	491.0	0.083	-30.05 ± 0.01	12.26 ± 0.02	-38.65 ± 0.02	-0.636 ± 0.004
MIE-d47kin-T4-10	4	491.0	0.167	-30.04 ± 0.01	12.28 ± 0.01	-38.75 ± 0.02	-0.761 ± 0.003
MIE-d47kin-T4-11	3	491.0	0.250	-30.05 ± 0.00	12.28 ± 0.01	-38.79 ± 0.02	-0.806 ± 0.004
MIE-d47kin-T4-12	4	491.0	2.000	-30.07 ± 0.06	12.21 ± 0.14	-38.90 ± 0.20	-0.818 ± 0.004
MIE-d47kin-T4-13	5	491.0	14.00	-30.05 ± 0.00	12.29 ± 0.01	-38.80 ± 0.02	-0.820 ± 0.004
MIE-d47kin-T4-14	4	491.0	26.00	-30.05 ± 0.00	12.30 ± 0.01	-38.78 ± 0.01	-0.809 ± 0.007
MIE-d47kin-T4-15	5	1000	0.033	-29.91 ± 0.01	11.30 ± 0.01	-39.68 ± 0.03	-0.876 ± 0.010
MIE-d47kin-T4-16	5	1000	0.167	-29.86 ± 0.01	11.46 ± 0.02	-39.50 ± 0.02	-0.896 ± 0.004
MIE-d47kin-T4-17	5	1000	0.500	-29.91 ± 0.00	11.50 ± 0.03	-39.52 ± 0.03	-0.910 ± 0.006
MIE-d47kin-T4-18	4	1000	1.500	-29.92 ± 0.01	11.63 ± 0.02	-39.40 ± 0.02	-0.906 ± 0.005
MIE-d47kin-T4-19	5	1000	4.000	-29.91 ± 0.00	11.84 ± 0.02	-39.19 ± 0.05	-0.913 ± 0.004
MIE-d47kin-T4-20	5	50.00	26.00	-29.93 ± 0.01	11.28 ± 0.01	-38.94 ± 0.02	-0.064 ± 0.009
MIE-d47kin-T4-21	5	50.00	72.00	-29.93 ± 0.00	11.28 ± 0.01	-38.98 ± 0.02	-0.113 ± 0.004
MIE-d47kin-T4-22	5	50.00	144.0	-29.93 ± 0.00	11.29 ± 0.01	-39.01 ± 0.05	-0.147 ± 0.004
MIE-d47kin-T4-23	5	50.00	216.0	-29.92 ± 0.00	11.30 ± 0.01	-38.99 ± 0.02	-0.141 ± 0.005
MIE-d47kin-T4-24	4	50.00	288.0	-29.93 ± 0.00	11.28 ± 0.01	-39.02 ± 0.02	-0.151 ± 0.007

Table 4.3: Variations of Δ_{47} values with temperature at thermodynamic equilibrium in the three CO₂ gases tested in this study

Experimnt No.	Temperature (°C)	MRSI-T4 $\Delta_{47\text{-equ}}$ (‰)	MRSI-T2 $\Delta_{47\text{-equ}}$ (‰)	Carrara $\Delta_{47\text{-equ}}$ (‰)
1	50	-0.142	-0.122	-0.064
2	50	-0.127	-0.122	-0.078
3	50	-0.160	-0.125	-0.067
4	50	-0.134	-0.097	-0.077
5	50	-0.141	-0.128	-0.063
	Mean ± 1SE	-0.141 ± 0.005	-0.119 ± 0.006	-0.070 ± 0.003
1	100	-0.296	-0.276	-0.265
2	100	-0.309	-0.300	-0.269
3	100	-0.297	-0.282	-0.238
4	100	-0.279	-0.296	-0.241
5	100	-0.317		-0.255
	Mean ± 1SE	-0.299 ± 0.007	-0.288 ± 0.006	-0.254 ± 0.006
1	200	-0.542	-0.504	-0.476
2	200	-0.552	-0.490	-0.469
3	200	-0.547	-0.523	-0.491
4	200	-0.548	-0.515	-0.457
5	200	-0.529	-0.482	
	Mean ± 1SE	-0.544 ± 0.004	-0.503 ± 0.008	-0.473 ± 0.007
1	300	-0.660	-0.633	-0.612
2	300	-0.642	-0.640	-0.601
3	300	-0.661	-0.650	-0.609
4	300	-0.642	-0.630	-0.592
5	300	-0.649		-0.595
	Mean ± 1SE	-0.651 ± 0.004	-0.638 ± 0.004	-0.602 ± 0.004
1	491	-0.824	-0.796	-0.772
2	491	-0.804	-0.784	-0.764
3	491	-0.818	-0.808	-0.759
4	491	-0.827	-0.788	-0.766
5	491	-0.811	-0.785	-0.753
	Mean ± 1SE	-0.817 ± 0.005	-0.792 ± 0.004	-0.763 ± 0.003
1	600	-0.871	-0.840	-0.771
2	600	-0.849	-0.837	-0.803
3	600	-0.863	-0.850	-0.815
4	600	-0.864	-0.831	-0.808
5	600	-0.870	-0.833	-0.773
	Mean ± 1SE	-0.863 ± 0.004	-0.838 ± 0.003	-0.794 ± 0.009
1	800	-0.886	-0.874	-0.833
2	800	-0.904	-0.870	-0.832
3	800	-0.894	-0.891	-0.837
4	800	-0.895	-0.871	-0.843
5	800	-0.896	-0.882	-0.828
	Mean ± 1SE	-0.895 ± 0.003	-0.878 ± 0.004	-0.835 ± 0.003
1	1000	-0.914	-0.881	-0.869
2	1000	-0.917	-0.886	-0.858
3	1000	-0.907	-0.907	-0.863
4	1000	-0.925	-0.892	-0.854
5	1000	-0.904	-0.886	-0.854
	Mean ± 1SE	-0.913 ± 0.004	-0.890 ± 0.004	-0.860 ± 0.003
1	1100	-0.924	-0.904	-0.872
2	1100	-0.921	-0.897	-0.858
3	1100	-0.939	-0.890	-0.872
4	1100	-0.926	-0.912	-0.865
5	1100	-0.922		-0.852
	Mean ± 1SE	-0.926 ± 0.003	-0.901 ± 0.005	-0.864 ± 0.004

4.9 Figures

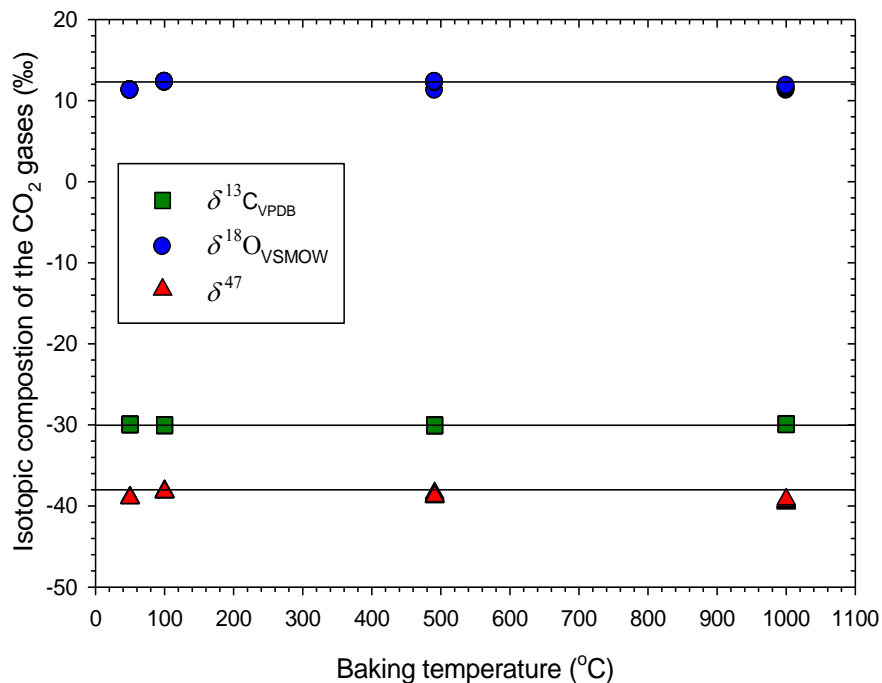


Fig. 4.1: $\delta^{13}\text{C}$, $\delta^{18}\text{O}$ and δ^{47} values of the baked CO₂ gases in the time series experiments. Horizontal lines indicate the mean of the starting CO₂ gas.

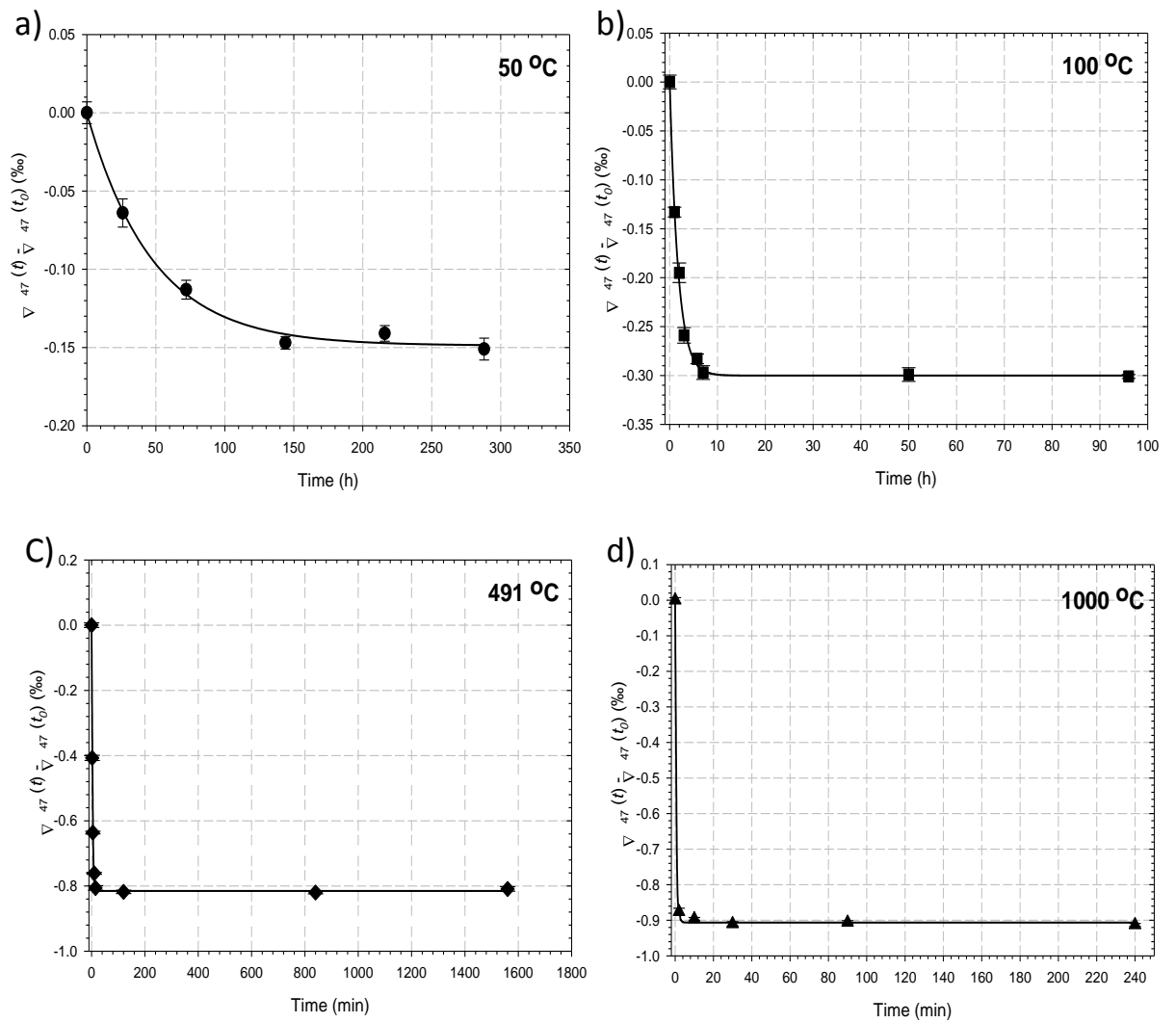


Fig. 4.2: Time evolution of Δ_{47} values in the baked CO_2 gas in the time series experiments at: (a) 50 °C (b) 100 °C, (c) 491 °C, and (d) 1000 °C.

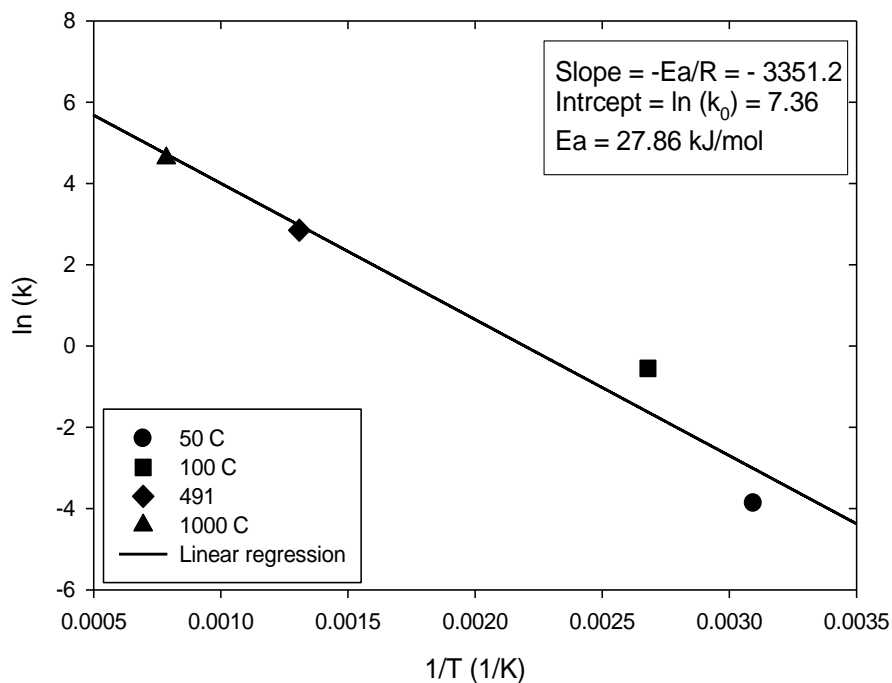


Fig. 4.3: Arrhenius regression of the rate constants estimated in this study for determining activation energy and pre-exponential factor. The slope of the line is equivalent to $-E_a/R$, and the intercept is equivalent to $\ln(K_0)$.

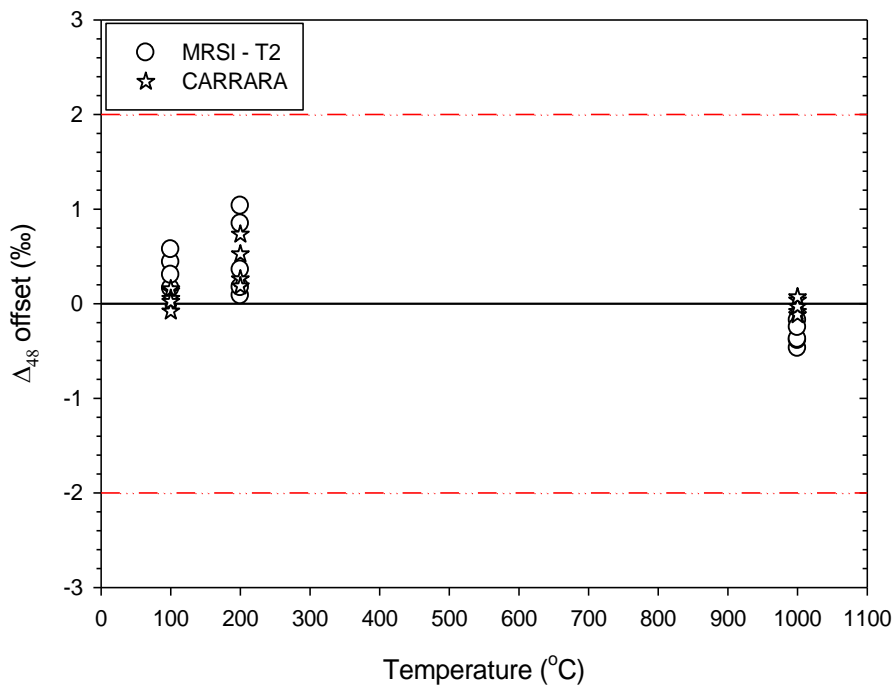


Fig. 4.4: Δ_{48} offset of CO_2 gases measured in the first protocol (CBM) from the mean Δ_{48} values of the same CO_2 gases that were measured in the second protocol (BCM) at same baking temperatures. Solid line defines the mean of Δ_{48} values in the BCM protocol whereas the dashed lines indicate the acceptable limit of the Δ_{48} values (i.e., contamination base line).

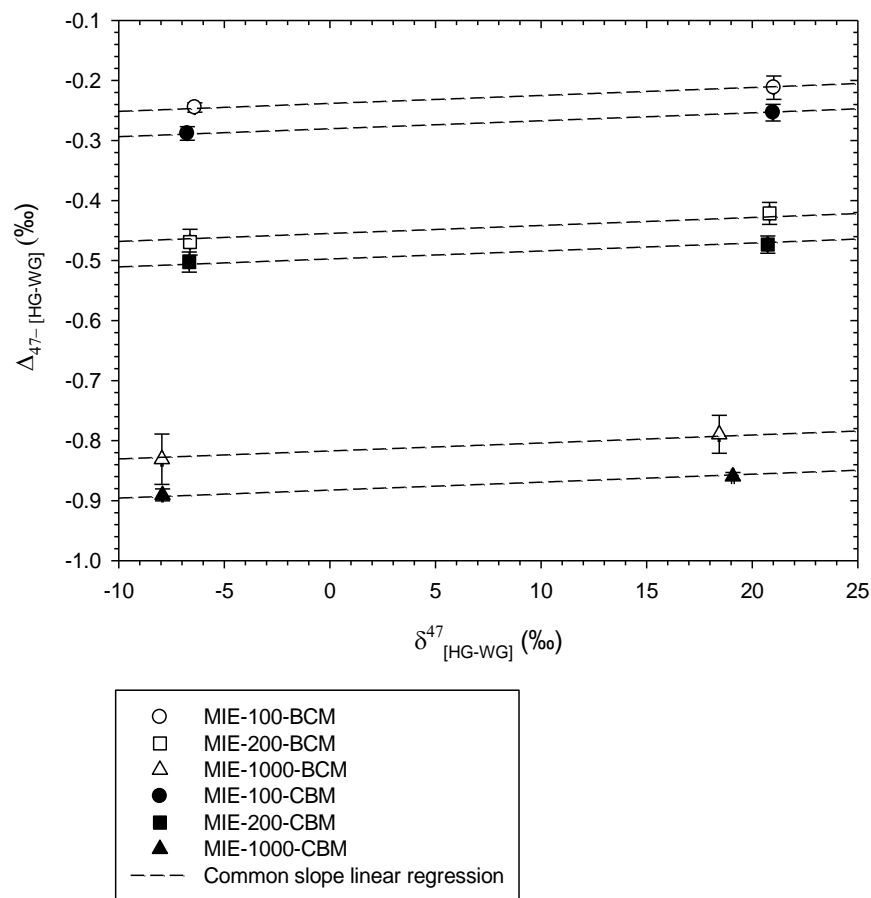


Fig. 4.5: A comparison between the measured Δ_{47} values in heated CO_2 gases from the two experimental protocols (i.e., CBM, BCM) in this study, showing the isotope reordering effect of the CO_2 cleaning procedures on the Δ_{47} values (i.e., decrease in Δ_{47} with increasing the temperature at which the CO_2 was baked).

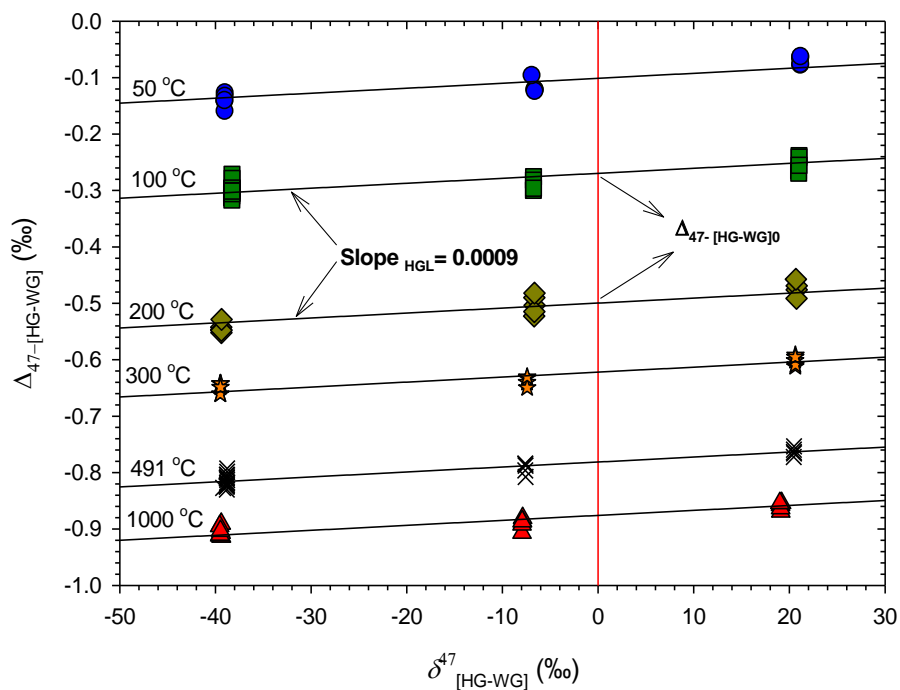
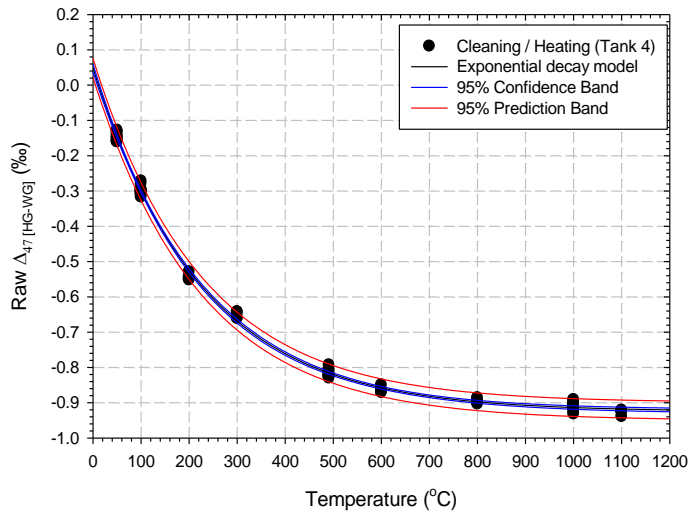
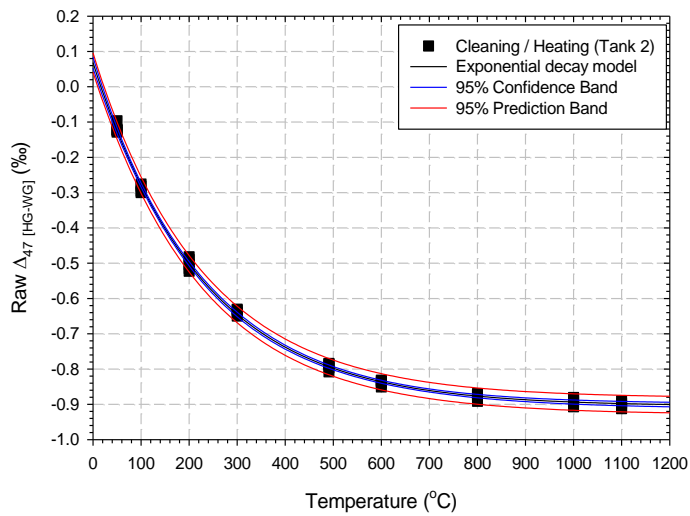


Fig. 4.6: A common slope regression lines of the heated gases at isotopic equilibrium from different temperatures using the CBM protocol. $\text{Slope}_{\text{HGL}}$ and $\Delta_{47-[HG-WG]0}$ define the nonlinearity slope and intercept, respectively.

a)



b)



C)

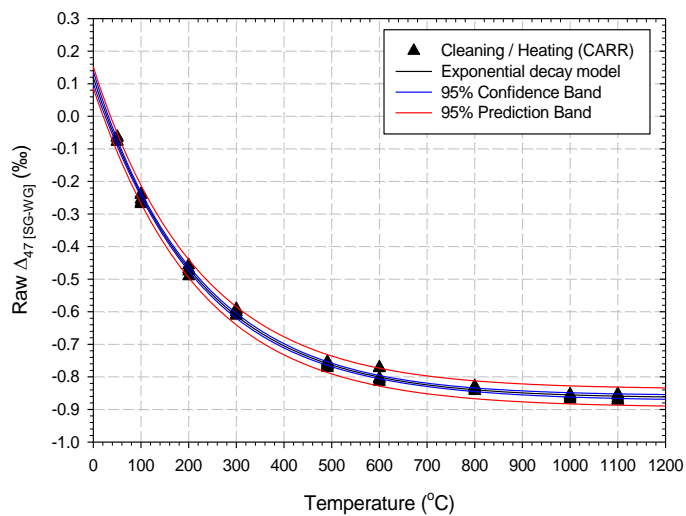


Fig. 4.7: Exponential fits of the PBL-corrected Δ_{47} (raw) measurements of three CO_2 gases at thermodynamic equilibrium between 50 and 1100 °C. a) MRSI-T4, b) MRSI-T2 and c) Carrara.

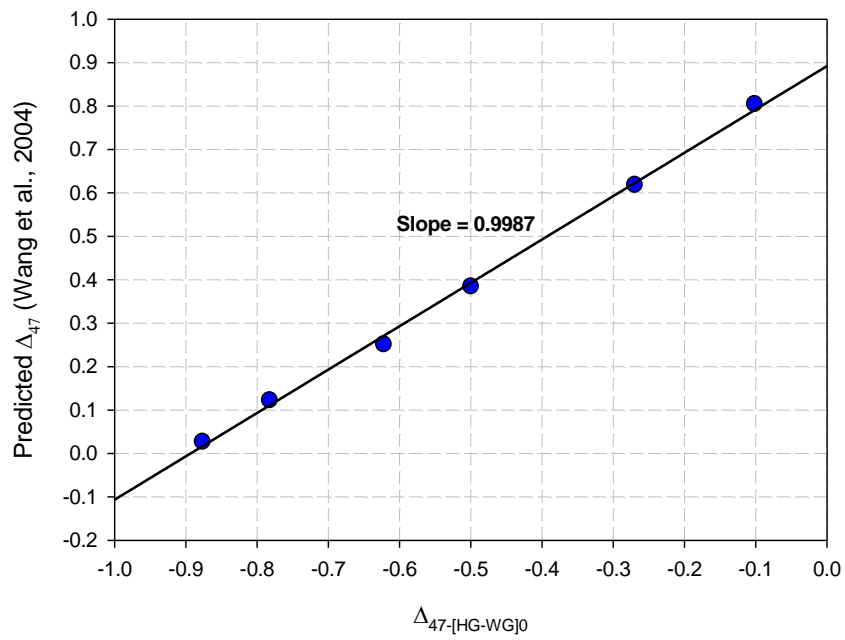


Fig. 4.8: Least-squares fit of the intercepts of the heated CO₂ gas lines ($\Delta_{47-[HG-WG]_0}$) against their corresponding values from the theoretical model from Wang *et al.*,^[11].

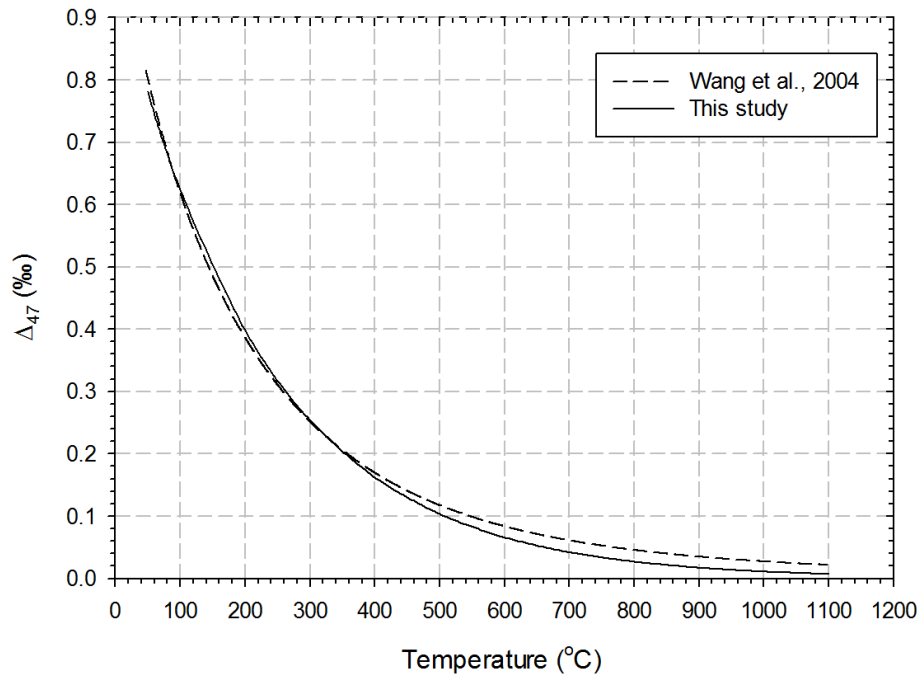


Fig. 4.9: A comparison between the experimental Δ_{47} – T calibration in this study and the theoretical calculations of Wang *et al.*,^[11]

Chapter 5 - Conclusions and outlook

5.1 Conclusions

This thesis contributes to the knowledge required to interpret stable isotope compositions ($\delta^{13}\text{C}$ and $\delta^{18}\text{O}$) of natural speleothems as paleoclimate proxies (Chapter 2). In Chapter 2, an experimental approach was used to mimic the formation of speleothems in natural caves. The outcomes of this experimental study enable us to predict carbon and oxygen isotope equilibrium fractionation factors between calcite and drip water in cave environments. The measured equilibrium carbon isotope fractionation factor is 1.7 ± 0.7 ‰ and is shown to be insensitive to the cave temperature. In contrast, the equilibrium oxygen isotope fractionation factor is temperature-dependant and is expressed as (T in Kelvin; $R^2 = 0.97$; $P < 0.0001$):

$$1000\ln^{18}\alpha_{\text{Cc-H}_2\text{O}} = 18.33 (10^3/T) - 33.14$$

These equilibrium isotope fractionation factors were measured from slow calcite precipitates in pool-like settings, defining a datum to refer to when modern cave calcites are evaluated for the occurrence and magnitude of non-equilibrium isotope effects. Moreover, non-equilibrium carbon and oxygen isotope fractionation factors between calcite and drip water were measured in stalagmite-like settings. These non-equilibrium isotope fractionation factors deviate positively from the equilibrium isotope fractionation factors determined from pool carbonates. The magnitude of this deviation increases with decreasing the flow rate of drip water above the apex of stalagmites. The flow rate controls non-equilibrium carbon and oxygen isotope fractionations based upon the following two mechanisms:

- 1) The decrease in drip water flow rate allows time for progressive consumption of the DIC reservoir by the rapid CO₂ degassing out of the thin water film formed on the surface of stalagmite. This rapid CO₂ degassing preferably uses the lighter carbon and oxygen isotopes in the DIC reservoir, enriching the remaining DIC reservoir in both ¹³C and ¹⁸O. Subsequent transfer of these isotopic enrichments to precipitating CaCO₃ is facilitated by the rapid CaCO₃ precipitation (100s of seconds) on the surface of stalagmite.
- 2) The drip water flow rate also controls the non-equilibrium carbon isotope effects in stalagmites through carbon isotope exchange between DIC species and the cave CO₂. Slow flow rates lead to increasing the non-equilibrium carbon isotope effects in stalagmites and vice versa. However, the magnitude of the carbon isotope exchange effect on calcite in stalagmites depends on how far the DIC in drip water is from isotopic equilibrium with cave CO₂. For instance, the carbon isotope exchange effect would be negligible when cave CO₂ is mainly generated by CO₂ degassing from drip water (i.e., closed caves), whereas this effect would increase in strong ventilated caves with CO₂ of higher carbon isotope composition than those of DIC in drip water.

Based on our laboratory studies, a maximum non-equilibrium oxygen isotope effect in stalagmites was predicted to be 2.95 ± 0.14 ‰, which is close to the equilibrium oxygen isotope fractionation between bicarbonate ion and calcite (this study and Beck et al., 2005). This non-equilibrium isotope effect-induced by the flow rate explains the current discrepancy among the published equilibrium $1000\ln^{18}\alpha_{\text{Cc-H}_2\text{O}}$ values (e.g., Coplen, 2007;

Tremaine et al., 2011) and the variability in reported $1000\ln^{18}\alpha_{\text{Cc-H}_2\text{O}}$ from modern farmed calcite samples from a natural cave setting. Moreover, this prediction might open a new window to quantify the non-equilibrium oxygen isotope effects in stalagmites and thus to precisely estimate the paleotemperature (see section 6.2). Furthermore, the results of these experiments can be used to refine the existing theoretical models for simulating carbon and oxygen isotope systematics in cave environments.

Chapter 3 contributes to the knowledge gained from the utilization of natural speleothems as a paleoclimate archive. This chapter presents a new line of evidence regarding the timing and source of the moisture responsible for the greening of the Sahara over the past 350 ka, which permitted the periodic passage of hominins to Eurasia, through this otherwise hyper-arid terrain. This evidence is based on uranium-series dating and oxygen isotope compositions of a double stalagmite (WS-5d) collected from Wadi Sannur cave (central Egypt) in the northeastern Sahara desert. The U/Th dates of the WS-5d stalagmite growth suggest that greening conditions extended widely in the Sahara for brief time intervals during the interglacial Marine Isotope Stages MIS 5.5, MIS 7.3, and the early MIS 9. In addition, the WS-5d stalagmite possesses distinct low $\delta^{18}\text{O}$ values, suggesting a distal moisture source. We attribute this source to long-traveling rains from the Atlantic Ocean that were delivered via the West African monsoon system (WAM). High CO_2 concentration and summer insolation facilitated the north extension of the WAM up to Wadi Sannur cave (28 °N) during the periods of stalagmite growth. The two youngest greening periods were concurrent with the arrival of *Homo sapiens* in the

Levant (130 – 100 ka) and an earlier possible change in human population at ~244 ka in this region, indicating a key role of the Sahara route in early human dispersal out of Africa. This new speleothem-based evidence can also be used to validate the climate models in the North Africa region.

Finally, Chapter 4 provides the first experimental determined Δ_{47} – T relationship in a CO₂ gas phase (Δ_{47} in ‰, T in °C; $R^2 = 0.99$, $P < 0.0001$):

$$\Delta_{47\text{equ}} = 0.9791 (\pm 0.0029) \exp (-0.0045 * T)$$

This relationship can be used as an alternative to that which is predicted by the existing theoretical models to normalize the Δ_{47} measurements. Our experimental approach (i.e., heating CO₂ in a dried quartz tube) discussed in Chapter 4 enables us to prepare thermodynamic equilibrium CO₂ gases between 50 and 1100 °C. Therefore, our proposed approach will benefit the community for the normalization of Δ_{47} measurements in two ways:

- 1) The preparation of CO₂ standards for Δ_{47} normalization requires a single experimental protocol. In the current Δ_{47} normalization method, two different experimental protocols are necessary to prepare CO₂ standards (i.e., CO₂-H₂O equilibration at low temperatures and heated CO₂ at 1000 °C). This conventional practice may cause a systematic error during the Δ_{47} normalization.
- 2) Unlike the current Δ_{47} normalization method, heated CO₂ gases enable the direct correction of the carbonate-derived CO₂ gases against CO₂ standards of similar Δ_{47} values (i.e., similar Δ_{47} correction matrix).

The expected improvement in our newly proposed Δ_{47} normalization method will help the community to accurately calibrate the carbonate clumped isotope thermometry and to understand the Δ_{47} systematics in speleothems.

5.2 Outlook

Future research opportunities arisen from this thesis work are listed below:

- 1) In Chapter 2, we proposed a non-linear model (Eq. 2.4) to project non-equilibrium oxygen isotope effects in ancient stalagmites back to isotopic equilibrium and to construct the paleotemperature. Equation 2.4 can be rearranged to the following form:

$$1000\ln^{18}\alpha_{\text{Cc-H}_2\text{O}}(eq) = 1000\ln^{18}\alpha_{\text{Cc-H}_2\text{O}}(neq) - 2.95 \left[\frac{\text{Consumed DIC}}{\text{DIC initial} - \text{DIC equilibrium}} \right]$$

The $1000\ln^{18}\alpha_{\text{Cc-H}_2\text{O}}(neq)$ can be estimated by measuring the $\delta^{18}\text{O}$ values of fluid inclusions and calcites in a stalagmite. The consumed DIC from the seepage water before (PCP) and at the time of calcite precipitation on the apex of the stalagmite can be calculated from fractionation of calcium isotopes ($\delta^{44}\text{Ca}$) in stalagmite relative to value for the bed rock. The (DIC initial - DIC equilibrium) term in the equation should be equal to the maximum non-equilibrium calcium isotope effect in stalagmites, which can be predicted using the same approach used for the oxygen isotope data in our study. The proposal of using calcium isotopes as a proxy for the DIC term in our model relies on that $\delta^{44}\text{Ca}$ in drip water reflect that of the host rock with negligible isotopic fractionation during the dissolution

process (Reynard et al., 2011). Moreover, calcium isotope fractionation between carbonate and water has a weak temperature dependency (Reynard et al., 2011).

- 2) The speleothem-based evidence for the greening of the Sahara in Chapter 3 raises the following question: What was the temperature when the North African monsoon extended far north up to Wadi Sannur cave? Estimating this temperature is critical to understand the positive feedback of the global warming over the North Africa region where water resources are limited. Speleothem records are a good candidate to answer this question based on our experimental observations presented in Chapter 2. Furthermore, conducting fluid inclusion study on the WS-5d stalagmite is needed to confirm the moisture source over the North Africa during the interglacial periods. High resolution oxygen isotope records from multiple speleothem samples from the Wadi Sannur cave and the other adjacent cave (Dajara cave) would be helpful to support the conclusions from Chapter 3, as well as to understand the variability of the WAM during the interglacial periods.
- 3) Chapter 4 shows that CO₂ cleaning procedures are the main source of the scrambling effect observed in measured Δ_{47} values. Therefore, the clumped isotope community should validate our findings by repeating our experiments. In addition, clumped isotope compositions of the carbonates synthesized for Chapter 2 might help the community to resolve the current discrepancy among the existing carbonate clumped isotope calibrations (by measuring the Δ_{47} in pool carbonates) and to understand the Δ_{47} systematics in speleothems (by measuring the Δ_{47} in stalagmite carbonates).

5.3 References

- Coplen T. B. (2007) Calibration of the calcite-water oxygen-isotope geothermometer at Devils Hole, Nevada, a natural laboratory. *Geochim. Cosmochim. Acta* **71**, 3948–3957.
- Reynard L. M., Day C. C. and Henderson G. M. (2011) Large fractionation of calcium isotopes during cave-analogue calcium carbonate growth. *Geochim. Cosmochim. Acta* **75**, 3726–3740.
- Tremaine D. M., Froelich P. N. and Wang Y. (2011) Speleothem calcite farmed in situ: Modern calibration of $\delta^{18}\text{O}$ and $\delta^{13}\text{C}$ paleoclimate proxies in a continuously-monitored natural cave system. *Geochim. Cosmochim. Acta* **75**, 4929–4950.